

NPS ARCHIVE
1965
HASKELL, H.

INVESTIGATION OF A LOW ENERGY
ALKALI ION GUN

HUGH B. HASKELL

LIBRARY
U.S. NAVAL POSTGRADUATE SCHOOL
MONTEREY, CALIFORNIA

DUDLEY KNOX LIBRARY
NAVAL POSTGRADUATE SCHOOL
MONTEREY CA 93943-5101

**INVESTIGATION OF A
LOW ENERGY ALKALI
ION GUN**

*** * * * ***

Hugh B. Haskell

INVESTIGATION OF A LOW
ENERGY ALKALI ION GUN

by

Hugh B. Haskell

//
Lieutenant, United States Navy

Submitted in partial fulfillment of
the requirement for the degree of

MASTER OF SCIENCE
IN
PHYSICS

United States Naval Postgraduate School
Monterey, California

1 9 6 5

MRS Archive

H2783

1965

Haskell, H.

~~Library~~
U. S. Naval Postgraduate School
Monterey, California

INVESTIGATION OF A LOW
ENERGY ALKALI ION GUN

by

Hugh B. Haskell

This work is accepted as fulfilling
the thesis requirements for the degree of

MASTER OF SCIENCE

IN

PHYSICS

from the

United States Naval Postgraduate School

ABSTRACT

A design used by Simpson and Kuyatt for a multistage electron gun has been modified for use with ions. In the work reported here a thermal emitter of Lithium ions using the mineral β -eucryptite was employed as a source of ions. While the electron gun yielded a space charge limited beam, practical and theoretical considerations held the obtainable Lithium ion currents to less than 10% of the space charge limit in most cases. Currents of 10^{-10} to 10^{-7} amps were obtained at nominal energies of 2 to 100 eV. Minimum beam radii occurred a few cm. from the end of the lens and were less than one mm. at higher energies and less than two mm. at all energies. Well collimated beams of up to 16 cm. in length have been obtained. Beam profiles were measured and analyzed assuming the radial current density to be Gaussian. Theoretical calculations of space charge dispersion are presented along with the information necessary for design and use of the gun. Detailed measurements of the energy distribution of the ions are in progress but no conclusive results are available at this time.

TABLE OF CONTENTS

Section	Title	Page
1.	Introduction	1
2.	Experimental Arrangement	7
	(a) Vacuum System	7
	(b) Emitter	7
	(c) Electrodes	10
	(d) Detector	15
	(e) Energy and Mass Analyzers	18
3.	Results and Discussion	19
	(a) Total Current	19
	(b) Beam Profiles	22
	(c) Extraction Stage Perveance	40
	(d) Mass Analysis	41
	(e) Energy Spread of the Ion Beam	41
4.	Conclusion	43
5.	Acknowledgements	45
6.	Bibliography	46
Appendices		
1.	Mass Independence of the Trajectory of a Charged Particle in an Axially Symmetric Electrostatic Field	48
2.	Calculation of Beam Spreading Due to Space Charge	51
3.	Voltage Divider Circuit for Electrode Potentials	61
4.	Estimation of Emitter Current Densities	63
5.	Analysis of Beam Profile Data	67
6.	Design Curves	79

LIST OF ILLUSTRATIONS

Figure		Page
1.	Schematic Diagram of Ion Gun	3
2.	Vacuum Chamber Assembly	8
3.	Emitter Assembly	9
4.	Emitter Temperature as a Function of Filament Power	11
5.	Detail of Extraction Stage	13
6.	Detail of Electrode Plate Mounting	14
7.	Ion Gun Assembly	16
8.	Beam Collector Assembly	17
9.	Diode Emission Characteristic of Li^+ Emitter	21
10.	Effect of Interstage Space Charge Spreading	23
11. through 30.	Beam Profiles	24
31.	Mass Analysis	42
2-1	Optical Ray Pattern of Focused Beam	52
2-2	Effect of Space Charge on Beam Rays	59
3-1	Voltage Divider Network	62
4-1	Ray Patterns Defining the Angle α	64
5-1	Split Geometry for Beam Profile Analysis	68
5-2 through 5-7	Measured Beam Profiles for 10 and 80v Beams and Check of Gaussian Current Density Assumption	72
6-1	Maximum Li^+ Beam Current Based on Equation (1)	82
6-2	Langmuir Child Law for Various Diode Spacings	82
6-3	Required Emitter Li^+ Current Density <u>vs.</u> Beam Voltage for Various Image Sizes	83

6-4	Optical Characteristics of the Deceleration Stage	83
6-5	Characteristics of the Extraction Stage	84
6-6 through 6-18	Image Size and Focal Distance <u>vs.</u> Beam Perveance Under the Influence of Space Charge for the Parameters L and $\tan \gamma$	85

SYMBOLS

α	-	Parameter of assumed density distribution
B	-	Subscript referring to lens opening
γ	-	Beam convergence angle, launching angle
D	-	Dawson function
d_k	-	Emitter to grid distance in lens extraction stage
e	-	Electronic charge
E	-	Energy, electric field, efficiency
ΔE	-	Energy spread
η	-	Charge to mass ratio
i	-	current
Δi	-	Element of current passing through a slit
j	-	Current density
L	-	Distance from lens opening to optical focal point
L_F	-	Distance from lens opening to space charge focal point
M	-	Magnification
m	-	Mass
m_e	-	Electronic mass
O	-	Object distance
P	-	Perveance, $i/V^{3/2}$
P_e	-	Extraction stage perveance, $i/V_a^{3/2}$
Q	-	Image distance
R	-	Radius
r	-	radius
r_F	-	Radius of space charge focal point
r_l	-	Radius of outer ray defining the beam

r_2	-	Radius of inner ray defining the beam
r_0	-	Minimum value of r_1
s	-	Space charge spreading parameter
T	-	Temperature
V	-	Potential
V_a	-	Accelerating electrode potential measured with respect to emitter
V_g	-	Grid potential measured with respect to emitter
V_o	-	Emitter potential (beam potential) above ground
y	-	Distance of collector slit from beam axis
Δy	-	Slit width
z	-	Axial distance along beam
ϕ	-	Error function , radial angle of cylindracal co-ordinates

1. Introduction

In recent years the study of atomic collision processes has been directed increasingly towards measurement of differential cross sections at low energies. Thus there has developed a need for systems capable of producing well defined monoenergetic beams of ions in the energy range less than 100 eV. In this energy region the effects of space charge and energy resolution become increasingly important, and are often the limiting factors in a given experiment.

Space charge effects limit the amount of current that can be passed through a given cross sectional area according to the formula

$$i_{\max} = 4.67 \pi \epsilon_0 \sqrt{e/2m} V^{3/2} \tan^2 \chi \quad (1)$$

where V is the beam energy in eV, m is the particle mass, e is the electronic charge, and χ is the launching angle of the beam. (See Appendix 4). For Lithium ions the constant factor becomes 3.42×10^{-7} amp/(volt) $^{3/2}$. Pierce (1939, 1954) and Simpson and Kuyatt (1963d) have shown that space charge effects within the lens system and the nature of the emitter may reduce the obtainable current as much as several orders of magnitude below the limit predicted by equation (1) at low energies.

The energy spread of the beam, ΔE , is ultimately limited by the thermal distribution of the particles as they leave the emitter. Solid emitters tend to have lower energy spreads than plasma sources, and low energy systems may approach thermal energy spreads if the lens is designed to accept only those particles that leave the emitter in, or very nearly in, the axial direction.

Pierce (1940) designed a widely used lens utilizing curved electrodes designed to create the fields required to simulate flow between concentric spheres. Such a system for use with Lithium ions, utilizing a plane emitter fabricated from the mineral β -eucryptite ($\text{Li}_2\text{O} \cdot \text{Al}_2\text{O}_3 \cdot 2\text{SiO}_2$) was investigated by Lambert (1963b). This lens system has been used with some success by Eager (1964) and Lorents, et. al. (1965) for a rectangular slit geometry. However, the lack of flexibility as well as certain mechanical problems made it desirable to undertake an improved design.

Simpson and Kuyatt (1963c) have given a design for an electron gun with plane electrodes and cylindrical geometry, which utilizes a two stage (acceleration-deceleration) principle to minimize the losses within the lens arising from space charge limitations. A schematic diagram of the lens is given in Fig. 1.

The first stage extracts the particles at high energies and forms a well defined beam which is then decelerated to the desired final energy in the second stage. The first, or extraction, stage is based on designs given by Soa (1959) and the deceleration stage is based on the properties of plane electrodes as given by Spangenberg and Field (1943). The electrode potentials V_g and V_a are measured with respect to the emitter, which is maintained at the desired beam potential, while the exit electrodes are grounded, permitting the beam to be injected into a field free region at ground potential.

This design has several advantages over the Pierce gun, among which are simplicity of construction and versatility. Moving the deceleration stage with respect to the extraction stage and suitably varying the potentials on the electrodes permits beams of a wide range

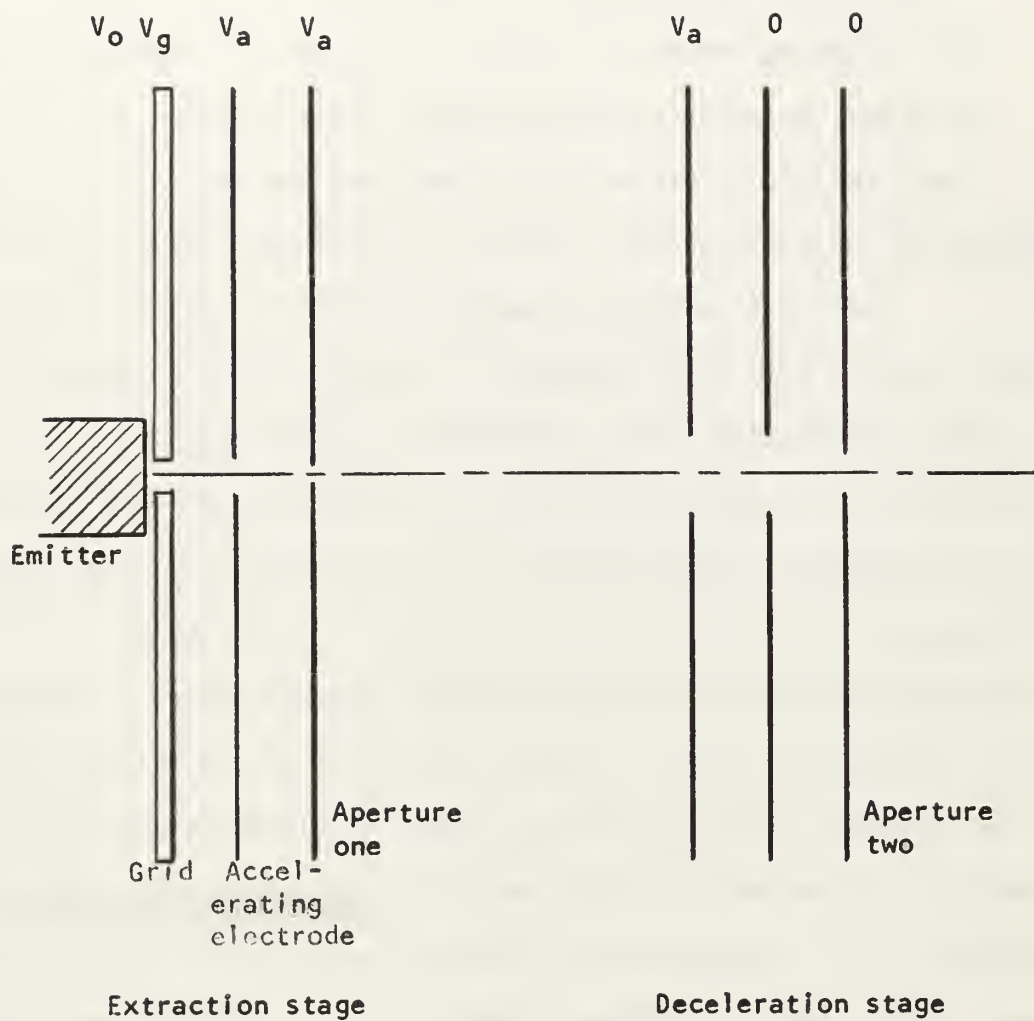


Fig. 1

Schematic Diagram of Ion Gun

of intensities and shapes to be formed.

It is shown in Appendix 1, that the trajectories of charged particles moving in axially symmetric electrostatic fields with small initial velocities are independent of the particle mass. Hence the focal properties of a lens designed for electrons, should, upon appropriate change of the polarity of the electrode potentials, be identical for any particle. Based upon this assumption, the above design for electrons has been adapted to the use of Lithium ions, utilizing a source consisting of a porous tungsten surface, impregnated with β -eucryptite to a depth of a few hundredths of an inch.

In Appendix 4 are discussed the theoretical limits on beam intensities from thermal effects at the emitter and internal space charge phenomena, based on the analysis of Pierce (1939, 1954). Two factors tended to make the beam intensities less than would be predicted by the results of Appendix 4. First, the analysis of Appendix 4 presumes that the emitter is space charge limited whereas the emitter utilized was emission limited at the extraction potentials used; and second, since Lithium has approximately 10^4 times the electron mass we expect that space charge effects in the field-free region of the lens will be much more significant for Lithium ions than for electrons. This is indeed the case, and in fact these two effects overlap, i.e the internal space charge effects are not negligible until extraction energies are sufficiently high that the emitter becomes emission limited. Hence we expect the total currents to be less than those predicted in Appendix 4. Further we may note that the higher mobility of electrons makes their entrapment in a Lithium ion beam and the resulting space charge neutralization unlikely.

Appendix 2 contains an analysis of space charge spreading of a beam in field free space, due to Wendt (1948) and Glaser (1952). Calculations based on these results indicate that for a given energy there is an upper limit to the current, beyond which a usable beam is not obtainable since the beam diverges immediately on leaving the lens. However, such currents are generally beyond the capabilities of this system, and this limit presents no problem.

A mass analysis of the emitter output was performed and showed the beam to be $\sim 98\%$ Li^7 , with Na^{23} and K^{39} impurities on the order of 1% at operating temperatures of $\sim 1100^\circ\text{C}$. The β -eucryptite utilized was prepared from Lithium enriched in Li^7 and the amount of Li^6 observed was $< .01\%$. Below 1100°C the percentage of beam impurities tended to be of the order of 10%, primarily Na and K but with a small quantity of Rb^{85} . The impurities tended to be driven off after a short while and the beam became almost pure Li^7 .

As expected the beam intensities tended to be lower than the maximum predicted by equation (1) by factors of 10 to 100, running from 10^{-10} amp, at very low energies to 10^{-7} amp, at higher energies. Although these currents are rather small, they are adequate for many atomic scattering experiments. Higher intensities may be achieved by operating at grid voltages $\sim 50\%$ of the extraction voltages. However, under such conditions, the focal properties of the lens are largely lost. This will be discussed in greater detail in section three.

The beam profiles were measured and analyzed by assuming that the radial current density of the beam is Gaussian in any cross section. The nominal beam radius is taken as that containing $(\frac{1}{e})$ of the total current. The validity of the Gaussian assumption is investigated in

Appendix 5. Note that the space charge spreading analysis of Appendix 2 is based in part on the assumption of uniform charge density in a cross-section. Clearly these two assumptions are not consistent with one another; nevertheless the predictions of the theory are in reasonable agreement with the measurements.

The energy resolution of the beam is still under investigation. On theoretical grounds it is reasonable to expect that any energy spread which may be observed will be due primarily to the nature of the emitter rather than the lens system. However, a definite answer must await the outcome of these measurements.

2. Experimental Arrangement

(a) Vacuum System

The lens and its associated equipment have been constructed in a large commercially built vacuum system which has been fully described by Lambert (1963b). Typical operating pressures were $\sim 10^{-6}$ Torr. Fig. 2 is a plan view of the aluminum vacuum chamber, a round can 18 inches in inside diameter and 10 inches deep. The lens was constructed so that the emitter could be rigidly mounted to the vacuum chamber on a flange shown at the bottom of Fig. 2, through which passed the electrical connections for the filament power and beam potential. The lens is constructed in two independently adjustable stages, each of which is mounted on a slider installed in a six inch "Unislide" assembly. The extraction stage elements were mounted on one slider whose position remained fixed with respect to the emitter. The deceleration stage elements were mounted on the other slider which was adjustable from outside the vacuum system by means of a screw arrangement through a Wilson seal in the same flange on which the emitter was mounted. Position was measured by a revolution counter mounted on the screw shaft. The entire lens apparatus was mounted on a section of I-beam which could be fixed to the bottom of the vacuum chamber.

(b) Emitter

The emitter (See Fig.3) consists of a sintered tungsten surface of 70% to 80% matrix density, into which is melted β -eucryptite to a depth of $\sim .010$ inches (The preparation and use of β -eucryptite has been fully described by Johnson, 1962 and Lagerstrom, 1963a). This surface

*Tropel, Inc., 52 West Avenue, Fairport, New York

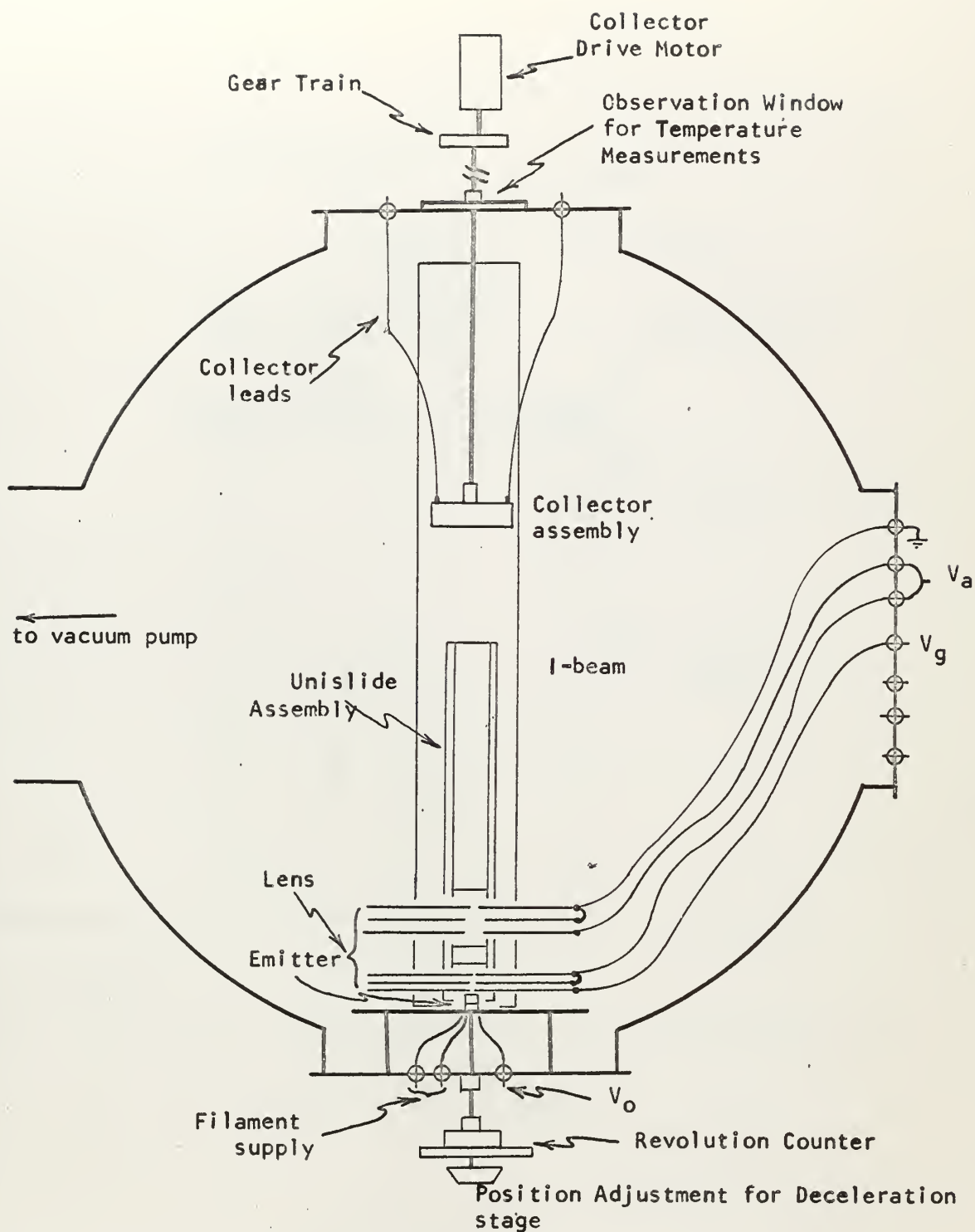


Fig. 2

Vacuum Chamber Assembly

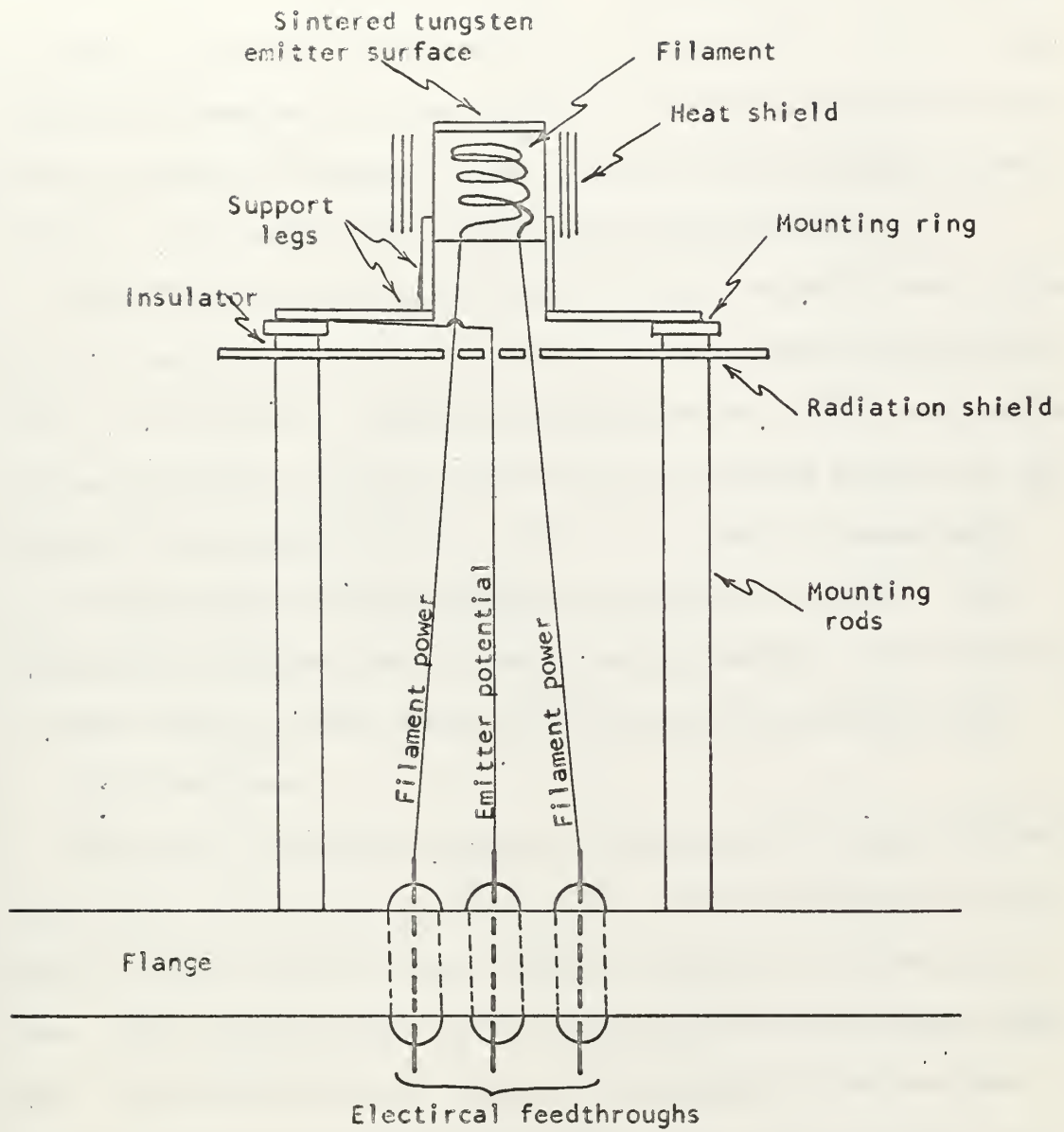


Fig. 3
Emitter Assembly

is welded to a .600 inch diameter tungsten cylinder which provides the housing for a filament of non-inductively wound tungsten wire, insulated from the emitter by alundum. The emitter is then surrounded by several layers of molybdenum foil as a heat shield. Finally, this apparatus is mounted to a ring by means of ruthenium and nickel legs. The ring forms the structural means of mounting the emitter, as seen in Fig. 2. The emitters were manufactured commercially.*

The filament power source found to be most successful was a direct current regulated power supply (such as Sorenson Nobatron DCR 150-15, which is very stable). Operating temperatures of $\sim 1700^{\circ}\text{C}$ were obtained with approximately 65 watts power input on a shielded emitter and 120-140 watts on an unshielded one. Fig. 4 is a graph of temperatures vs. filament power for both shielded and unshielded emitters, the temperature being measured with an optical pyrometer. For use with an a-c power supply a power factor of $\sim .8$ was found to be applicable.

(c) Electrodes

The gun is intended for use as an ion source for atomic scattering experiments in which the openings of the scattering chamber can be as much as .5cm. Hence the size of the final aperture was taken to be .5cm. This aperture serves to fix the maximum beam convergence angle, α . For convenience in carrying out the design calculations (see Appendix 6) the deceleration stage apertures were taken to be 1 cm. and they were placed 1 cm. apart. The final aperture was set 1 cm. downstream from the second decelerating electrode, a distance where its effect on the field formed between the deceleration plates is negligible.

*Spectra-Mat, Inc., P.O. Box 287, Freedom, California

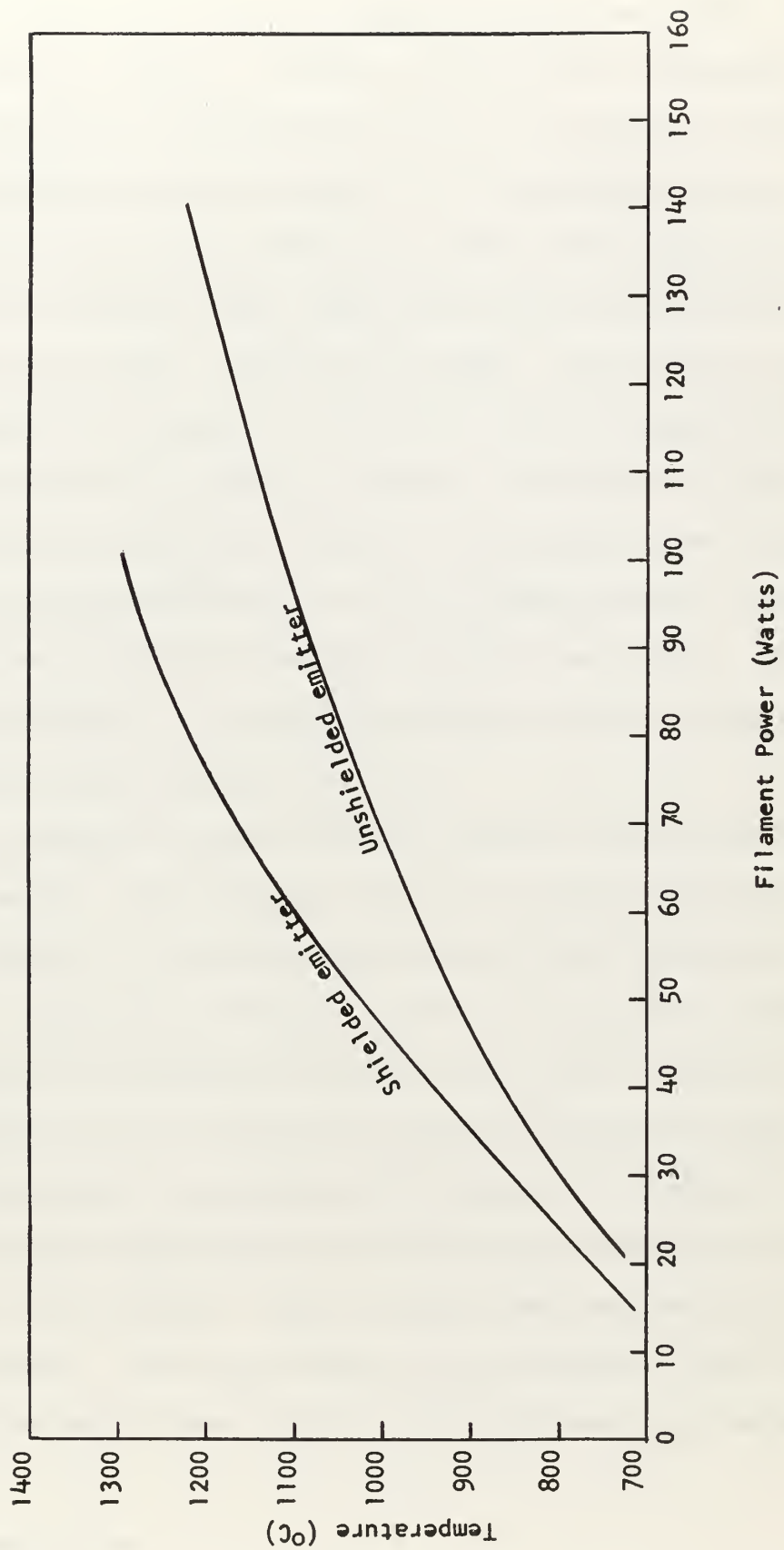


Fig. 4

Emitter Temperature as a Function of Filament Power

The extraction stage (see Fig. 5) is a standard Soa immersion lens, and is taken directly from the design of Simpson and Kuyatt (1963a) with all dimensions doubled. The design curves given by Simpson and Kuyatt are reproduced in Appendix 6 (fig. 6-5). The extraction stage forms an image which becomes the object for the deceleration stage, and the relative positioning of these two stages is then fixed by the location of the extraction stage image and the desired object distance of the deceleration stage. Following Soa (1959), the extraction stage object is assumed to be a spot on the emitter surface of approximately half the area of the grid aperture. Aperture 1 following the accelerating electrode was arbitrarily located 1 cm. downstream and following a suggestion of Simpson* was made so that its opening subtends an angle three times the desired convergence angle at the plane of the accelerating electrode. A reasonable convergence angle was taken as $\sim .07$ radians, giving an aperture of .2cm.

The lens elements were constructed of stainless steel discs four inches in diameter. The varying hole size in the plates made optical alignment difficult, so the plates were made with their holes exactly in the center and mounted on holders (see Fig. 6) for proper alignment. The brackets were insulated from the sliders with .003 inch layers of mica. To insure that the brackets were properly aligned and spaced, spacers of the proper size were made, drill rod was run through the alignment holes and clamped tight before the screws holding the brackets to the slider were tightened. When the spacers were removed, the plates could be installed. The entire assembly was then mounted in the vacuum chamber with the emitter face parallel to the grid plate, and approxi-

*Private Communication

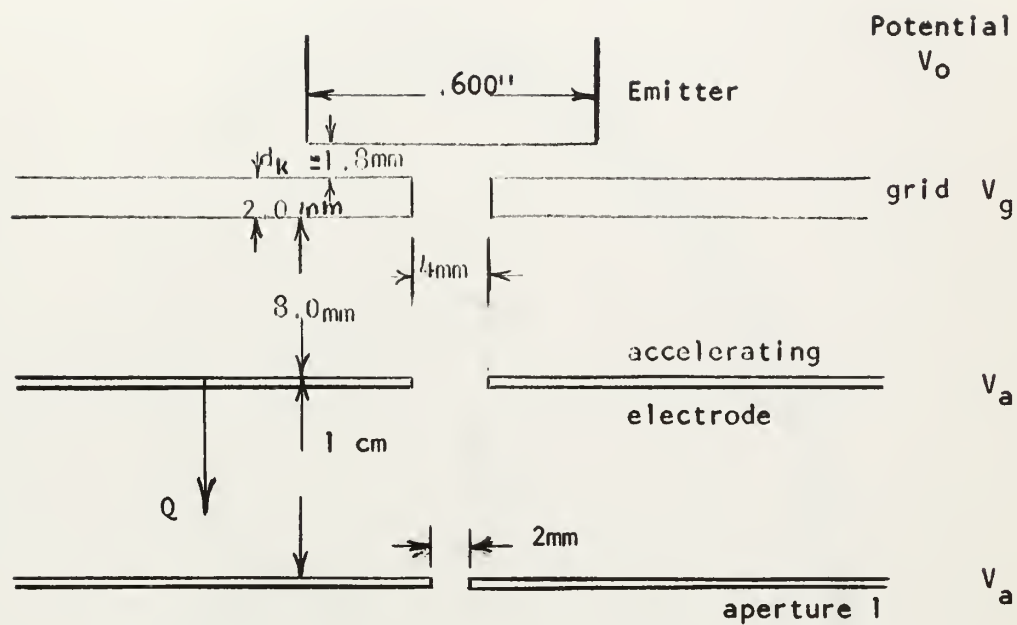


Fig. 5

Detail of Extraction Stage

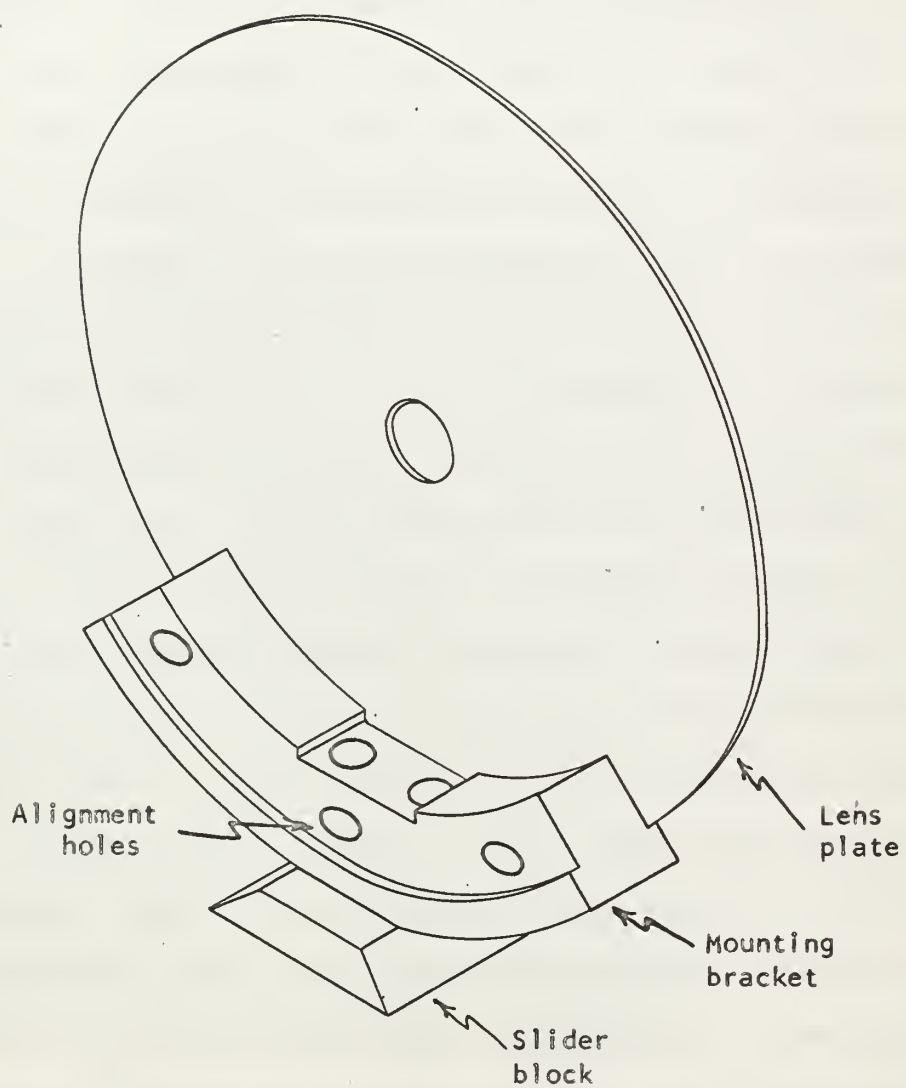


Fig. 6

Detail of Electrode Plate Mounting

mately centered on it. This arrangement is illustrated in Fig. 7. The appropriate potentials are then applied to the plates using the voltage divider network described in Appendix 3.

(d) Detector

The collector for the beam cross-section measurements consisted of a plate with a .23mm slit mounted vertically in front of an insulated collector plate, both encased in a foil container to reduce background (Fig. 8). Total current was then the sum of the currents to both plates (all current measurements being made with Keithley 410 micromicroam-meters). For the beam cross-section measurements the slit arrangement was mounted at the end of an eight cm. arm connected to a shaft passing through a Wilson seal (Top of Fig. 2) to the outside of the chamber. This shaft was rotated at ~ 2 rph by a variable speed d.c. motor through a reduction gear train. By this means the slit was swept across the beam and the current through the slit was recorded on a chart recorder. The trace thus recorded a sequence of very nearly parallel segments cut out of the beam. When this data is analyzed by the method of Appendix 5 it yields a value of beam "radius". The slit is then moved along the beam axis, and the process repeated. In this manner the beam profile may be measured. The motor speed was maintained constant by driving it with a regulated d-c power supply (Harrison Lab 6226A); friction chatter of the shaft at this slow speed seemed to be negligible. The sweep speed was measured by timing the motion of a collimated light beam reflected from a mirror attached to the rotating shaft. Results of these measurements are shown in Figs. 11 through 30, and discussed in detail in the next section.

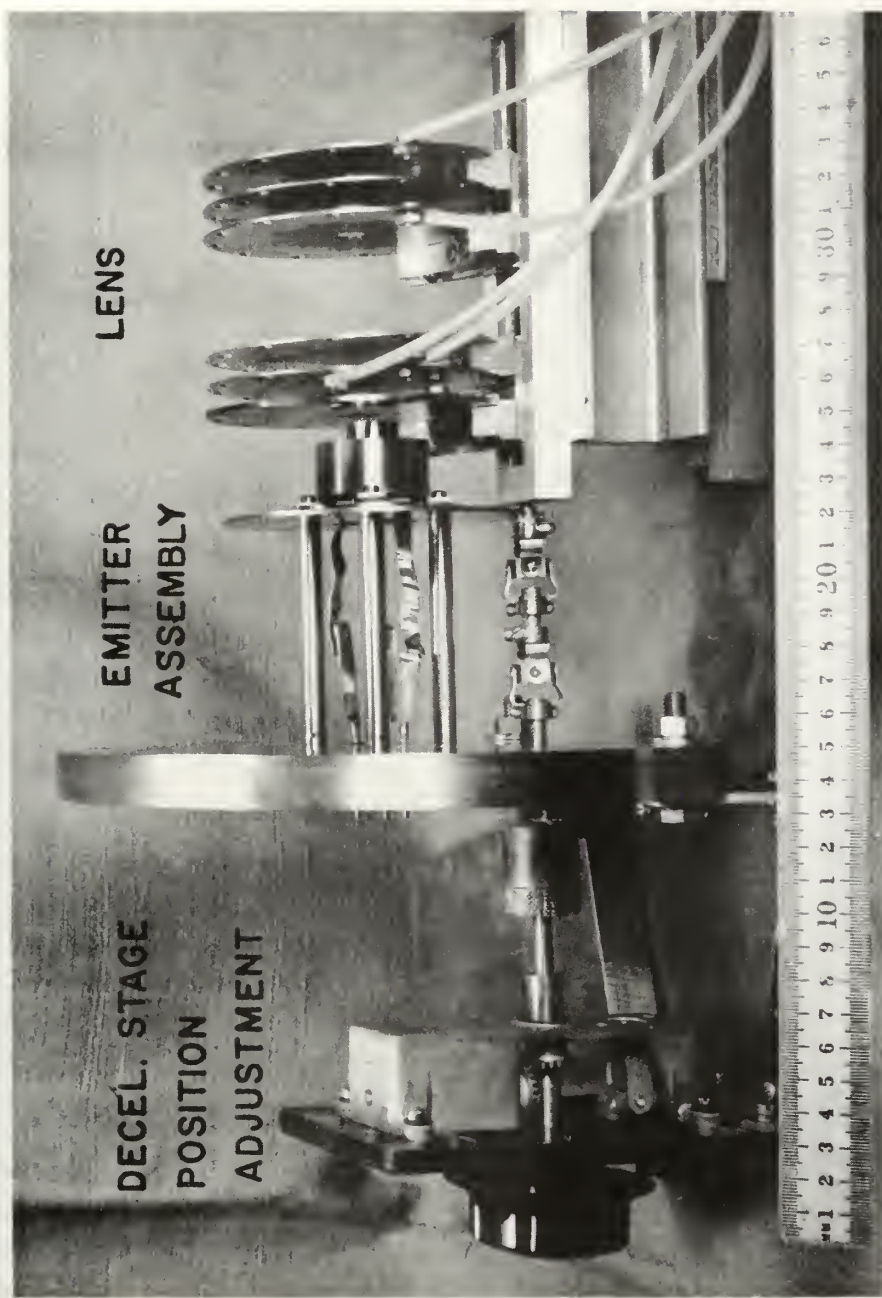


FIG. 7

Ion Gun Assembly

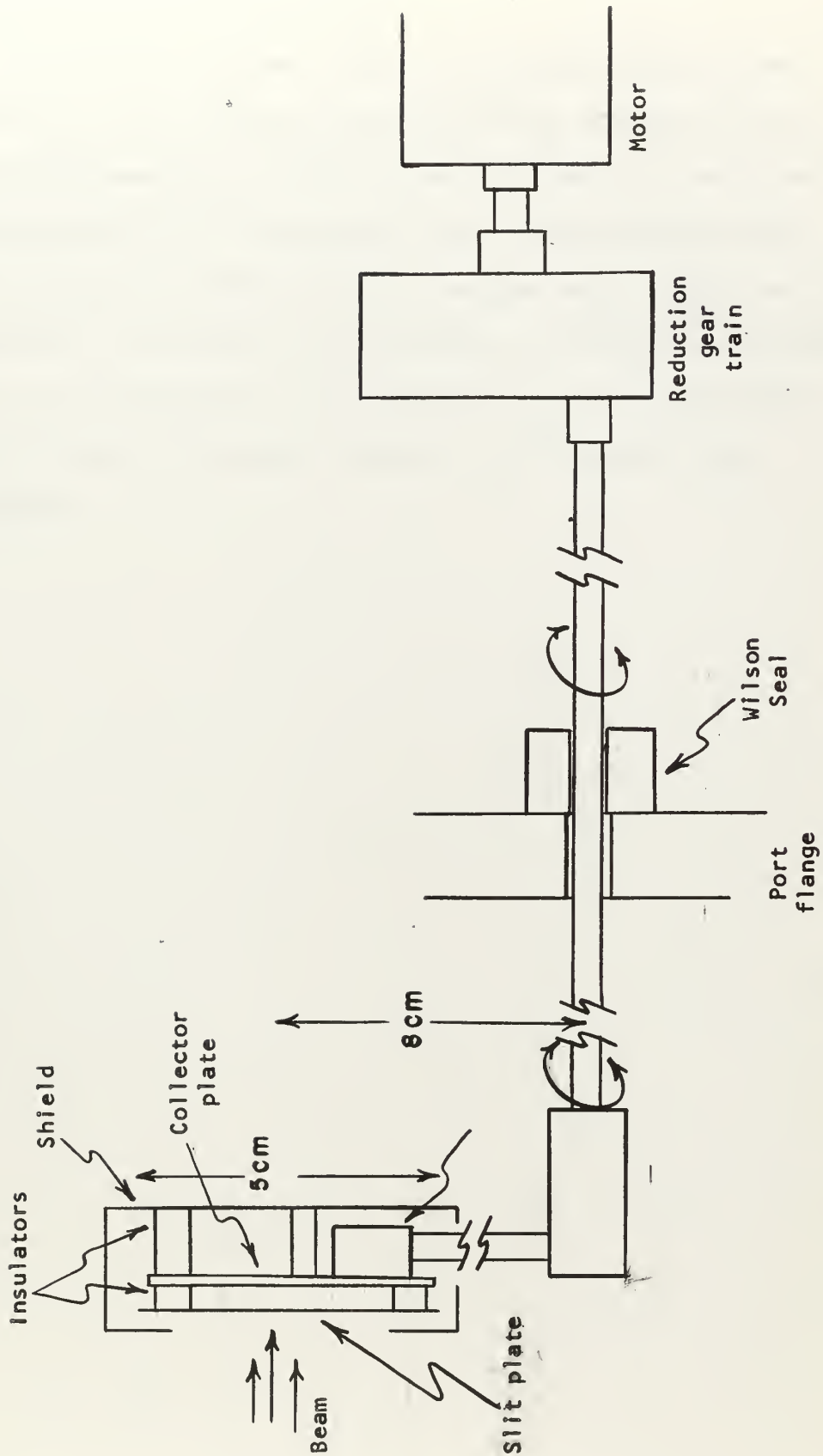


Fig. 8

Beam Collector Assembly

(e) Energy and Mass Analyzers

The analysis of the beam energy is being carried out by two methods: (1) a double screen retarding potential analyzer which is placed in the beam near the focal point thus assuring a fairly parallel ion beam, and (2) a 127° electrostatic deflecting analyzer with a narrow entrance slit, which permits investigation of spatial and energy correlations in the beam. The mass analysis of the beam was performed by Drs. J.R. Peterson and W. Aberth of Stanford Research Institute using an identical ion emitter mounted in a 90° magnetic mass spectrometer.

3. Results and Discussion

a. Total Current

The maximum possible current for any given value of beam convergence angle is given by equation (1), and is obtainable only under the specific condition that the beam is focused to a point defined by the initial beam radius and $\tan \alpha$ (See Fig. 4-1). The value of i_{\max} from equation (1) is given with each of the beam profiles shown below. We note that in each case the measured current is less than i_{\max} by factors varying from 10 to 100. This is attributed to several factors. First the lens is not focusing the beam toward a point but toward a spot of finite size and hence the conditions required by equation (1) are not met. For purposes of calculation with a finite image size, α was taken as the half angle of the cone formed by the inner rays which define the image, as shown in Fig. 4-1. This value of α constitutes a maximum and the effective value of convergence angle for equation (1) is somewhat smaller. A second factor undoubtedly is that the mechanical properties of the lens are not perfect. Finite plate thickness, slight aperture misalignment, plates not quite parallel or improperly spaced, as well as buildup of charge on the plates would cause the focusing properties to deviate from the ideal, with resultant loss in current intensity. Third, and most importantly, is the effect of limited emission from the emitter and space charge spreading between stages. These effects will be discussed in somewhat more detail.

The emission current density from a plane parallel diode is given by the Langmuir-Child law

$$j_0 = \frac{4}{9} \epsilon_0 \sqrt{\frac{2e}{m}} \frac{V^{3/2}}{X^2} \quad (\text{amp/cm}^2) \quad (2)$$

where V is the voltage, x the diode spacing in cm., j_0 the current density in amp/cm², e the electronic charge, and m the particle mass. For a lithium emitter the constant factor becomes 2.075×10^{-8} . Fig. 9 is a plot of the diode emission characteristics of the emitter used. Electrode spacing was 2 cm. and the temperature of the emitter was $\sim 1200^\circ\text{C}$. The current density deviates from equation (2) quite markedly at voltages greater than 100 and is emission limited at voltages greater than 200. Since the extraction voltages are typically greater than 100 v except at very low beam energies this limit places a severe restriction on the obtainable current.

The data in Fig. 9 should be considered only as an upper limit on the emitter ion current since there exists the possibility that photoelectrons from the Lithium deposited on the collector may have contributed to the measured current despite the use of suppression grids. The results of Lagerstrom (1963a) and others indicate, however that considerably larger total currents can be obtained and work on improved emitters is in progress.

Space charge effects tend to be proportional to $m^{-\frac{1}{2}}$ where m is the particle mass, so effects calculated for electrons will be magnified by $(m_e/m)^{\frac{1}{2}}$ for heavier particles. For Lithium this ratio is ~ 100 . Hence the lens system designed by Simpson and Kuyatt for electrons and which operated in the voltage range where space charge spreading was negligible between stages will, when used with Lithium at similar voltages, have space charge losses between stages which are considerable. The space charge losses will be significant even at voltages where the emitter is emission limited. Hence the two effects overlap, and at no lens configuration is it possible to obtain the value of current given by equation (1).

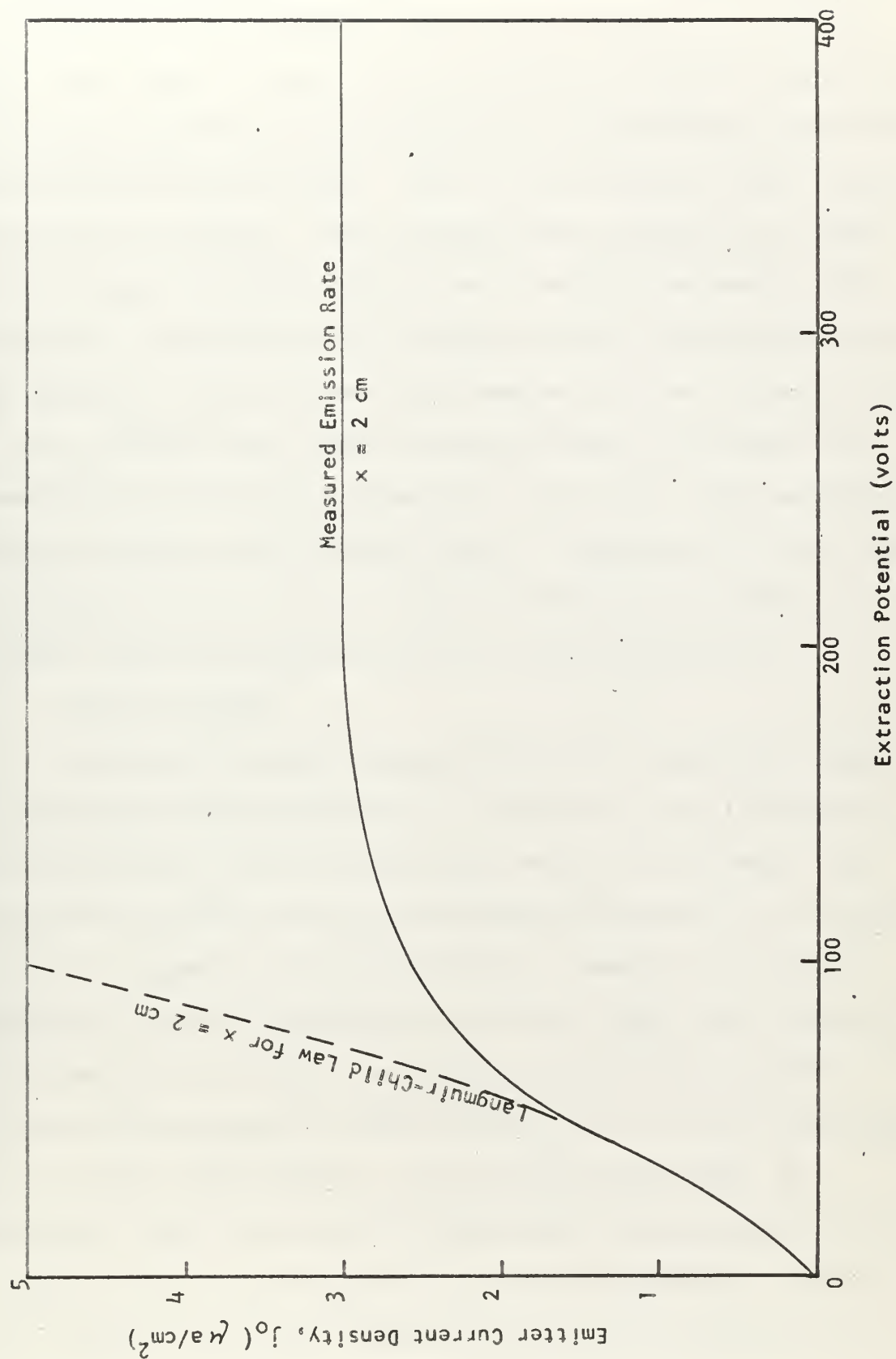


Fig. 9

Diode Emission Characteristic of Li^+ Emitter

An additional effect of space charge spreading between stages is to change the effective object location for the deceleration stage. The inter-stage beam, under the effect of space charge will reach the first plate of the deceleration stage more divergent than it would had space charge not been present. Fig. 10 illustrates the effect this has on the object position. Note that the effective object for the deceleration stage is both moved closer to the deceleration aperture and magnified. Inspection of the deceleration stage focal property curves in Appendix 6 (Fig. 6-4) shows that reducing the object distances for a given stepdown ratio extends the image distance and increases the magnification of the stage. Hence we see that space charge spreading between stages has the additional effect of increasing the final image distance as well as its size. This may make γ smaller which still further reduces the maximum current according to equation (1).

(b) Beam Profiles

A selection of measured beam profiles over a wide range of beam voltages and lens characteristics is presented in Figs. 11 through 30. On each plot are listed the significant values for each beam. Also shown are the optical image and the expected image based on the calculations of Appendix 2. The optical image is found by the methods of Appendix 6, based on the parameters grid bias, V_g/V_a , beam voltage, V_o , deceleration ratio, V_a/V_o , and deceleration stage object distance. Choosing these parameters rather arbitrarily fixes the final image size, r_a , the final image distance, L , and the convergence angle, γ . Ordinarily these values would be established by the experimental conditions and they would then serve to fix the lens parameters. However, the reverse procedure was followed in this case for evaluation of the

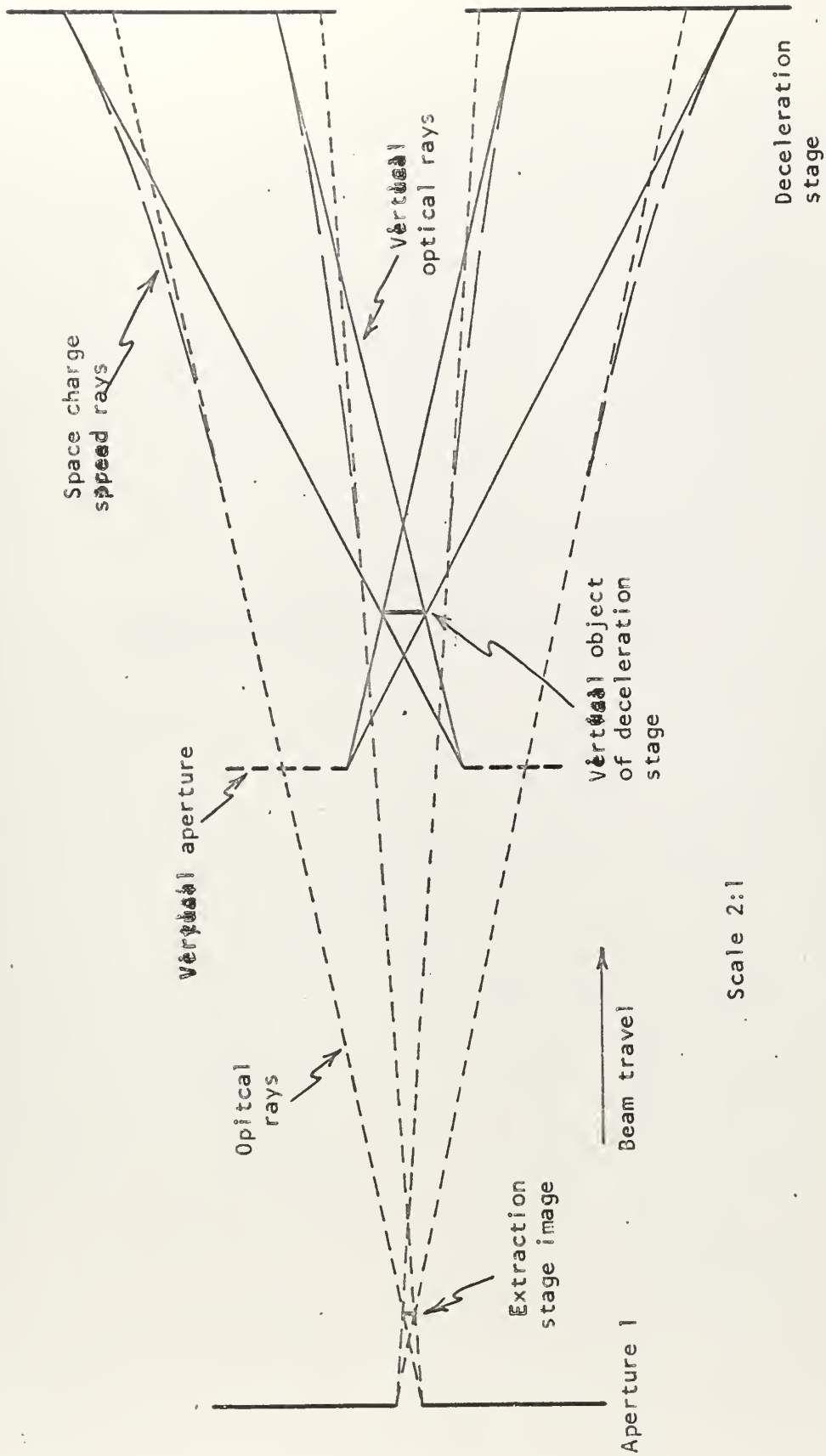


Fig. 10
Effect of Interstage Space Charge Spreading

Fig. 11 through 30
Beam Profiles for Indicated Conditions

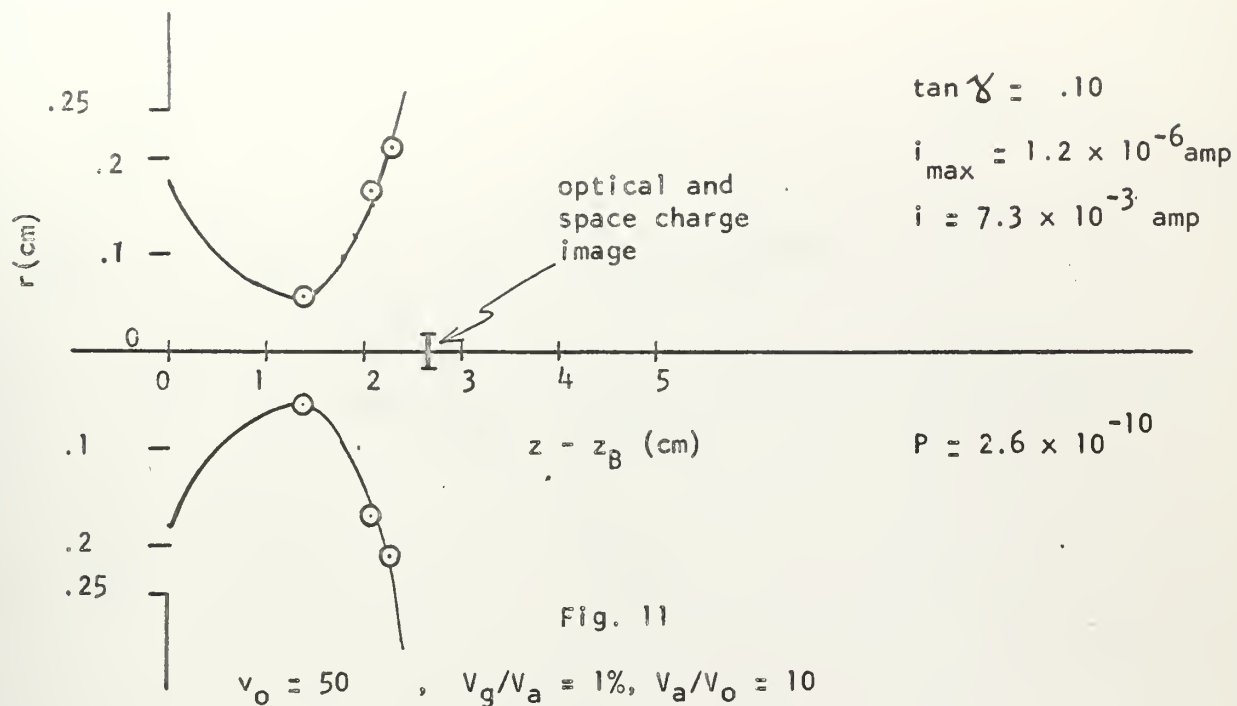


Fig. 11

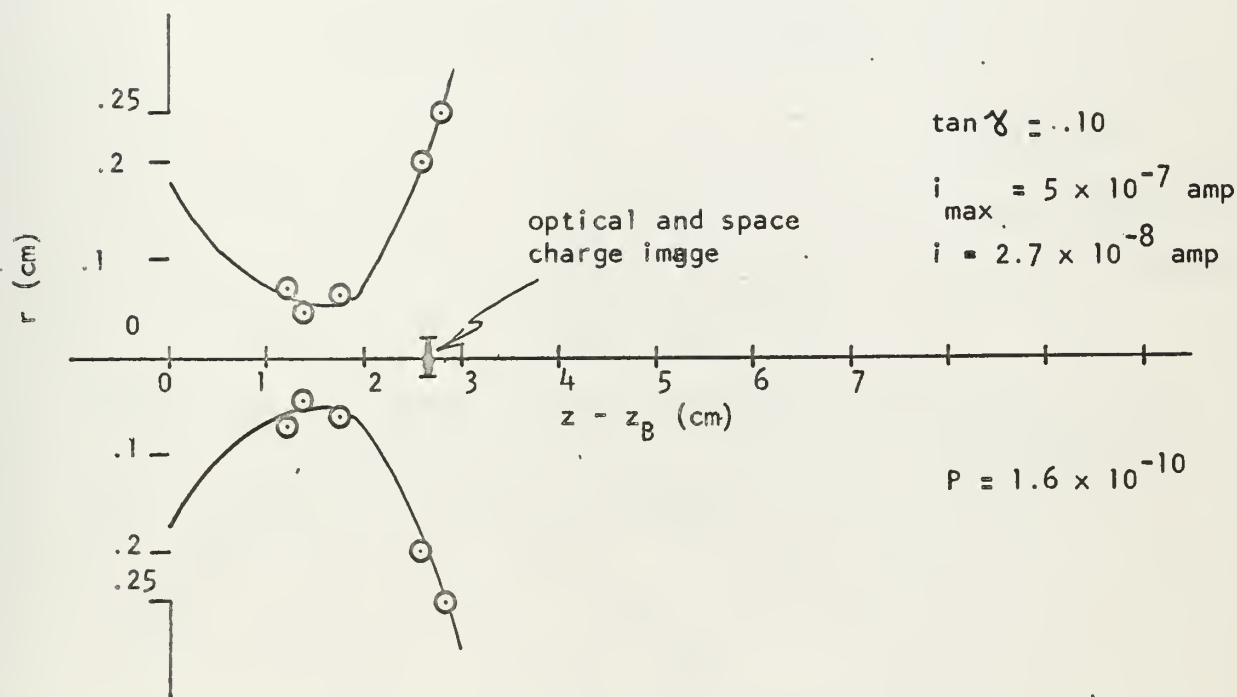


Fig. 12

$v_o = 30$, $V_g/V_a = 1\%$, $V_a/V_o = 10$

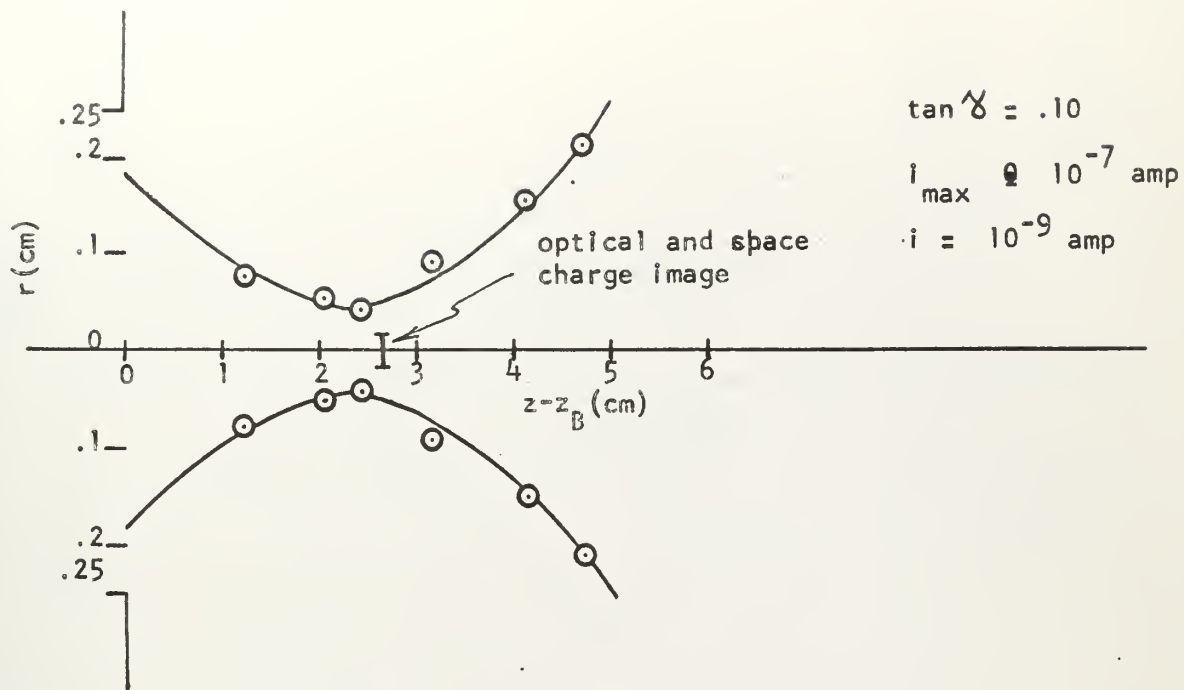


FIG. 13

$$V_0 = 10 \text{ eV}, V_g/V_a = .67\%, V_a/V_0 = 10$$

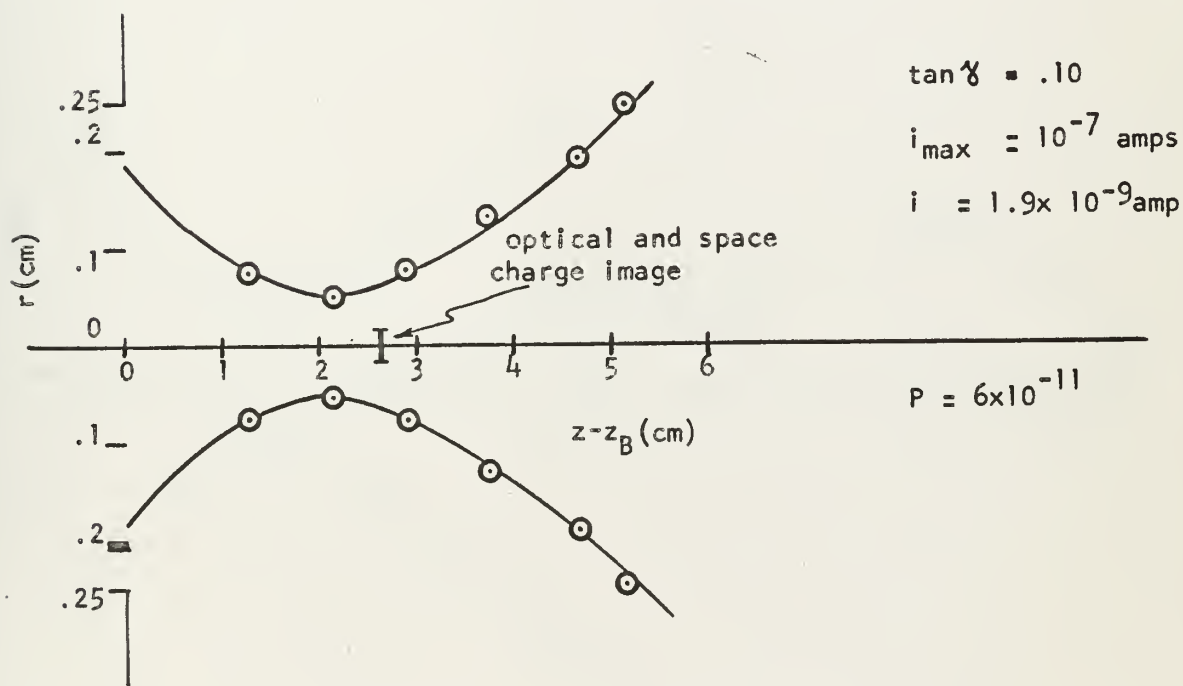


Fig. 14

$$V_0 = 10 \text{ eV}, V_g/V_a = 1\%, V_a/V_0 = 10$$

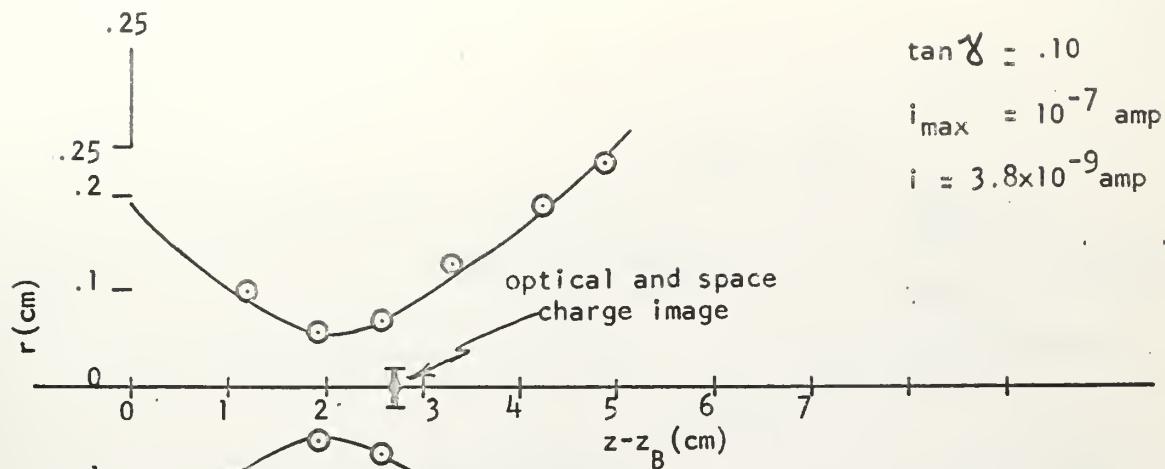


Fig. 15

$$V_0 = 10, \quad V_g/V_a = 1.5\%, \quad V_a/V_0 = 10$$

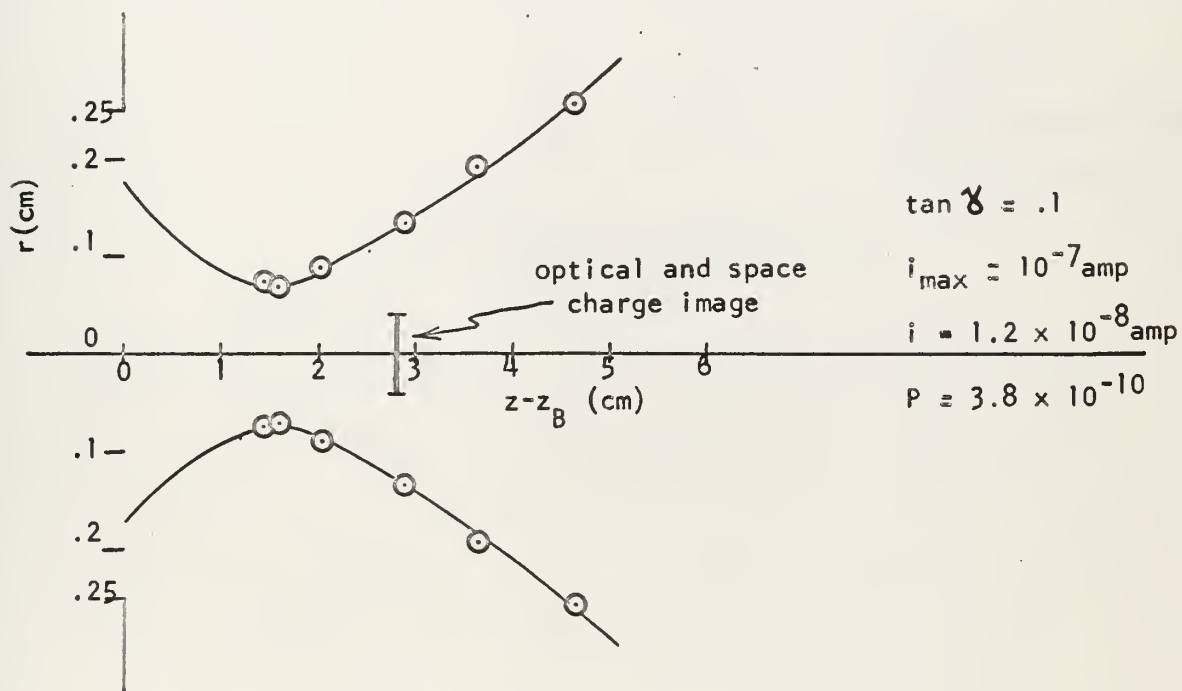


Fig. 16

$$V_0 = 10, \quad V_g/V_a = 2\%, \quad V_a/V_0 = 10$$

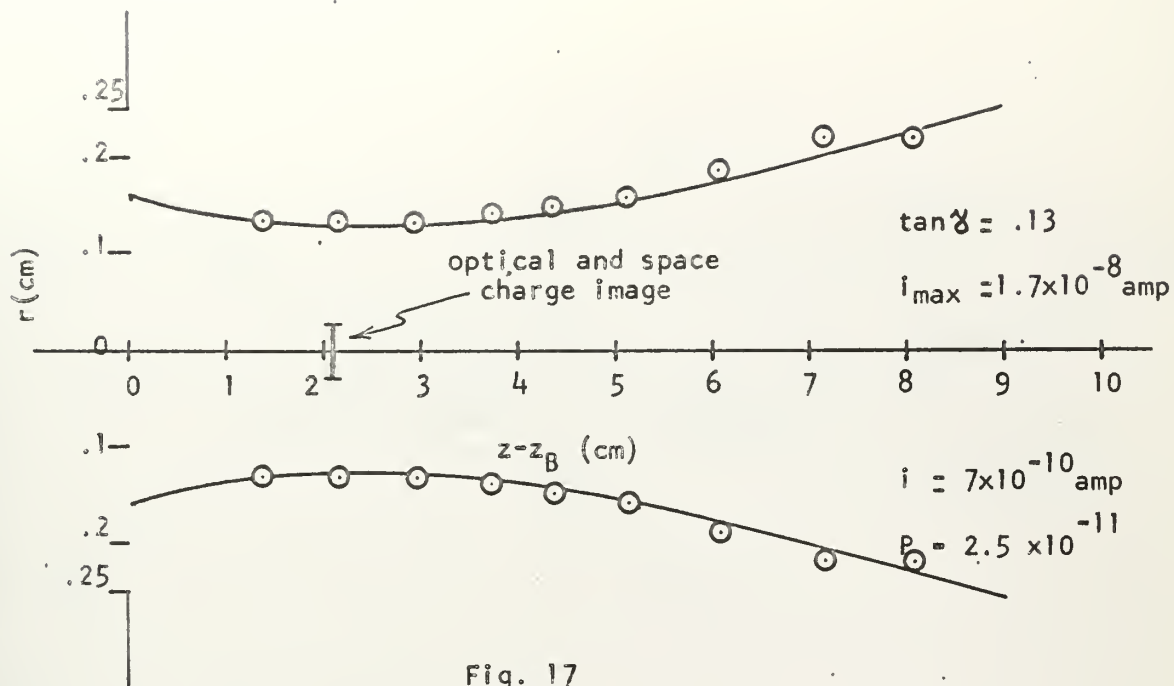


Fig. 17

$$V_0 = 2, \quad V_g/V_a = 2\%, \quad V_a/V_0 = 30$$

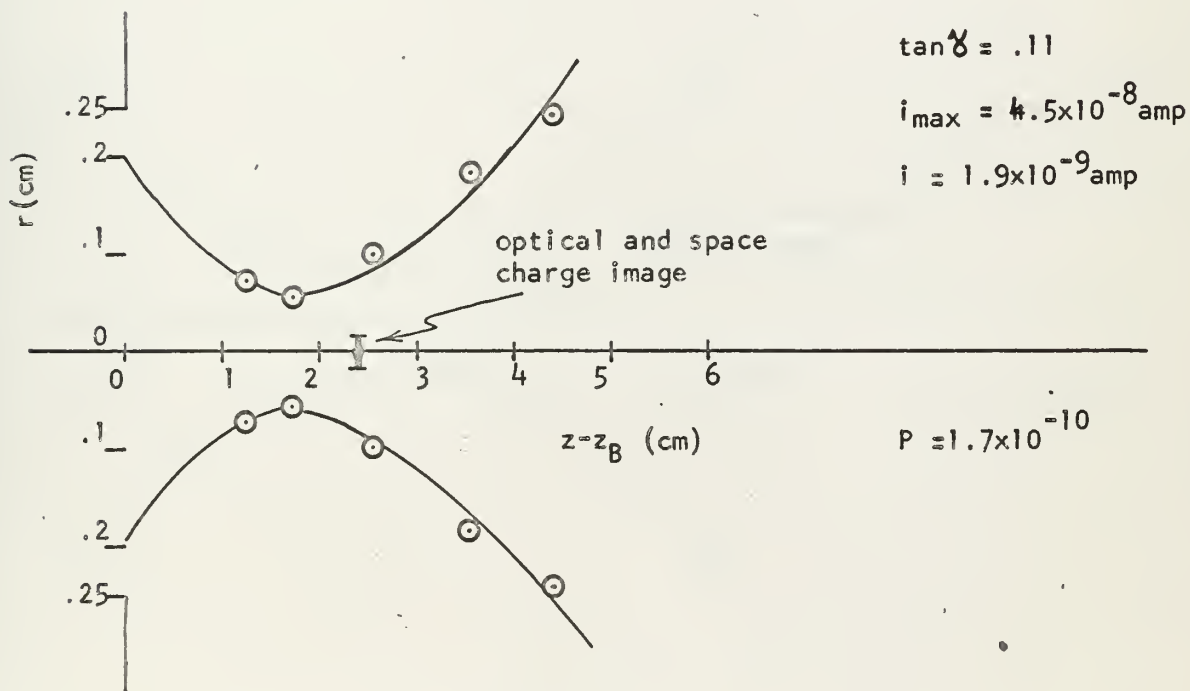


Fig. 18

$$V_0 = 5, \quad V_g/V_a = 1.2\%, \quad V_a/V_0 = 15$$

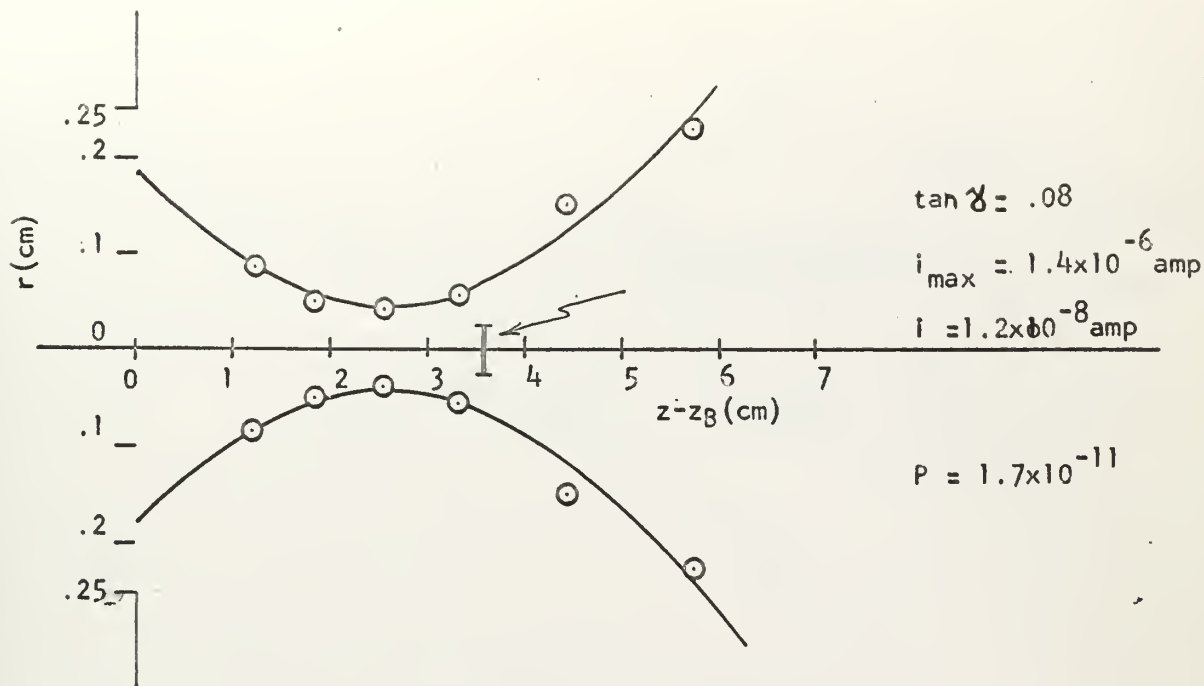


Fig. 19

$$V_0 = 80, \quad V_g/V_a = 1\%, \quad V_a/V_0 = 6$$

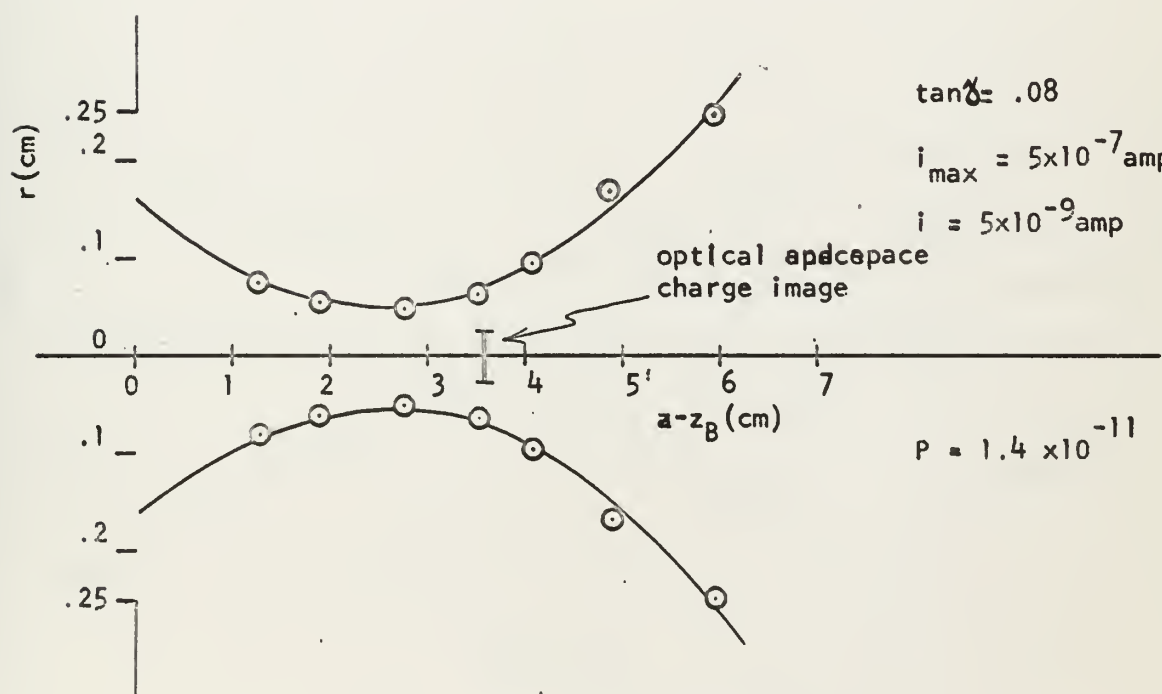


Fig. 20

$$V_0 = 50, \quad V_g/V_a = 1\%, \quad V_a/V_0 = 6$$

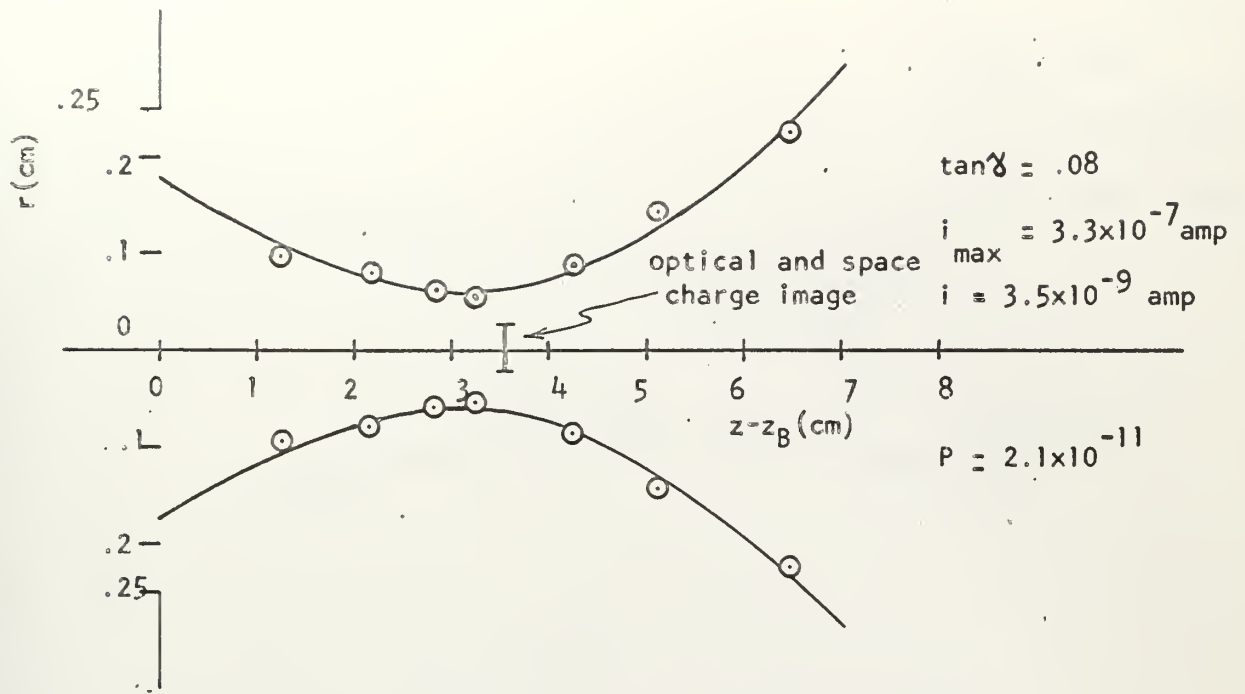


Fig. 21

$$V_0 = 30, \quad V_g/V_a = 1\%, \quad V_a/V_0 = 6$$

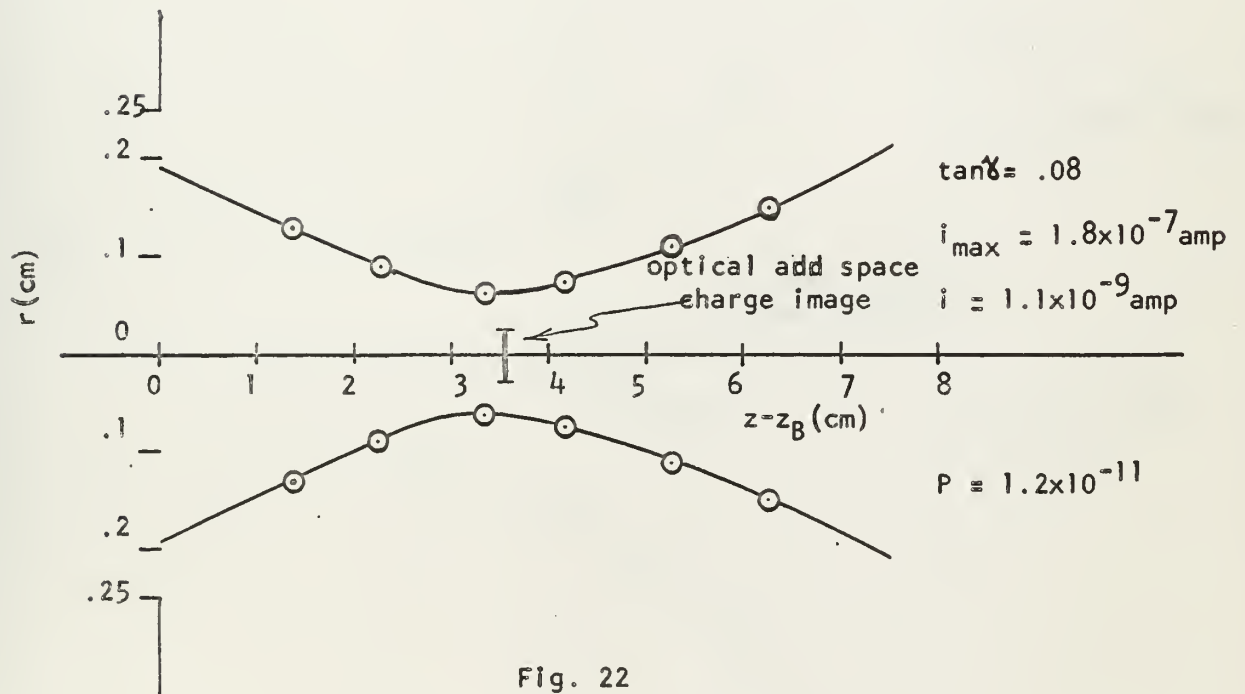


Fig. 22

$$V_0 = 20, \quad V_g/V_a = 1\%, \quad V_a/V_0 = 6$$

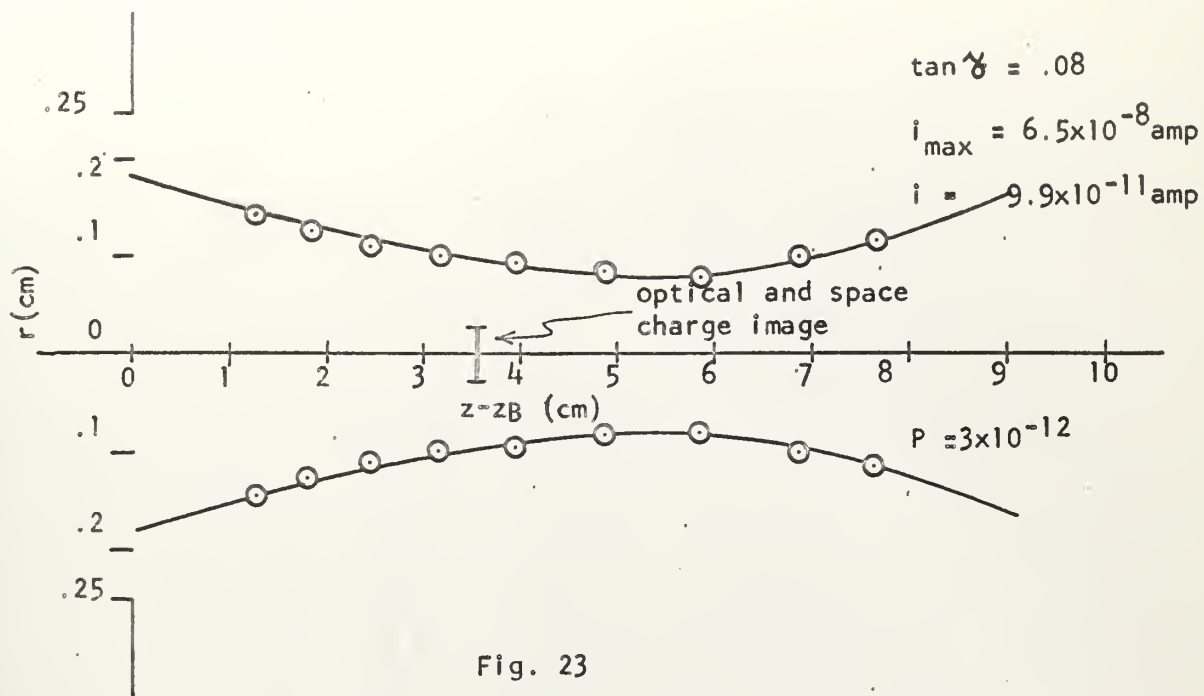


Fig. 23

$$V_0 = 10, \quad V_g/V_a = 1\%, \quad V_a/V_0 = 6$$

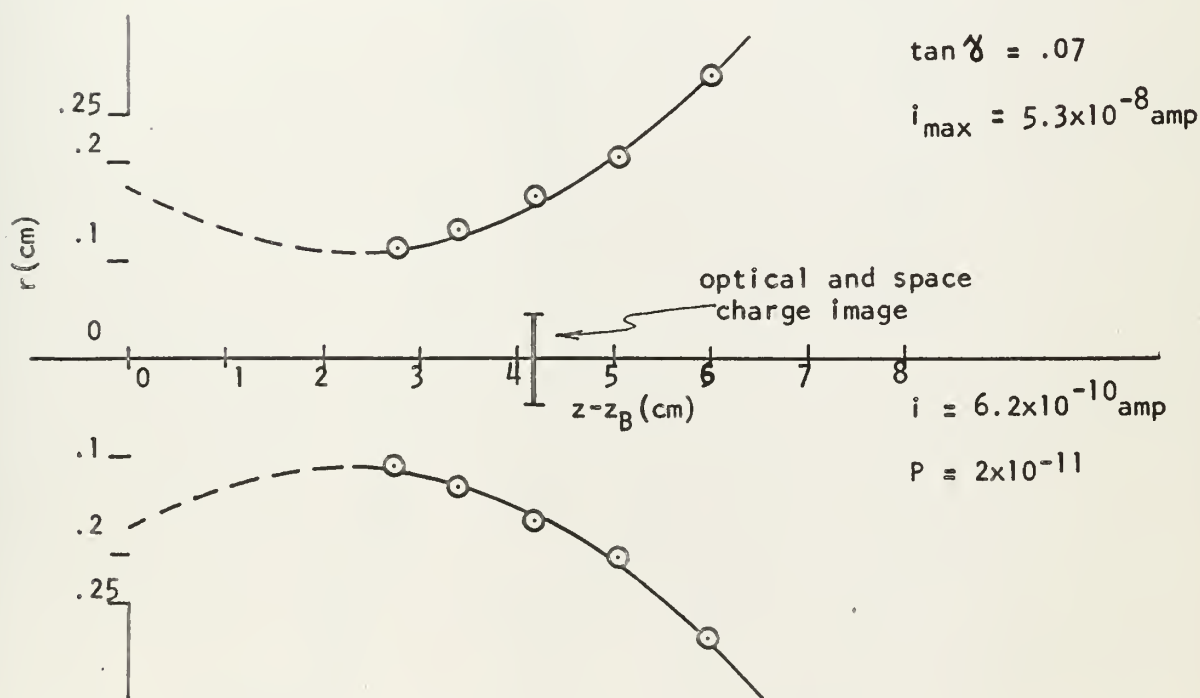


Fig. 24

$$V_0 = 10, \quad V_g/V_a = 1\%, \quad V_a/V_0 = 6$$

$$\tan \chi = .04$$

$$i_{\max} = 4.8 \times 10^{-7} \text{ amp}$$

$$i = 5.5 \times 10^{-9} \text{ amp}$$

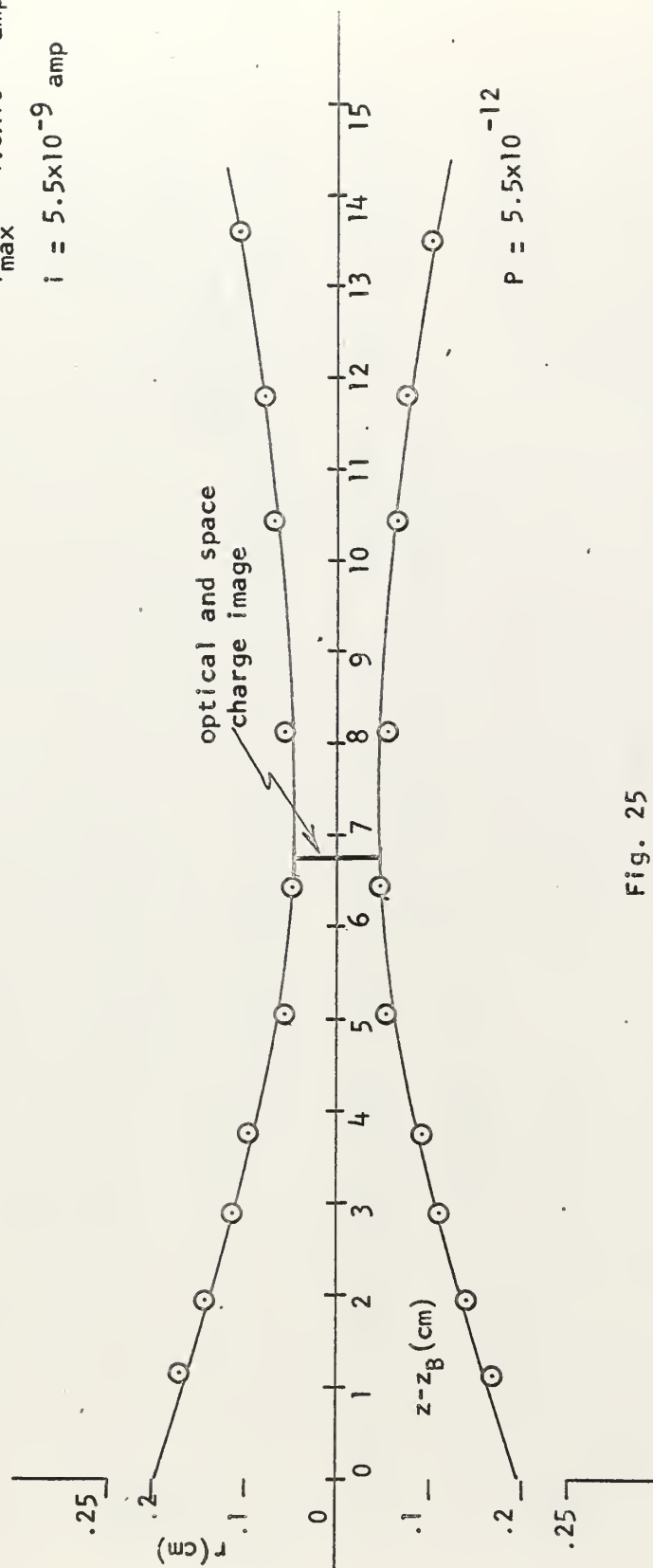


Fig. 25

$$V_0 = 100, \quad V_g/V_a = 1\%, \quad V_a/V_0 = 4$$

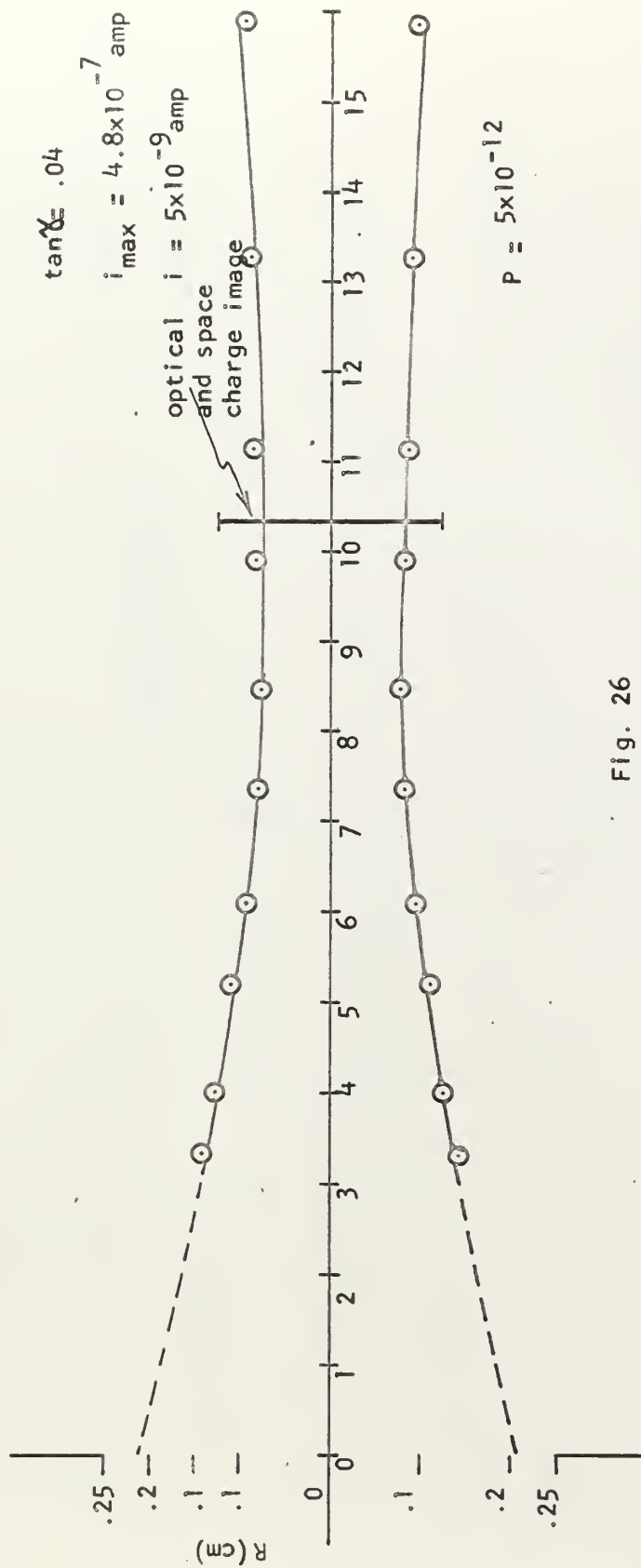


Fig. 26

$$V_o = 100, \quad V_g/V_a = 1\%, \quad V/V_o = 4$$

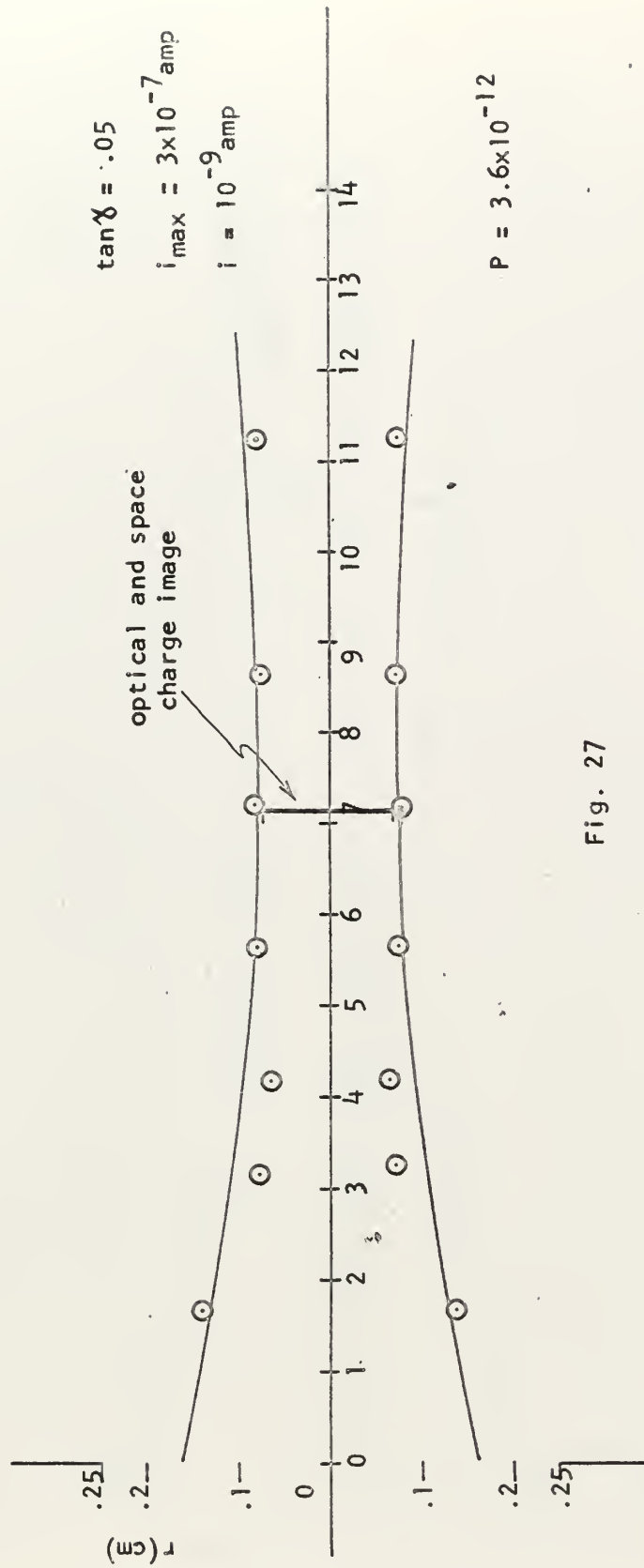


Fig. 27

$$V_0 = 50, \quad V_g/V_a = 1.5\%, \quad V_a/V_0 = 4$$

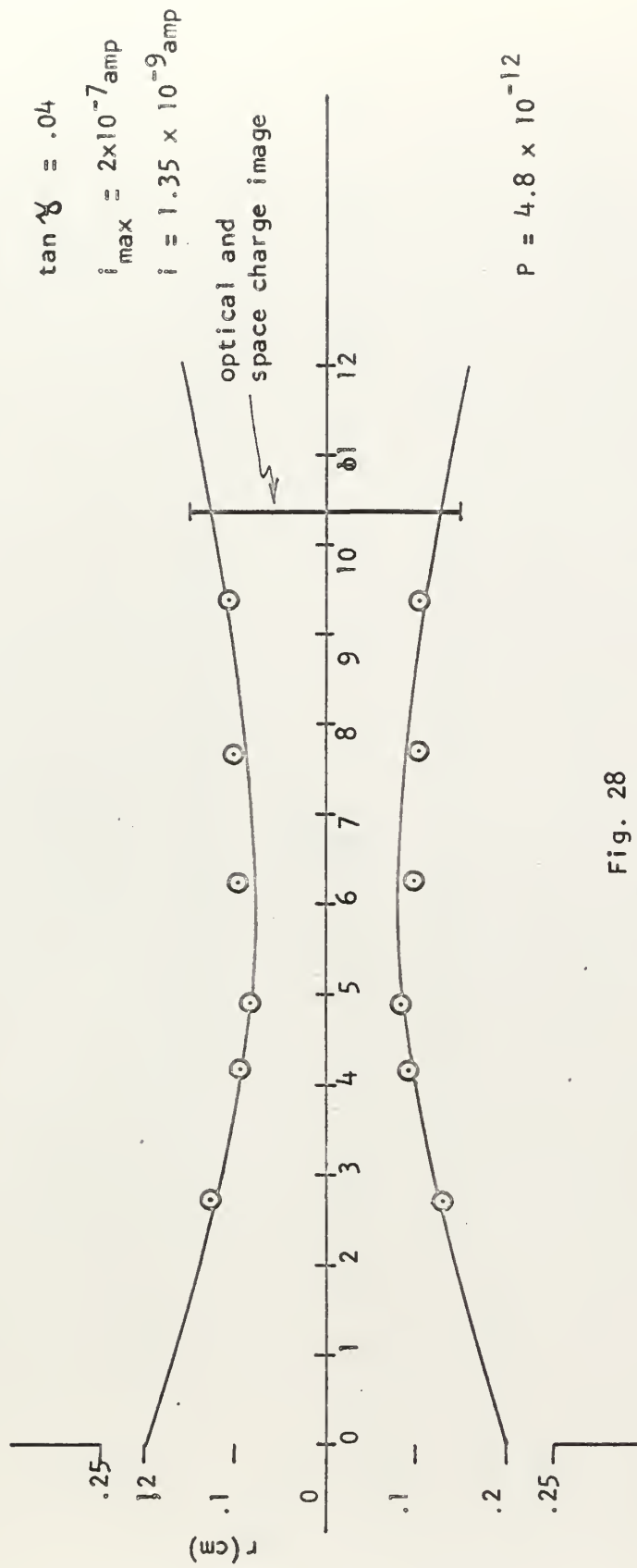


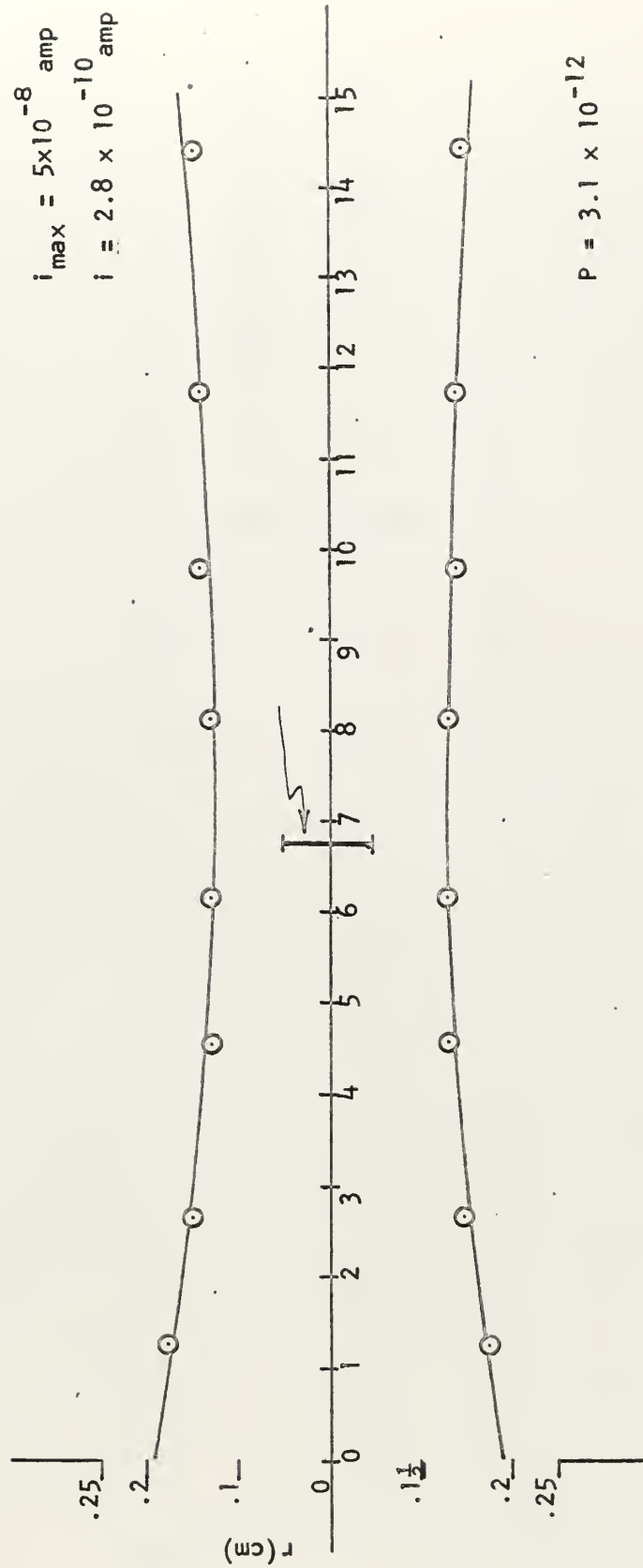
Fig. 28

$V_0 = 50$, $V_g/V_a = 1.5\%$, $V_a/V_0 = 4$

$$\tan \chi = .04$$

$$i_{\max} = 5 \times 10^{-8} \text{ amp}$$

$$i = 2.8 \times 10^{-10} \text{ amp}$$



$$P = 3.1 \times 10^{-12}$$

Fig. 29

$$V_0 = 20, \quad V_g/V_a = 1\%, \quad V_a/V_0 = 4$$

$$\tan \chi = .04$$

$$i_{\max} = 5 \times 10^{-8} \text{ amp}$$

$$i = 5 \times 10^{-10} \text{ amp}$$

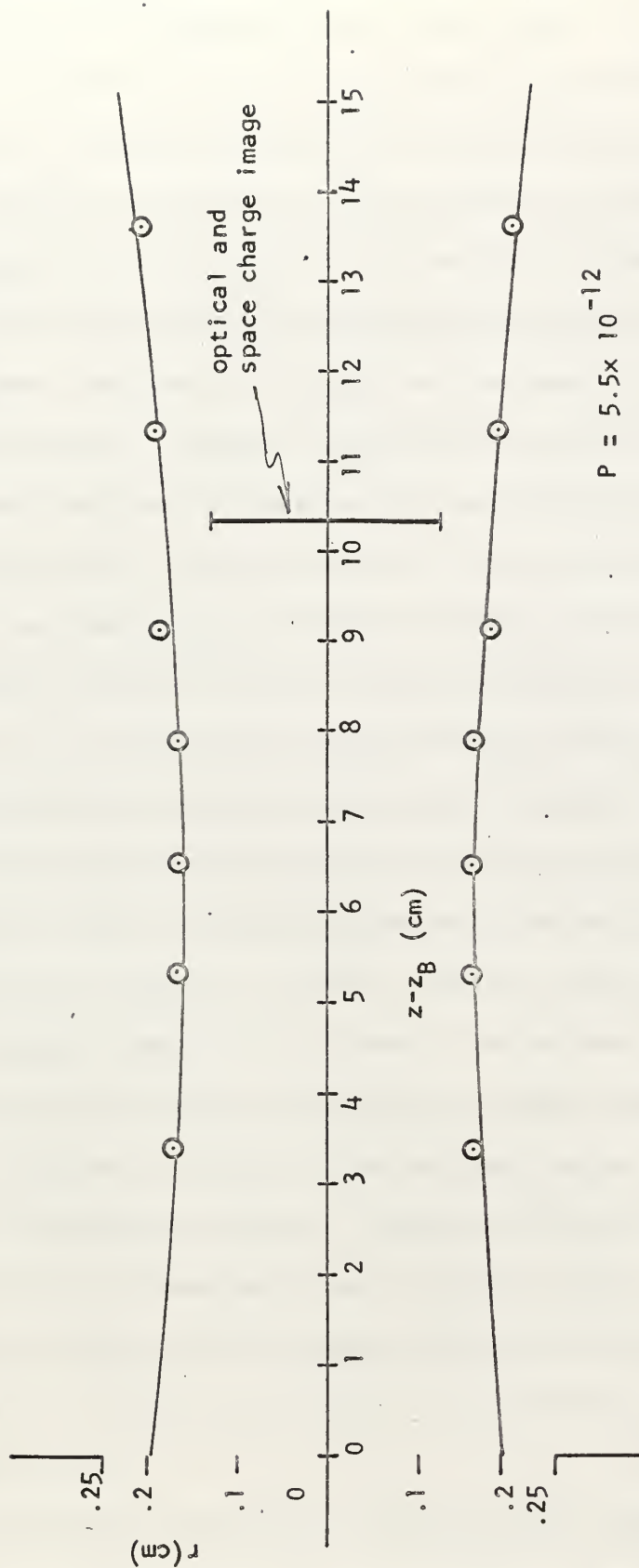


Fig. 30

$$V_o = 20, \quad V_g/V_a = 1\%, \quad V_a/V_o = 4$$

lens performance. The calculated space charge image (Fig. 6-6 to 6-18) is based on the measured beam perveance ($1/V_0^{3/2}$) and the calculated optical image. It should be noted that the theory assumes the current density in the cross-section is uniform and that all the current is contained within a definite region. The analysis of Appendix 5 shows that it is more reasonable to assume a Gaussian current density distribution, and even that does not account for the broad tail on the measured distribution. Perhaps a polynomial distribution would be better, however calculations based on such an assumption are cumbersome and the Gaussian curve gives an adequate fit for the present purposes. In comparing the results given below with theory, one should recall that the experimental profiles shown are those that include only 63% of the total current, (If the Gaussian current density distribution is valid) while the theoretical value given presumably includes all the current.

Four deceleration ratios have been investigated rather extensively, and two others at very low beam energies were used once each. Figs. 11 through 16 are for $V_a/V_0 = 10$. At this ratio the beam is highly convergent and its useful length is, as a result, rather short. There is no theoretical reason why this ratio requires a highly convergent beam, however, the physical structure of the lens made object distances less than 3.5 cm. impossible to attain. Inspection of Fig. 6-4 indicates that for this ratio the maximum focal distance is then ~ 5 cm., or ~ 4 cm. from the final aperture and the magnifications are small, hence the optical image is relatively small and close to the lens, which gives larger values of γ .

Figs. 13 through 16 illustrate that the focal properties of the lens are relatively insensitive to beam perveance. The beam voltage and step down ratio were held constant while the grid bias was varied.

This changed the optical properties only slightly but allowed the beam perveance to vary over an order of magnitude. Nevertheless the beam profile is relatively unchanged.

Fig. 17 is for a beam voltage of ~ 2 volts (voltage measurements in this range are quite uncertain due to the limitations of the voltage divider network. See Appendix 3). Note that while the actual image is very much larger than the optical one the beam is not highly convergent and the beam is useful out to ~ 8 cm. This is attributed to the defocusing effect of the inter-stage space charge spreading discussed above.

Fig. 18 is for 5 v beam voltage. Here the defocusing effect is not so strong and the beam becomes more convergent.

Figs. 19 through 24 are for $V_a/V_0 = 6$. This ratio permits lower values of χ and so the beam is usable to larger distances than with $V_a/V_0 = 10$. However, the currents are reduced accordingly at all values of beam voltage. Figs. 23 and 24 show the effect of inter-stage defocusing. The object distance for Fig. 23 was 10 cm. and for Fig. 24, 7 cm. That the inter-stage space charge losses are less in the second case is demonstrated by the higher current. However, in spite of the fact that the optical image has moved out by almost 1 cm. the actual focus has moved in by about 3.5 cm. The higher perveance can account for the close in focus in the second case, while the extended focus in the first case can be accounted for by the defocusing effect of the inter-stage beam spreading.

Figs. 25 through 30 are for $V_a/V_0 = 4$. If the lower currents can be tolerated this region gives the most useful beams, being less than 4 mm in diameter out to as much as 16 cm. from the lens. In these curves the inter-stage defocusing is also evident. As the optical

focus is moved out by 3 to 3.5 cm. the actual focus is increased only for $V_0 \approx 100\text{v}$ where the effect should be a minimum and actually decreases in the other two cases as would be the case if the inter-stage defocusing were sharply reduced by reducing the inter-stage distance. In two of the above cases the measured beam profile is smaller than the optical image. This may be accounted for by noting that the measured profile contains only 63% of the beam.

Examination of Fig. 6-5 indicates that magnification of the extraction stage is relatively constant for values of grid bias $\lesssim 2\%$, and increases rapidly above that value. Similarly, values of extraction stage image distance also increase rapidly when grid bias is $\gtrsim 2\%$. Hence it can be seen that operation above this range of grid bias makes the two stages incompatible, in that the object for the deceleration stage may well be larger than its apertures and may be outside the limits of travel of the deceleration stage. Thus operation at grid bias $>2\%$ may give higher total currents due to increased output from the emitter, but the lens focal properties are largely lost and some means external to the gun (such as a system of slits) must be used to define a beam.

(c) Extraction Stage Perveance

Fig. 6-5 gives the characteristics of the Soa extraction stage. It is utilized to fix the grid bias and to determine the size and location of the image of this stage. The grid bias is normally determined by entering the curve with the required value of P_e , defined by

$$P_e = i/V_a^{3/2} \quad (3)$$

where i is expressed in μamp and is obtained from equation (1). For electrons the useful range of this parameter is $\sim 10^3$. The range for Lithium should be ~ 10 after correcting for the mass ratio. The

values of P_e were computed for the beams investigated, and when plotted seemed to fit a curve of the shape of that found by Simpson and Kuyatt but whose range was ~ 1 . This additional factor of 10 reduction in values over that for electrons is attributed to the lower emission rate for the emitter and the inter-stage losses discussed above. As a practical matter, the required value of P_e for Lithium as determined by the method of Appendix 6 should be reduced by a factor of 100 prior to entering Fig. 6-5, to account for the expected loss in current over that predicted by equation (1).

As an example of the use of Fig. 6-5, assume we have an expected value of P_e of 3. Entering the dashed curve with this value gives a desired grid bias of 1.25%. With this bias we get, from the other two curves $M = .5$, and $Q/d_k = 5.8$.

(d) Mass Analysis

Fig. 31 gives the results of the mass analysis. As can be seen, the percent impurities at the operating temperatures is quite low. The beam is almost pure Li^7 . It has also been reported by other investigators that the heavier alkali impurities (Na^+ , K^+) tend to decrease in time, thus further increasing the Li^+ content of the beam.

(e) Energy Spread of the Ion Beam

A careful study of the beam energy spread is now underway but no definite results are available at this time. Preliminary indications are that the beam is not mono-energetic but may have a ΔE of a few eV. It is believed that this energy spread is inherent in the construction of the emitter, rather than in the lens system. However, a final conclusion with regard to the system's energy resolution must await the results of the energy measurements.

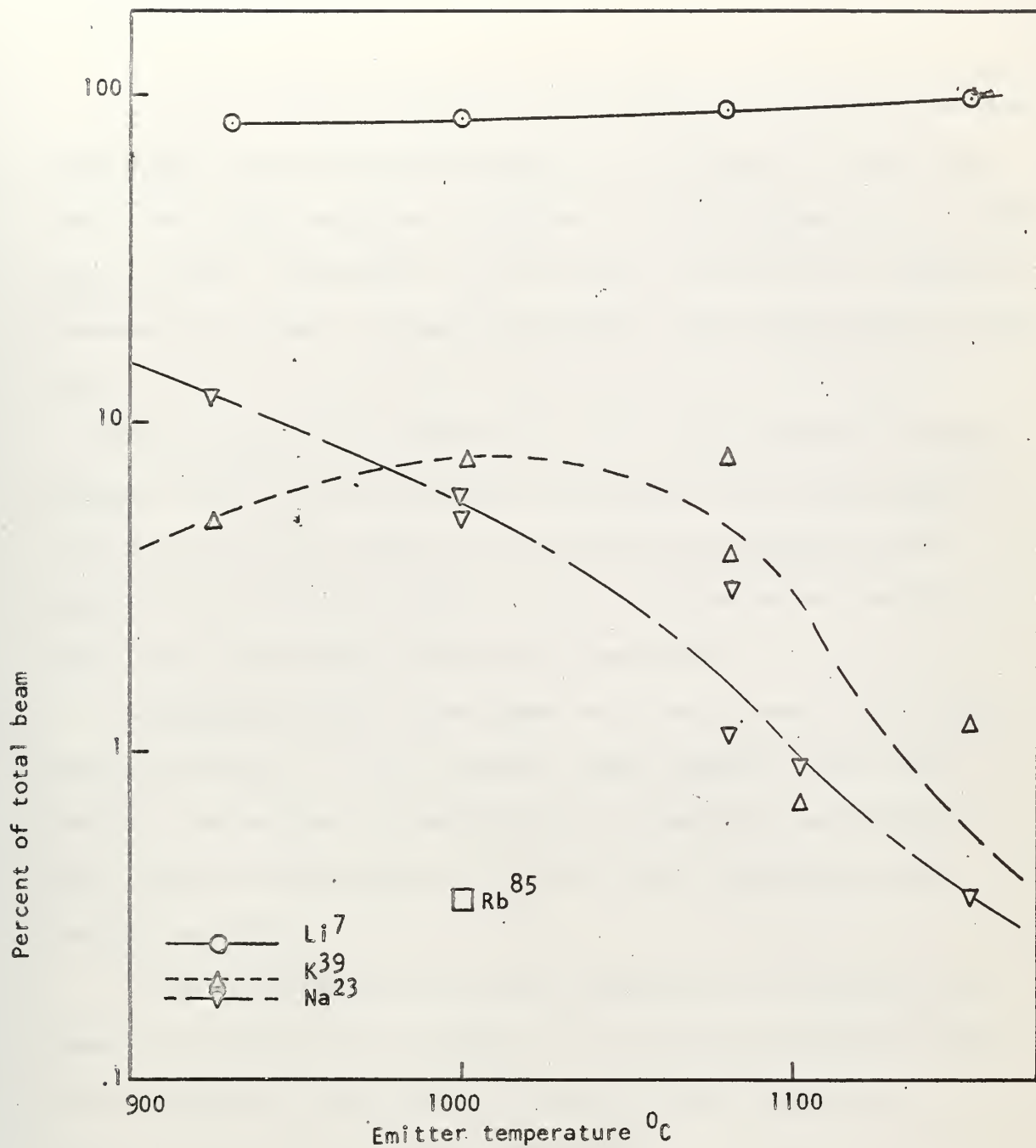


Fig. 341

Mass Analysis*

*Data taken by Drs. J.R. Peterson and W. Aberth of Stanford Research Institute

4. Conclusion

The above data indicates that a multistage lens system of the type investigated here performs approximately as predicted by theory and that under proper conditions a thin, well collimated beam in the 1-100eV energy region is obtainable. The ion optics observed are in reasonable agreement with theory, the major discrepancy being total current predictions.

The gun under investigation used a Li^7 source, however, suitable changes in the operating parameters should make this system useable with any of the alkali ions, or in fact with any charged particle capable of emission from a plane surface. For the source used the impurities in the beam are essentially negligible.

Although the energy spread seems not to be as small as desirable at this writing, it is felt that this effect depends mainly on the emitter used and that the desired energy spreads will be obtainable with improved emitter design. This should also improve the total currents available.

A small additional current may be obtainable by increasing the opening of aperture one to perhaps .3 cm. The gun was found to work more satisfactorily when the aperture was present, however, so leaving it out entirely is not recommended.

In order to be able to work at smaller object distances, the extraction stage in any permanent apparatus should be made a fixed part of the emitter structure. This would allow the deceleration stage to be moved closer to the extraction stage and would provide protection against inadvertent touching of the grid to the emitter. Aperture one can also be safely moved up to .5 cm from the extraction

electrode.

The voltage divider network used in this investigation is discussed in Appendix 3. As noted there is not an acceptable design for a permanent installation and any continuing use of this gun should involve a more useful means of setting and measuring the electrode potentials.

Incorporation of the improvements noted above should make this gun a versatile research tool in the study of low energy atomic collision processes.

5. Acknowledgements

It is a pleasure to acknowledge the support and encouragement of Dr. Otto Heinz of the Naval Postgraduate School faculty at whose suggestion this project was undertaken. Dr. W. Aberth of Stanford Research Institute has kindly provided the energy analysis of their ion beam and with Dr. J.R. Peterson, the reported mass analysis. Dr. D.C. Lorents of Stanford Research Institute along with Drs. Aberth and Peterson contributed several valuable suggestions and numerous discussions. I wish to thank also Dr. J.A. Simpson of the National Bureau of Standards for calling my attention to several aspects of the problem that I had overlooked, as well as several suggestions regarding the design. LT Frank Hauck of the Postgraduate School provided an excellent translation of Glaser's calculations. Finally, I am indebted to Messrs. M.K. Andrews, R. Moeller, and M.J. O'Dea of the Postgraduate school technical staff for their assistance in constructing the gun.

BIBLIOGRAPHY

- 1927 Watson, E.E., "Dispersion of an Electron Beam," Phil. Mag., 3, 849, 1927
- 1939 Pierce, J.R. "Limiting Current Densities in Electron Beams," J. Appl. Phys., 10, 715, 1939
- 1940 Pierce, J.R. "Retilinear Electron Flow in Beams", J. Appl. Phys., 11, 548, 1940
- 1943 Spangenberg, K., and Field, L.M., "The Measured Characteristics of Some Electrostatic Electron Lenses", Elect. Commun. 21, 194, 1943
- 1944a Terril, H.M. and Sweeny, L., "Table of the Integral of e^{x^2} ", J. Franklin Inst., 237, 495, 1944
- 1944b Terril, H.M. and Sweeny, L., "Table of the Integral of e^{x^2} ", J. Franklin Inst., 238, 220, 1944
- 1945 Jahnke, E. and Emde, F., Tables of Functions, Dover, 1945.
- 1948 Wendt, G., "The Spreading of an Electron Optical Pencil Under the Influence of its Own Charge," Ann. d. Physik, 2, 256, 1948
- 1952 Glaser, W., Grundlagen der Electronenoptik, Springer-Verlag, 1952, p 69 ff.
- 1953 Klemperer, O., Electron Optics, Cambridge, 1953
- 1954 Pierce, J.R. Theory and Design of Electron Beams, 2nd Ed., Van Nostrand, 1962.
- 1959 Soa, E.A., "Sydtematische Untersuchungen an Elektrostatischen Inmersions Objectiven" Janaer Jahrbuch, 1, 115, 1959.
- 1962 Johnson, F.M., "Studies of the Ion Emitter Beta-Eucryptite," RCA Review, 22, 427, 1962.
- 1963a Lagerstrom, R.P., "Ion and Plasma Beam Sources," Quarterly Research Review No. 4, Stanford Electronic Laboratories, 1 Jan to 31 March 1963, p. 1-33ff.
- 1963b Lambert, W.W., Production and Analysis of Lithium Ion Beams in the Low Electron Volt Region, Thesis, (M.S.), USNPGS, Monterey, Cal, 1963
- 1963c Simpson, J.A. and Kuyatt, C.E., "Design of Low Voltage Electron Guns," Rev. Sci. Instr., 34, 265, 1963.

- 1963d Simpson, J.A. and Kuyatt, C.E., "Limitations on Electron Beam Densities of Unipotential Electron Guns at Low Voltages." J. Res. NBS, 67C, 297, 1963.
- 1964 Eager, W.J., Elastic Scattering of 1-100eV Lithium Ions in Helium, Thesis (M.S.), USNPGS, Monterey, Cal, 1964
- 1965 Lorents, D.C., Black, G. and Heinz, O. "Charge Transfer Between Li Ions and Li Atoms in the 14-1000eV Energy Region," Phys. Rev., 137, A1049, 1965.

APPENDIX 1

Mass Independence of the Trajectory of a Charged Particle in an Axially Symmetric Electrostatic Field

The force on a particle of mass m and charge e in an axially symmetric electrostatic field \underline{E} is given by

$$\underline{F} = e\underline{E}$$

where

$$\begin{aligned}\underline{E} &= -\nabla V \\ &= -\frac{\partial V}{\partial r} \underline{r}_0 - \frac{1}{r} \frac{\partial V}{\partial \phi} \underline{\phi}_0 - \frac{\partial V}{\partial z} \underline{z}_0\end{aligned}$$

in cylindrical co-ordinates. By assumption of axi-symmetry $\partial V / \partial \phi = 0$ and V is a function of r and z only. Now the element of arc length in cylindrical co-ordinates is

$$ds = dr \underline{r}_0 + r d\phi \underline{\phi}_0 + dz \underline{z}_0$$

whence

$$\frac{ds}{dt} = \underline{\dot{R}} = \dot{r} \underline{r}_0 + r \dot{\phi} \underline{\phi}_0 + \dot{z} \underline{z}_0$$

and

$$\underline{\ddot{R}} = \ddot{r} \underline{r}_0 + \dot{r} \dot{\phi} \underline{\phi}_0 + r \ddot{\phi} \underline{\phi}_0 + \ddot{z} \underline{z}_0$$

where \underline{R} is the position vector to the point at which ds is measured.

If we assume the initial velocity to be 0, then

$$\dot{\phi} = \ddot{\phi} = 0$$

and we write the force equation as

$$m \underline{\ddot{R}} = \ddot{r} m \underline{r}_0 + \ddot{z} m \underline{z}_0 = -e \frac{\partial V}{\partial r} \underline{r}_0 - e \frac{\partial V}{\partial z} \underline{z}_0$$

so the equations of motion can be written

$$\ddot{r} = -e/m \frac{\partial V}{\partial r} = -e/m V_r,$$

$$\ddot{z} = -e/m \frac{\partial V}{\partial z} = e/m V_z. \quad (1-1)$$

The total energy is

$$W_0 = eV + \frac{m}{2} (\dot{r}^2 + \dot{z}^2) \quad (1-2)$$

and the kinetic energy is then

$$T = W_0 - eV \quad (1-3)$$

which can be expressed as

$$T = e(V_0 - V) \quad (1-4)$$

for the conditions of 0 initial velocity. Putting (1-3) into (1-2) gives

$$\dot{r}^2 + \dot{z}^2 = 2T/m$$

whence

$$1 + \left(\frac{dz}{dr}\right)^2 = 2T/m\dot{r}^2. \quad (1-5)$$

Let

$$\frac{dz}{dr} = z',$$

then

$$\frac{d}{dr} (1 + z'^2) = \frac{d}{dr} (2T/m\dot{r}^2),$$

so

$$2z'z'' = \frac{2}{m} \left[T'/\dot{r}^2 + T \frac{d}{dr} (1/\dot{r}^2) \right]$$

where

$$T' = e(V_r + V_z z')$$

and

$$\frac{d}{dr} (1/\dot{r}^2) = -2\ddot{r}/\dot{r}^4 = -(2e/m\dot{r}^4)V_r$$

from (1-1). Hence

$$z' z'' = e/m\dot{r}^2 \left[(2T/m\dot{r}^2 - 1) V_r - V_z z' \right]$$

and from (1-5) we have

$$z'' = e/m\dot{r}^2 (z' V_r - V_z).$$

Applying (1-5) again

$$z'' = \frac{e}{2T} (1+z'^2) (z' v_r - v_z). \quad (1-6)$$

Substituting (1-4) into (1-6) we get

$$z'' = (1+z'^2) (z' v_r - v_z) / 2 (v_o - v) \quad (1-7)$$

which is the differential equation of the trajectory and is independent of the mass of the particle.

Thus we can see that the "optical" properties of an electrostatic lens, once determined for, say, electrons, should be valid for any particle of the same charge, provided that the initial velocity of the particle is negligible compared to the total energy. Such a condition is usually met by thermionic ion emitters.

It can also be shown that the trajectory equations are mass independent for arbitrary electrostatic fields, however the calculation is much more cumbersome and the above development will be sufficient for our purposes.

APPENDIX 2

Beam Spreading due to Space Charge.

Following Glaser (1952) and based on an analysis due to Watson (1927) and Wendt (1948) we shall consider a beam of charged particles of sufficient density to be considered a continuous medium for the purpose of constructing energy functions. As the beam leaves an aperture of radius R_B the rays emanating from the edge are initially directed as in Fig. 2-1, and those from the interior points are contained within the outer rays so as to be focused toward a spot of radius r_a a distance L away. The origin of co-ordinates is such that the beam axis is the z axis; the co-ordinate of the aperture is z_B and of the focal point, z_a . The beam is symmetric about the z axis.

The effect of the space charge of the beam is to deflect the rays away from the axis. We assume that the current density is uniform across the beam cross section and zero outside the outer rays, and that the total current is constant. If the convergence of the rays is sufficiently small then a small segment of the beam forms a cylinder of nearly constant radius in which the axial forces are nearly 0, and hence the axial velocity z is very nearly constant and given by

$$\dot{z} \approx \sqrt{2eV/m} \quad (2-1)$$

We shall now proceed to calculate the trajectories of the outer and inner rays as shown in Fig. (2-1) under the influence of space charge in field free space, subject to the simplifying assumptions given above.

a. Trajectory of the Outer Ray

The radial component of the electric field due to the space charge

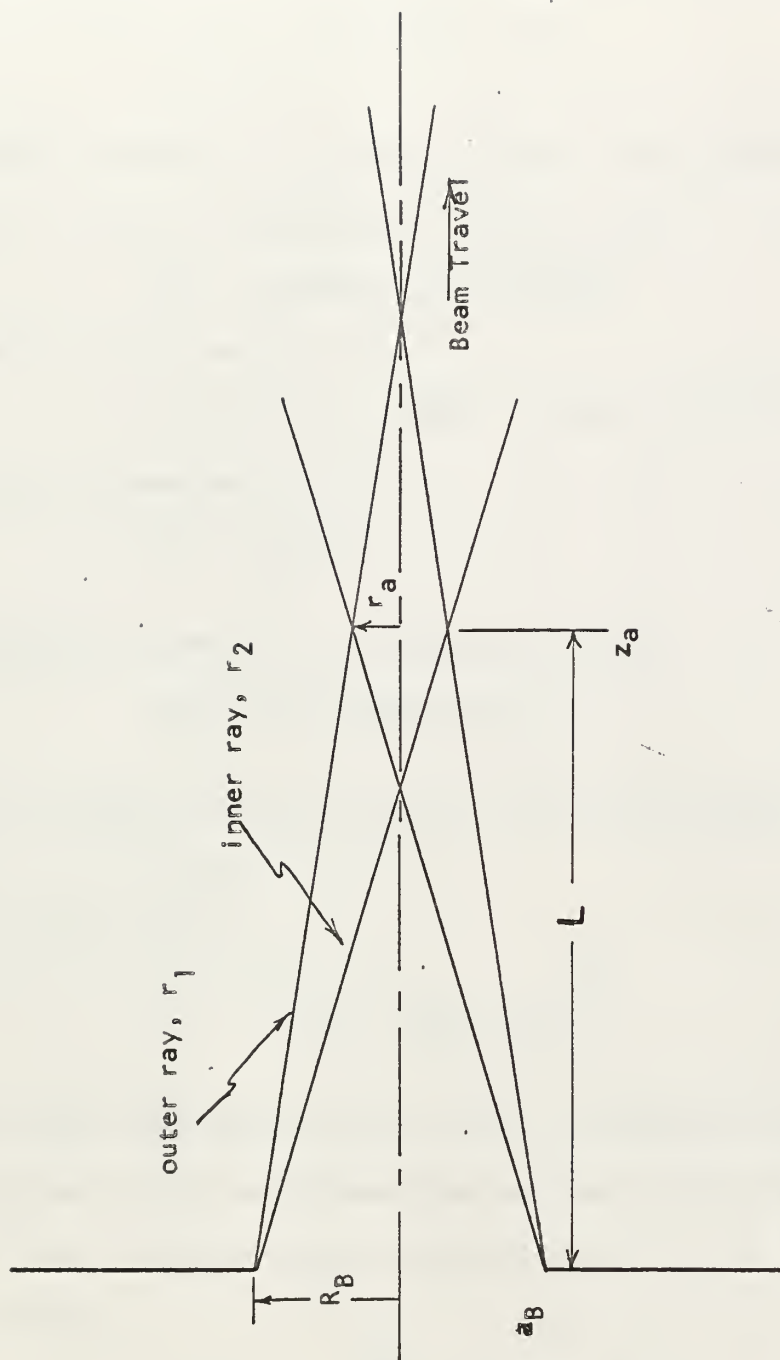


Fig. 2-1

Optical Ray Pattern of Focused Beam

can be written

$$E_{r_1} = (i/2\pi\epsilon_0 r_1) \sqrt{m/2eV} \quad (2-2)$$

where i is the total current, eV is the beam energy, and r_1 is the radius of the outer ray at any point. Let

$$\eta = e/m$$

be the charge to mass ratio of the particles. The radial equation of motion of a particle on the outer ray is, then

$$m\ddot{r}_1 = (ei/2\pi\epsilon_0 r_1) (1/\sqrt{2\eta V}). \quad (2-3)$$

If we define, using the mass of Li^7 ,

$$K_1 = i/(2\pi\epsilon_0 \sqrt{2\eta V}) = 3.4273 \times 10^6 iV^{-\frac{1}{2}} \quad (2-4)$$

in mks units, we may write (2-3) as

$$\ddot{r}_1 = K_1 \eta / r_1. \quad (2-5)$$

Multiplying both sides by r_1 and integrating gives

$$\frac{1}{2} \dot{r}_1^2 = K_1 \eta \ln(r_1/r_0) \quad (2-6)$$

where the constant of integration r_0 is chosen such that at

$$r_1 = r_0, \dot{r}_1 = 0.$$

From (201) we have

$$\dot{r}_1 = - \dot{z} \left[\frac{K_1}{V} \ln(r_1/r_0) \right]^{\frac{1}{2}} \quad (2-7)$$

where we choose the negative root in order to restrict consideration to the portion of the beam between the aperture and the focal point, i.e. the region where the beam is convergent and $\dot{r}_1 < 0$. This gives on integration

$$z - z_B = - \int_{R_B}^{r_1} \left[\frac{K_1}{V} \ln(r'_1/r_0) \right]^{-\frac{1}{2}} dr'_1$$

where the primes denote variables of integration.

Finally, setting

$$s = [\ln(r_1/r_0)]^{\frac{1}{2}} \quad (2-8)$$

we find

$$z - z_B = -2K \int_{s_B}^s \exp\{s'^2\} ds' \quad (2-9)$$

where

$$K = r_0 \sqrt{V/K_1} = 5.4016 \times 10^{-4} r_0 V^{3/4} / i^{\frac{1}{2}}$$

which becomes, when we define the perveance

$$P = i/v^{3/2} \quad (2-10)$$

$$K = 5.4016 \times 10^{-4} r_0 / P^{\frac{1}{2}}. \quad (2-11)$$

If we define the Dawson function

$$D(s) = \int_0^s \exp\{s'^2\} ds' \quad (2-12)$$

then (2-9) becomes

$$z - z_B = -2K [D(s) - D(s_B)] . \quad (2-13)$$

Tables of $D(s)$ are available, (1944a, 1944b, 1945) and (2-13) may then be evaluated in terms of $r_0/P^{\frac{1}{2}}$.

b. Trajectory of the inner ray

We know from Gauss' law that only the charge enclosed by the inner ray will affect its trajectory. Assuming a uniform radial charge distribution in the beam cross section the ratio of currents included within each ray varies as r_2^2/r_1^2 and since the field depends only on the enclosed charge we have immediately, using (2-2) and (2-4)

$$E_{r_2} = K_1 r_2/r_1^2 \quad (2-14)$$

whence the radial equation of motion of a particle on the inner ray is

$$r_2 = \eta K_1 r_2 / r_1^2 \quad (2-15)$$

where r_1 is given by

$$r_1 = r_0 \exp \{s^2\} \quad (2-16)$$

from (2-8).

We may differentiate r_2 parametrically as

$$\frac{dr_2}{dt} = \frac{dr_2}{ds} \frac{ds}{dr_1} \frac{dr_1}{dt} = \frac{dr_2}{ds} \frac{ds}{dr_1} \dot{r}_1$$

where r_1 is given by (2-6). ds/dr_1 may be found from (2-8), giving

$$\dot{r}_2 = \sqrt{2K_1\eta} \frac{\exp \{-s^2\}}{2r_0} \frac{dr_2}{ds} \quad (2-17)$$

and

$$\ddot{r}_2 = K_1 \eta \frac{\exp \{-2s^2\}}{2r_0^2} \left(\frac{d^2 r_2}{ds^2} - 2s \frac{dr_2}{ds} \right). \quad (2-18)$$

Putting (2-18) in (2-15) gives

$$\frac{d^2 r_2}{ds^2} - 2s \frac{dr_2}{ds} - 2r_2 = 0 \quad (2-19)$$

which has the solution

$$r_2 = C_1 \exp \{s^2\} \left[1 + C_2 \phi(s) \right] \quad (2-20)$$

where C_1 and C_2 are constants of integration, and

$$\phi(s) = (2/\sqrt{\pi}) \int_0^s \exp \{-s'^2\} ds'. \quad (2-21)$$

$\phi(s)$ is the error function and is extensively tabulated (1945).

We evaluate the constants of integration by noting that at $z = z_B$
(See Fig. 2-1)

$$r_{1B} = r_{2B} = R_B$$

and

$$\begin{aligned}\left(\frac{dr_1}{dz}\right)_B &= -(R_B - r_a)/L, \\ \left(\frac{dr_2}{dz}\right)_B &= -(R_B + r_a)/L.\end{aligned}\quad (2-22)$$

Note also that

$$\frac{dz}{dr_1} = -2K \frac{d}{dr_1} \int_0^s \exp\{s'^2\} ds'$$

from (2-9). Applying Leibniz' rule gives

$$\frac{dz}{dr_1} = -2K \frac{ds}{dr_1} \exp\{s^2\} = -K/r_0 s.$$

So

$$\frac{dr}{dz} = -r_0 s/K$$

and

$$\left(\frac{dr_1}{dz}\right)_B = -r_0 s_B/K, \quad (2-23)$$

whence

$$s_B = K(R_B - r_a)/r_0 L \quad (2-24)$$

From (2-16)

$$R_B/r_0 = \exp\{s_B^2\}$$

so

$$r_0 = R_B \exp\left\{-2.9177 \times 10^{-7} \left(\frac{r_a}{R_B} - 1\right)^2 R_B^2/L^2 P\right\}. \quad (2-25)$$

Now from (2-20)

$$R_B = c_1 \exp\{s_B^2\} [1 + c_2 \phi(s_B)] \quad (2-26)$$

and

$$\frac{dr_2}{dz} = c_1 \exp\{s^2\} \frac{dr_1}{dz} \frac{ds}{dr_1} \left[2s(1 + c_2 \phi) + c_2 \cdot \frac{d\phi}{ds} \right]. \quad (2-27)$$

Applying Leibniz' rule to (2-21) gives

$$\frac{d\phi}{ds} = \frac{2}{\sqrt{\pi}} \exp \{-s^2\} \quad (2-28)$$

and

$$\frac{ds}{dr_1} = 1/2sr_1. \quad (2-29)$$

Putting (2-23), (2-28), (2-29), and the second equation of (2-22) into (2-27) and evaluating at $r_2 = R_B$, gives

$$(R_B + r_a)/L = \frac{C_1}{K} \left[s_B (1 + C_2 \phi_B) + \frac{C_2}{\sqrt{\pi}} \exp \{-s_B^2\} \right] \quad (2-30)$$

where ϕ_B is $\phi(s_B)$. Solving (2-26) for C_1 and putting this and (2-24) in (2-30) gives

$$C_2/(1 + C_2 \phi_B) = 2 \sqrt{\pi} K R_B r_a/r_o^2 L$$

Let

$$N = 2 \sqrt{\pi} K R_B r_a/r_o^2 L = 1.9148 \times 10^{-3} R_B r_a/r_o L P^{\frac{1}{2}} \quad (2-31)$$

Using (2-11). With this we have immediately

$$C_2 = N/(1 - N \phi_B) \quad (2-32)$$

and from (2-26)

$$C_1 = r_o (1 - N \phi_B). \quad (2-33)$$

so the complete solution for r_2 is given by

$$r_2 = r_o \exp \{s^2\} [1 - N (\phi_B - \phi)] \quad (2-34)$$

where r_o is given by (2-25), N by (2-31), s_B by (2-24), and ϕ by (2-21)

c. Calculation of minimum beam radius

The spreading of the rays is shown in Fig. (2-2). If the beam perveance is less than a certain critical value P_{cr} , then the outer ray will be intersected by the inner ray originating diametrically opposite in the aperture at some point, z_F , before r_1 reaches its minimum value r_0 ; thus at $z = z_F$, $r_2 = r_1 = r_F$. This condition will be discussed as ~~case 2~~ below.

For $P \geq P_{cr}$ the outer ray reaches its minimum value $r_1 = r_0$ before $r_2 = r_1$, and hence the minimum radius occurs at $z = z_0$. This will be discussed as case 1.

Case 1: $P \geq P_{cr}$

Let $z_B - z_0 = L_F$. At $r_1 = r_0$, $s = 0$ from (2-8). Since $D(0) = 0$, we get from (2-13)

$$L_F = 2K D(s_B) \quad (2-35)$$

and $r_0 = r_F$ is given by (2-25).

Case 2: $P < P_{cr}$

Let $z_B - z_F = L_F$. The minimum radius occurs where $r_1 = r_2$. Equating (2-16) and (2-34) gives

$$1 - N(\phi_B - \phi_F) = -1$$

from which

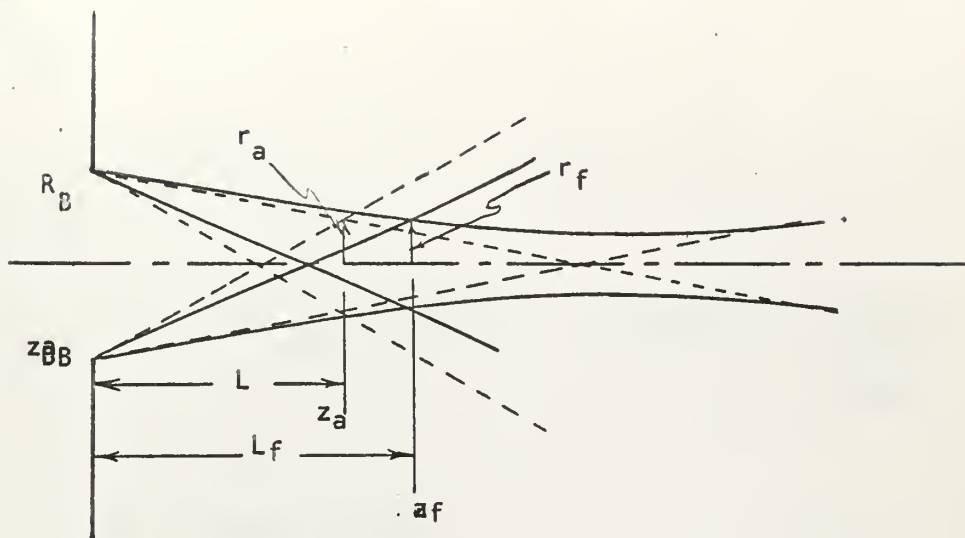
$$\phi_F = \phi_B - 2/N. \quad (2-36)$$

s_F can then be found from (2-36) and we find r_F from

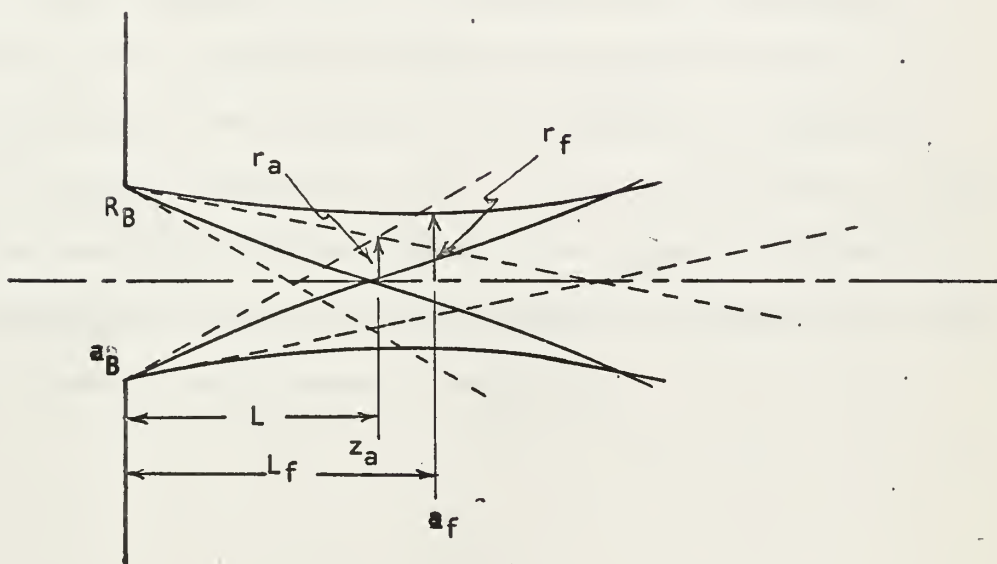
$$r_F = r_0 \exp\{s_F^2\} \quad (2-37)$$

and

$$L_F = 2K [D(s_B) - D(s_F)]. \quad (2-38)$$



(a)



(b)

Fig. 2-2

Effect of Space Charge on Beam Rays

a) $P < P_{cr}$

b) $P > P_{cr}$

When $P = P_{cr}$, L_F (case I) = L_F (case II). Note that at this point $s_F = 0$, Hence

$$N = 2/\phi_{Bcr}.$$

Putting this in (2-31) gives

$$P_{cr}^* = \frac{P_{cr} \exp \{ -2s_{Bcr}^2 \}}{(\phi_{Bcr})^2} = 9.1663 \times 10^{-7} (r_a/L)^2. \quad (2-39)$$

If

$$P^* = \frac{P \exp \{ -2s_B^2 \}}{B}$$

then this may be compared to P_{cr}^* evaluated from the second part of (2-39) and r_F and L_F may be evaluated by the methods of case I or Case II according as P^* is greater or less than P_{cr}^* . Values of L_F and r_F have been calculated for $R_B = .25$ cm, and for several values beam convergence angle (γ) and optical focal length. In Appendix 6 are presented curves of L_F and r_F as a function of perveance for $\tan \gamma$ between .01 and .15 and L between 2 and 20 cm.

APPENDIX 3

Voltage Divider Circuit for Electrode Potentials.

The requirement for three separate electrode voltages in the lens and the necessity of maintaining the electrode voltage ratios constant over a wide range of beam energies during evaluation suggested the use of a common potential source and a voltage divider network to achieve this versatility. The network utilized is as shown in Fig. 3-1.

The advantages of this circuit are:

1) V_o is measured above ground while V_g and V_a are measured with respect to V_o , so the final apertures may be grounded, V_o applied to the emitter and V_g and V_a may be expressed in terms of ratios.

2) Once V_g and V_a are adjusted to the proper values for a given V_o , V_o may be varied arbitrarily and the ratios V_a/V_o and V_g/V_a will remain fixed.

On using the circuit with the beam operating several unanticipated difficulties arose. First, the currents flowing through the lens give rise to non-ohmic virtual resistances which cause V_a/V_o and V_g/V_a to vary as V_o is varied. Further, if the cathode temperature varies with time, this causes total current to vary and thus changes the virtual inter-electrode resistances, varying V_g/V_a and V_a/V_o . Finally, the periodical resetting of the voltages was made cumbersome by the fact that the three voltages are not independent in this circuit and considerable juggling was required to obtain the proper settings.

If any extended use be made of this lens it will probably be worthwhile to redesign this circuit using voltage regulator tubes to maintain the voltages constant. For only limited use the above circuit would probably suffice, or separate sources for each potential could be used.

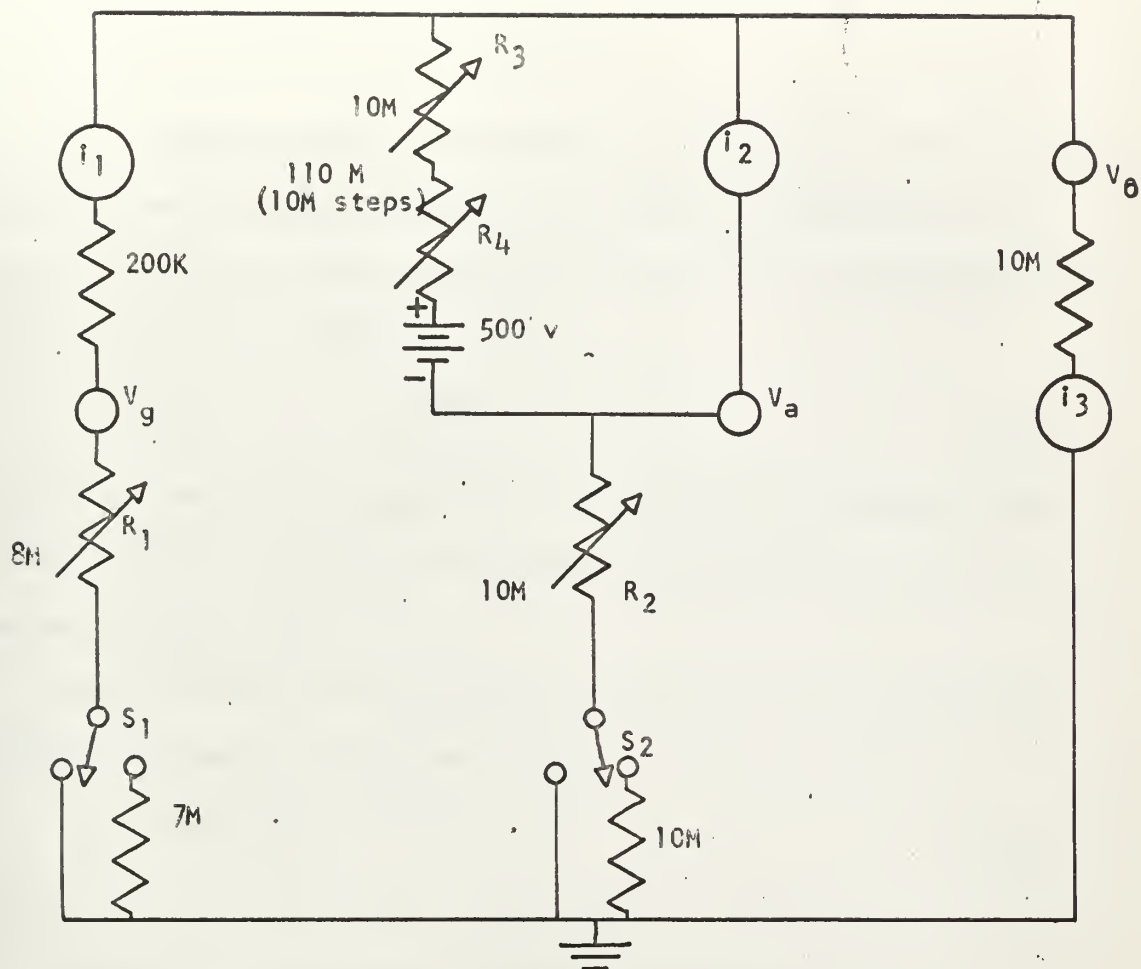


Fig 3-1

Voltage Divider Network

i_1 measures grid voltage (V_g) on a 0-25 microammeter calibrated to 0-5 volts

i_2 measures acceleration voltage (V_a) on a 0-10 microammeter calibrated to 0-500 volts

i_3 measures beam voltage (V_0) on a 0-10 microammeter calibrated to 0-100 volts

V_g is varied with R_1 and S_1

V_a is varied with R_2 and S_2

V_0 (and all other voltages in proportion) is varied with R_3 and R_4

Outputs are taken at the points indicated on the diagram.

APPENDIX 4.

Estimation of Emitter Current Densities

Let j be the average current density (in amp/cm²) of the beam at its focal point, and j_o be the current density (in amp/cm²) at the emitter. Then the maximum value of j based on thermal considerations is given by Pierce (1954) as

$$j_{\max} = j_o \left(1 + \frac{11,600}{T} V_o\right) \sin^2 \gamma \quad (4-1)$$

where T is the emitter temperature in ^oK, γ is the convergence angle of the particles arriving at the image point (Fig. 4-1a) and V_o is the beam energy in eV.

Now the maximum current density obtainable from a plane diode emitter is given by the Langmuir Child equation (for Li^+) as

$$j_o = 2.075 \times 10^{-8} V_a^{3/2} / x^2 \quad (4-2)$$

where V_a is the accelerating voltage and x is the electrode spacing.

Finally it is well known (Klemperer, 1953) that the maximum Lithium ion current that can be passed through a cylinder of radius R and length $2L$ is

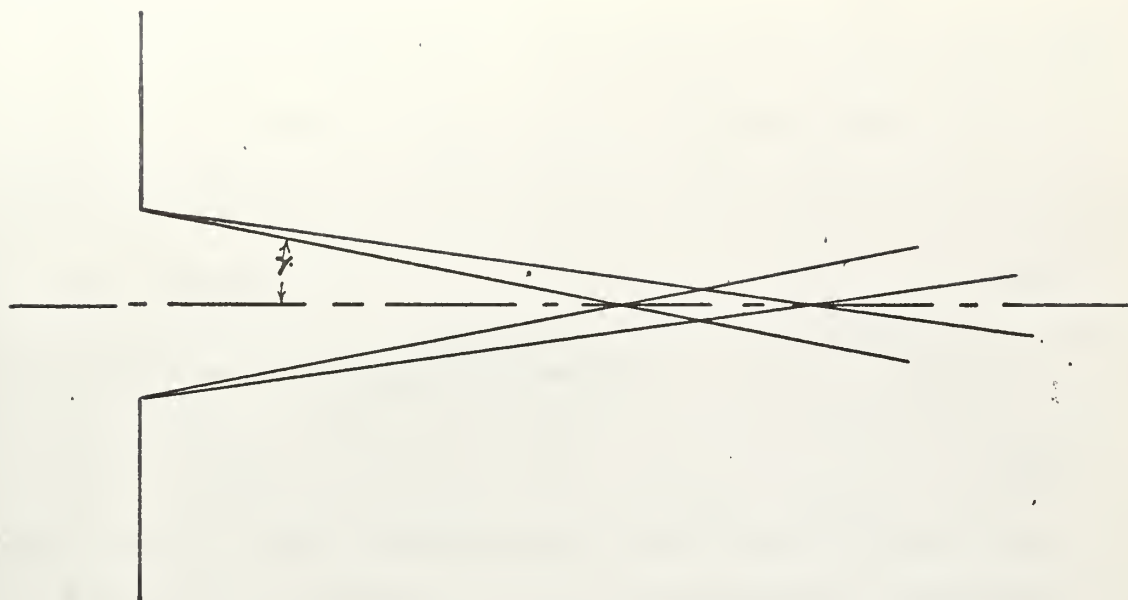
$$i = 3.42 \times 10^{-7} V_o^{3/2} (R/L)^2 \quad (4-3)$$

and this is obtained by injecting the current into the cylinder in such a manner that all the particles are initially directed at the midpoint of the cylinder axis, i.e. the maximum convergence angle of the beam is defined by

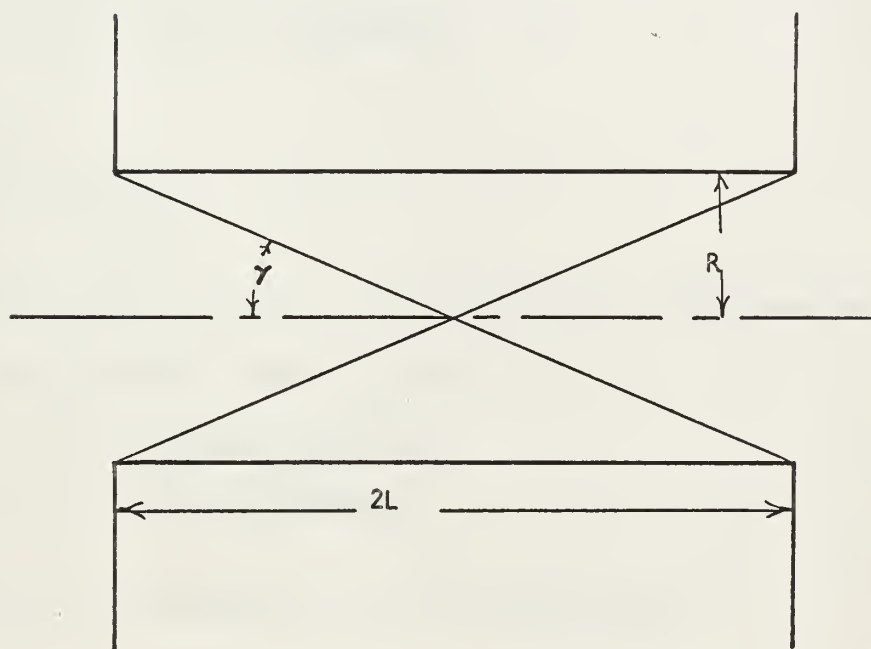
$$\tan \gamma = R/L$$

(Fig. 4-1b), whence (4-3) becomes

$$i = 3.42 \times 10^{-7} V_o^{3/2} \tan^2 \gamma \quad (4-4)$$



(a)



(b)

Fig. 4-1

Ray Patterns Defining the Angle

- (a) Finite Image Size (Equation 4-1)
- (b) Point Image (Equation 4-4)

If we define, after Pierce, the intensity efficiency of the beam as the ratio of actual current density to maximum current density as given in (4-1) then

$$E_i = j/j_{\max} \quad (4-5)$$

We also define the current efficiency by

$$E_c = M^2 j/j_o \quad (4-6)$$

where M is the overall magnification of the lens and E_c represents the fraction of the total current leaving the object in the emitter plane that finally reaches the image. Fig. 8-2 of ref. (1954) gives a relationship between E_c and E_i . We have assumed $E_c \approx .8$ and $V_o \gg 1$, whence $E_i \approx .5$.

If we put this in (4-5) and substitute (4-5) into (4-1) we get

$$j \approx .5 j_o \left(1 + \frac{11,600 V_o}{T}\right) \sin^2 \chi \quad (4-7)$$

Now

$$j = \frac{j}{\pi r_F^2}$$

and if j is given by (4-4) we substitute this in (4-7) and note that for χ small $\sin \chi \approx \tan \chi$, giving

$$j_o = \frac{2.18 \times 10^{-7} V_o^{3/2}}{r_F^2 \left(1 + \frac{11,600 V_o}{T}\right)}$$

To simplify this expression let $T \approx 1160^\circ K$ whence

$$j_o \approx \frac{2.18 \times 10^{-8} V_o^{1/2}}{r_F^2} \quad (4-8)$$

For a beam of given size and energy, (4-8) gives the required current density at the emitter. For a two stage system of the type under investigation here we may approximate the extraction stage by a plane diode and using j_o from (4-8), find the required value of V_a to get the desired beam from (4-2).

It must be borne in mind that (4-2) and (4-8) will give only rough estimates of the values necessary to get a space-charge limited beam, and that in fact, it is not possible to get the currents predicted by the formulae above, in the lens described. Plots of (4-4), (4-2) and (4-8) for various values of r_F and x are included as Figs. 6-1, 6-2 and 6-3 respectively in Appendix 6 where they may be used as an aid in predicting lens performance.

APPENDIX 5

Analysis of Beam Profile Data

Consider the following experimental arrangement, illustrated in Fig. 5-1:

A slit of width Δy is moved past a beam (slit motion is in the y direction) whose radial current density in any cross-section is an axially symmetric function of distance from the beam center, say $j(r)$. Then the current passing through the slit at any distance, y , from the beam axis is

$$i(y) = 2\Delta y \int_0^{\infty} j(x, y) dx \quad (5-1)$$

where we assume that the variation of j over Δy is negligible. The total current in the beam is

$$i_t = \int_0^{\infty} j(r) da = 2\pi \int_0^{\infty} j(r) r dr \quad (5-2)$$

and the current included within any radius R is

$$i(R) = 2\pi \int_0^R j(r) r dr \quad (5-3)$$

Now let us assume that

$$j(r) = A \exp \left\{ -r^2/\alpha^2 \right\} = A \exp \left\{ -(x^2 + y^2)/\alpha^2 \right\} \quad (5-4)$$

where A and α are constants for any given cross-section, but in general may vary with z (axial distance) subject to the restriction that i_t is independent of z . Let us also take as the nominal beam radius the point $r = R$, where

$$\frac{i(R)}{i_t} = 1 - \frac{1}{e} \quad (5-5)$$

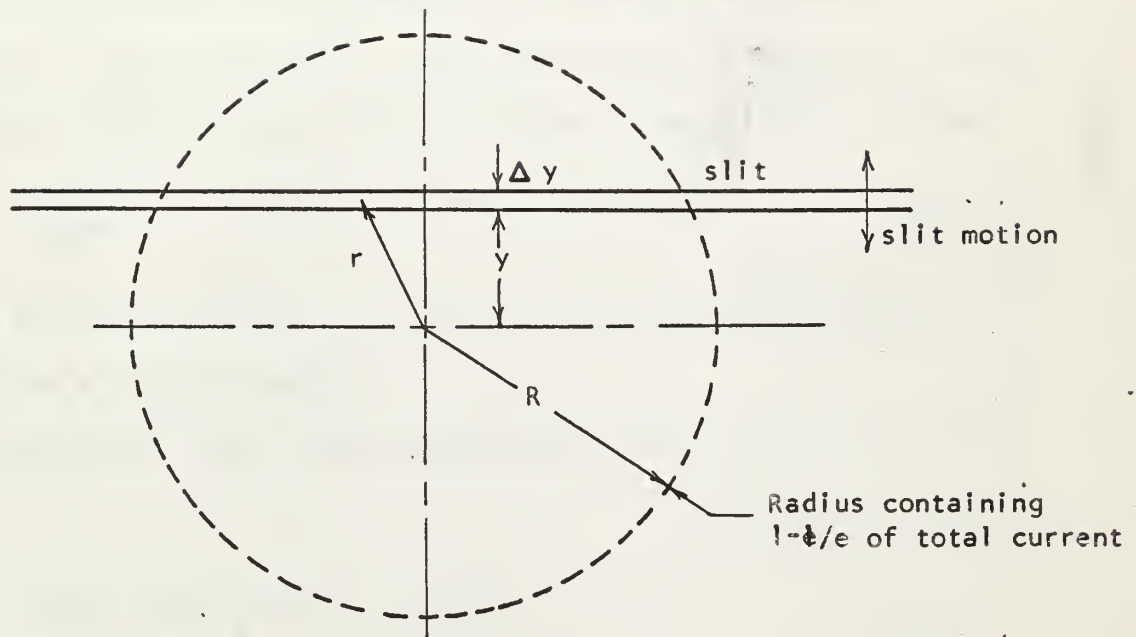


Fig 5-1

Slit Geometry for Beam Profile Analysis

Using (5-4), (5-1) becomes

$$\begin{aligned}\Delta i(y) &= 2A \Delta y \exp \left\{ -y^2/\alpha^2 \right\} \int_0^{\infty} \exp \left\{ -x^2/\alpha^2 \right\} dx \\ &= \sqrt{\pi} A \alpha \Delta y \exp \left\{ -y^2/\alpha^2 \right\}\end{aligned}\quad (5-6)$$

Since we have assumed axial symmetry in the beam we may take the direction of r to be along the y axis without loss of generality. Doing this we see immediately that $\Delta i(y)$ is proportional to $j(r)$, and that

$$\frac{\Delta i(y)}{\Delta i_{\max}} = \frac{j(r)}{j(0)} = \exp \left\{ -y^2/\alpha^2 \right\} \quad (5-7)$$

Hence a measurement of $\Delta i(y)$ is equivalent to a measurement of $j(r)$ (except for a constant factor).

Putting (5-4) into (5-3) and making the change of variable $r^2 = w$, we get

$$\begin{aligned}i(R) &= \pi A \int_0^{R^2} \exp \left\{ -w/\alpha^2 \right\} dw \\ &= \pi A \alpha^2 (1 - \exp \left\{ -R^2/\alpha^2 \right\})\end{aligned}\quad (5-8)$$

The total current is obtained as R goes to infinity, thus

$$i_t = \pi A \alpha^2 \quad (5-9)$$

Hence

$$\frac{i(R)}{i_t} = 1 - \exp \left\{ -R^2/\alpha^2 \right\}$$

which satisfies the criterion of (5-5) at $R = \alpha$ whence (5-7) becomes

$$\frac{\Delta i(R)}{\Delta i_{\max}} = \frac{1}{e} \quad (5-10)$$

Hence, if the assumption of (5-4) is valid, the nominal beam radius may be determined by plotting Δi against y and noting the value of y at which (5-10) is satisfied. Furthermore such a plot will be a measure of the radial current density distribution, according to (5-7).

To test this assumption the beam profile was analyzed in detail for two representative beams, one of 80 eV and one of 10 eV. Cross sections of each are shown as part of Figs. 5-2 through 5-7, for a point in the convergent section of the beam, one near the focal point where the beam is essentially parallel, and one in the divergent section of the beam. The distances are from the final defining aperture of the lens, and the values of Δi have been normalized to 1. The slit width Δy was .23 mm and Δi is the (normalized) current passing the slit at a distance y from the center of the beam. The total currents were 1.3×10^{-8} amp at 80 eV and 3.8×10^{-9} amp at 10 eV.

If we divide (5-6) by (5-9) we get

$$\frac{\Delta i(y)}{i_t} = \frac{\Delta y}{\sqrt{\pi} \alpha} \exp \left\{ -y^2 / \alpha^2 \right\}$$

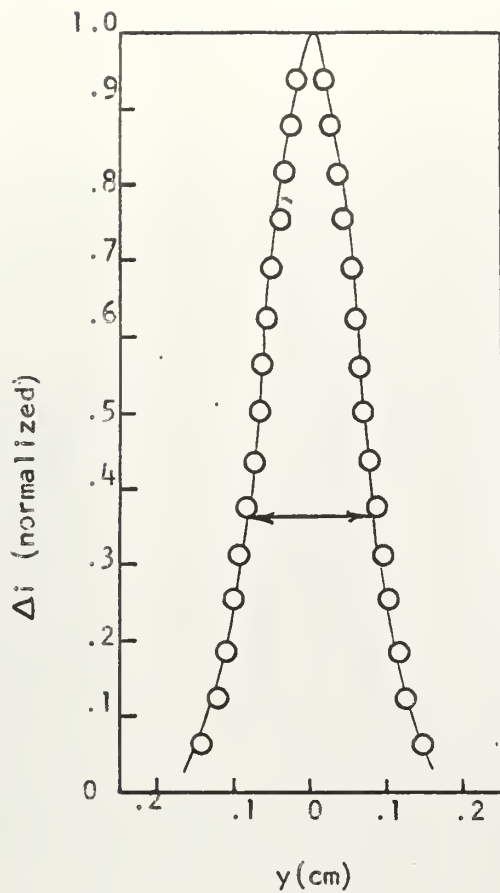
Taking logs of both sides

$$\log \left\{ \Delta i(y) / i_t \right\} = \log \left(\Delta y / \alpha \sqrt{\pi} \right) - \frac{y^2}{\alpha^2} \log(e) \quad (5-11)$$

Equation (5-11) is plotted in Figs. 5-2 through 5-7 for each cross section analyzed and for the values of α indicated, after normalizing $\log \left\{ \Delta i(y) / i_t \right\}$ to 1. The dotted lines indicate the deviation from this assumption of the actual current through the slit. Clearly, the assumption is best for high energies and close to the lens and less good elsewhere. The useful region of the beam is mainly from the lens to just beyond the focal point. The assumption of a Gaussian current

density distribution gives a reasonable estimate of the beam size in this region. Marked deviations of the measured Δ farther from the lens indicate that the above analysis is invalid outside the useful portion of the beam.

Fig. 5-2 through 5-7
Check of Gaussian Assumption



(a)

Beam "diameter"

.16 cm.

Fig. 5-2

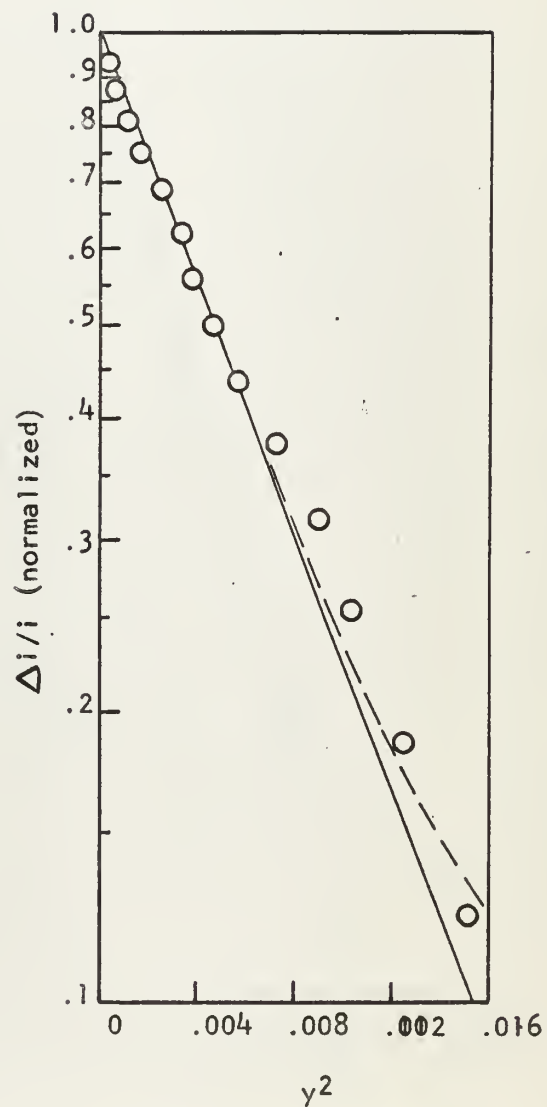
80 eV, $z - z_B = 1.37$ cm

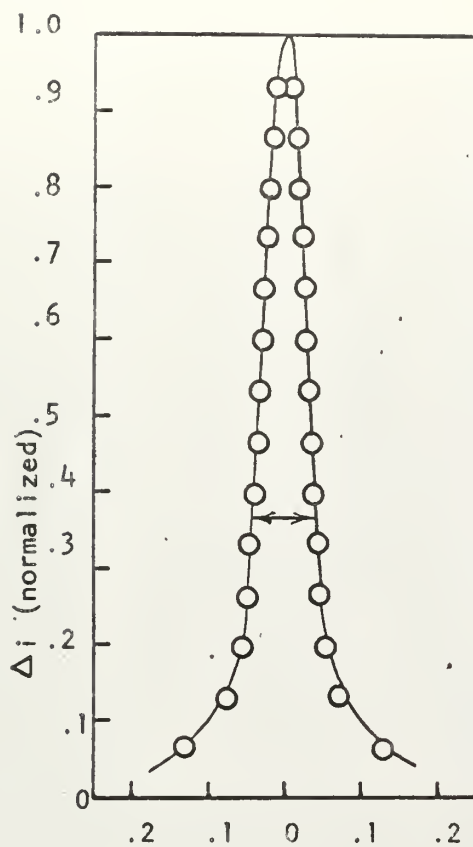
Convergent

Beam

(b)

$\alpha = .0815$





y (cm)

(a)

Beam "Diameter"

.08 cm

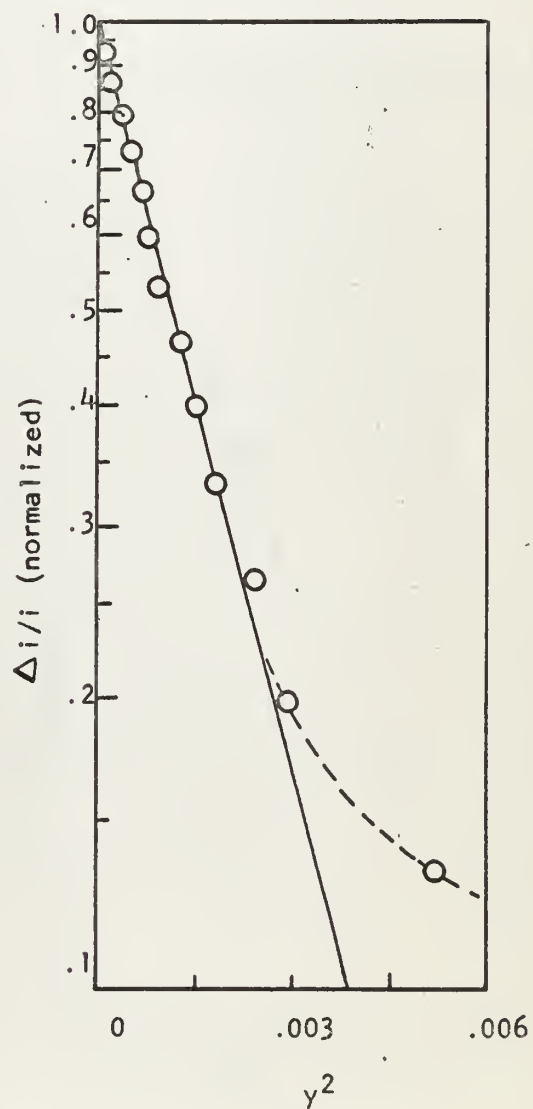
Fig. 5-3

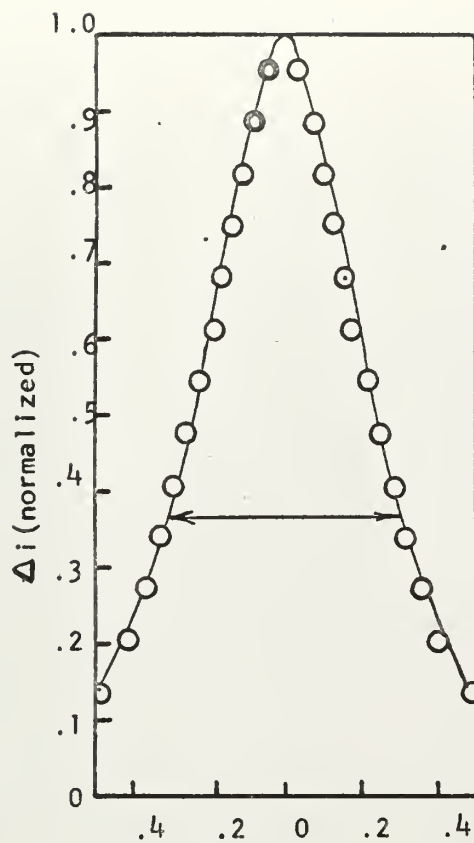
80 eV, $z-z_B = 2.43$ cm

Focal Point of Beam

(b)

$$\alpha = .0409$$





y (cm)

(a)

Beam "Diameter"

.6 cm

(b)

$\alpha = .265$

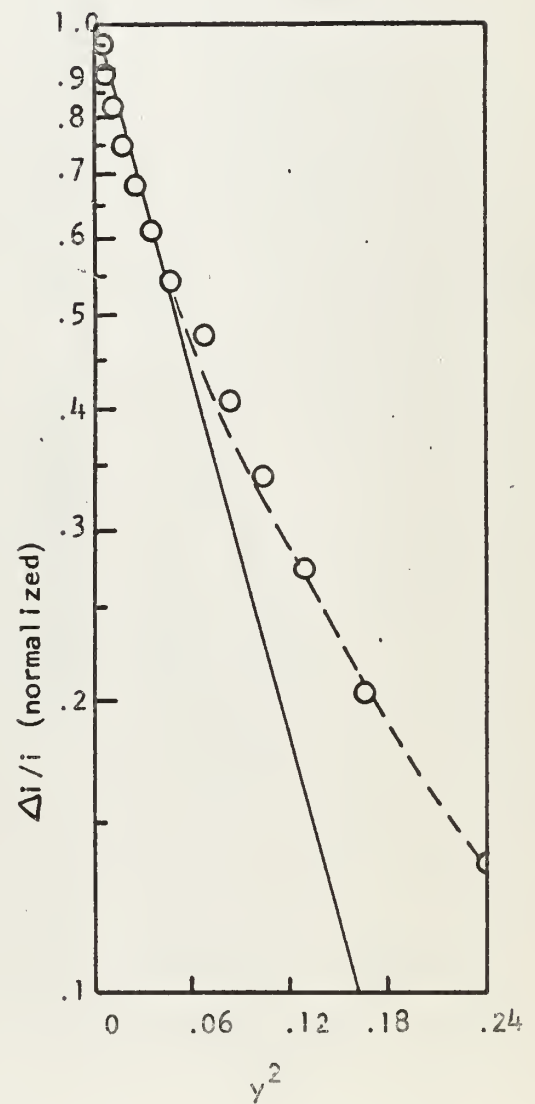
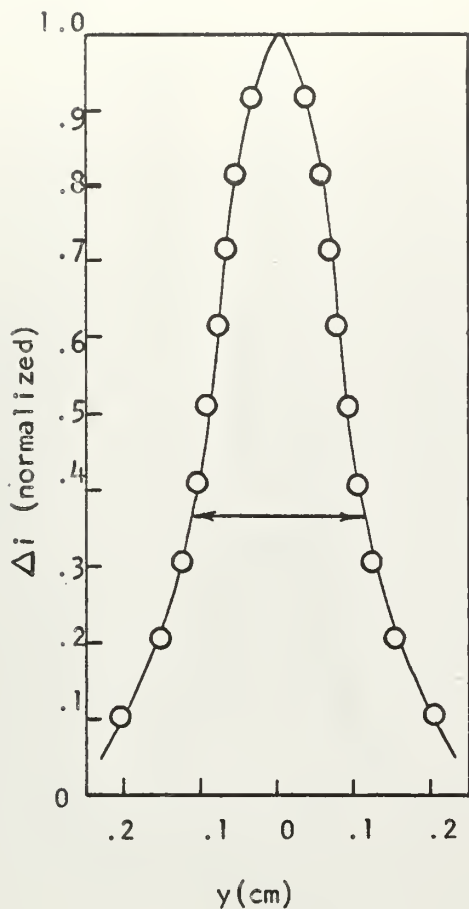


Fig. 5-4

80 eV, $z - z_B = 6.85$ cm.

Divergent Beam



(a)

Beam "Diameter"

.22 cm

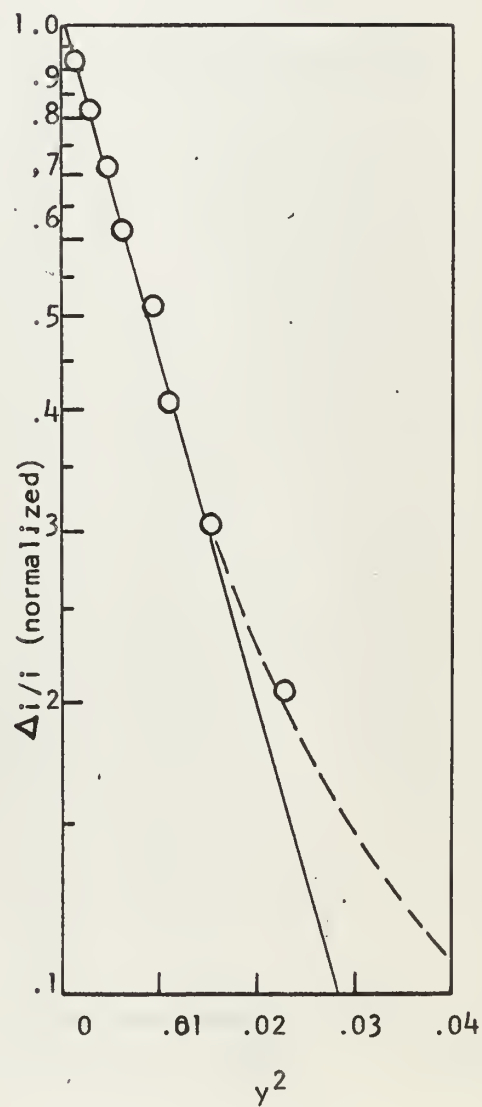
Fig. 5-5

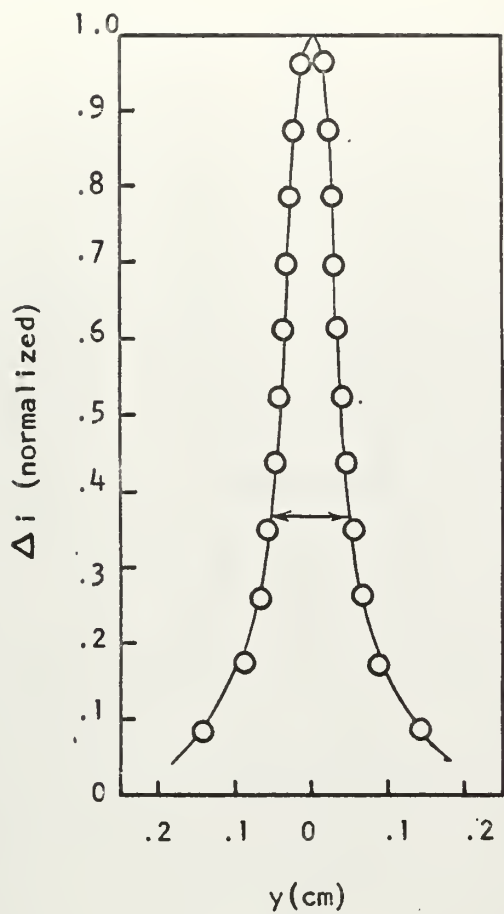
10eV, $z - z_B \approx 1.36$ cm

Convergent Beam

(b)

$\alpha = .1103$





(a)

Beam "Diameter"

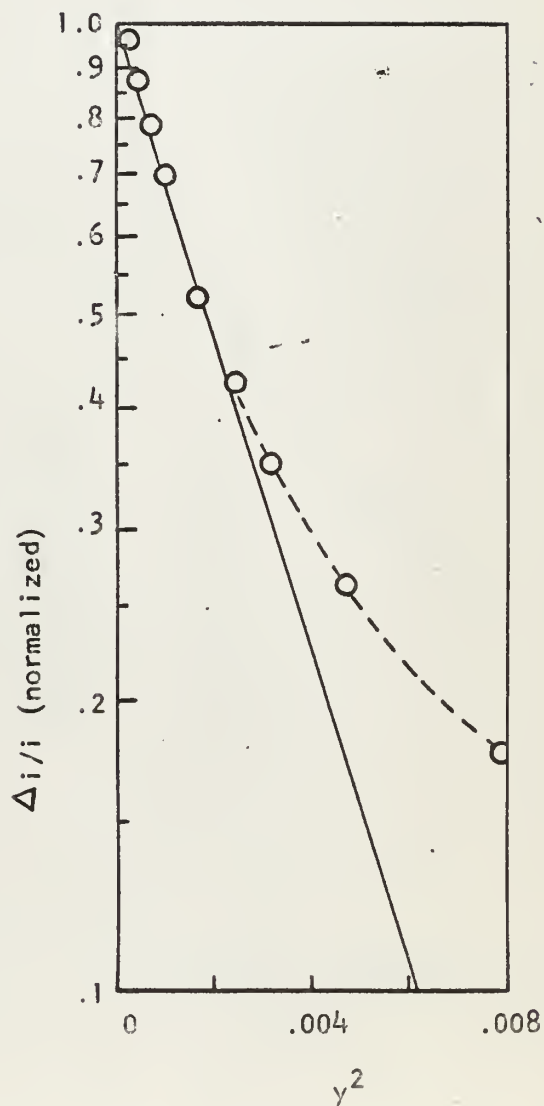
.1 cm

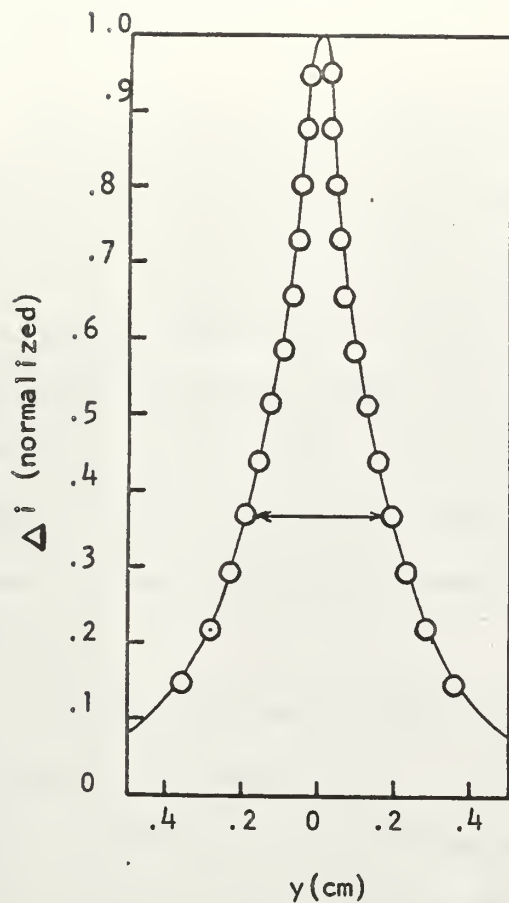
Fig. 5-6

10 eV, $z - z_B = 2.09$ cm

Focal Point of Beam

(b)
 $\alpha = .0519$





(a)

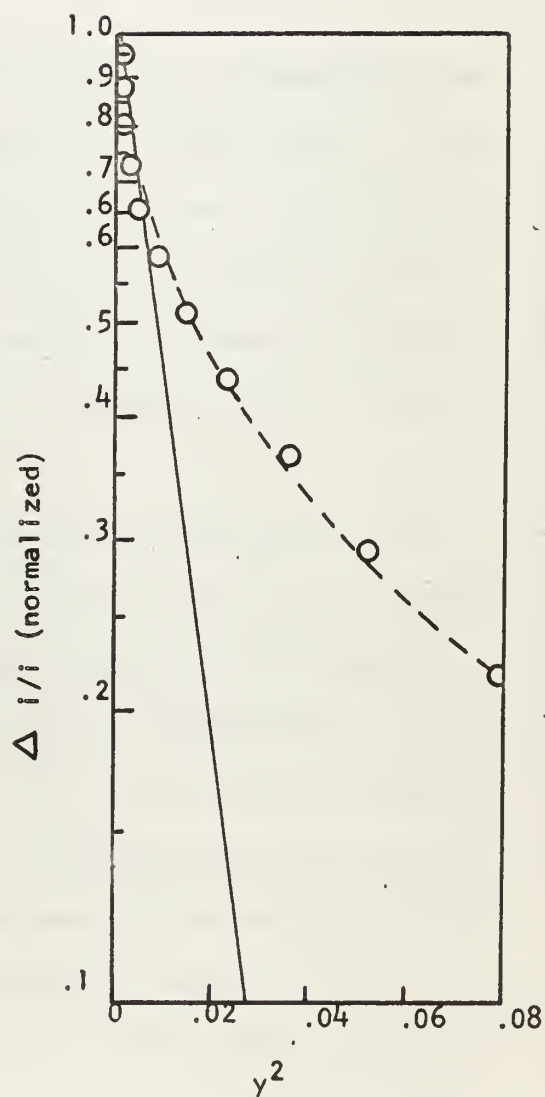
Beam "Diameter"
.38 cm

Fig. 5-7

10 eV, $z-z_B = 4.40$ cm

Divergent Beam

(b)
 $\alpha = .1103$



Design Curves

The curves collected here are sufficient for the prediction of lens performance based on the theory of electron optics and the mass of Li^7 . The use of the curves is best illustrated by an example.

Let us assume that we require a beam of Lithium ions of 20 eV energy whose minimum radius is 1.5 mm and is 8 cm from a lens whose opening is .25 cm radius. To insure good collimation we also require $\tan\gamma$ be $\sim .05$. From Figs. 6-9 (a) and 6-9 (b) we see that these conditions may be met with a beam whose perveance is $\sim 10^{-11}$ with $L = 8$ cm.

From Fig. 6-3 we see that the above specifications demand that the emitter current density be $\sim 4 \times 10^{-6}$ amp/cm². For the extraction stage used the emitter to extraction anode distance is ~ 2 cm, so to estimate the available current densities we assume this to be a diode of 2 cm spacing and from Fig. 6-2 we find that an extraction potential of 100v should give ample current density, and a 5:1 step down ratio for the deceleration stage is chosen.

The location of aperture 2 is 1 cm beyond the low voltage plate of the deceleration stage. Since the low voltage plate is the reference plane for this stage we must have the image distance 9 cm to enter Fig. 6-4. This gives an object distance of 5.5 cm and a magnification $M \sim 3$.

From Fig. 6-1 the maximum possible current at 20 eV and $\gamma = .05$ is $\sim 10^{-7}$ amp. For the emitter used in this experiment we reduce this by a factor of 30 as a practical matter (Note that improved emitter design will probably enable this factor to be reduced considerably or even eliminated), leaving an expected current of $\sim 3 \times 10^{-9}$ amp. This sets

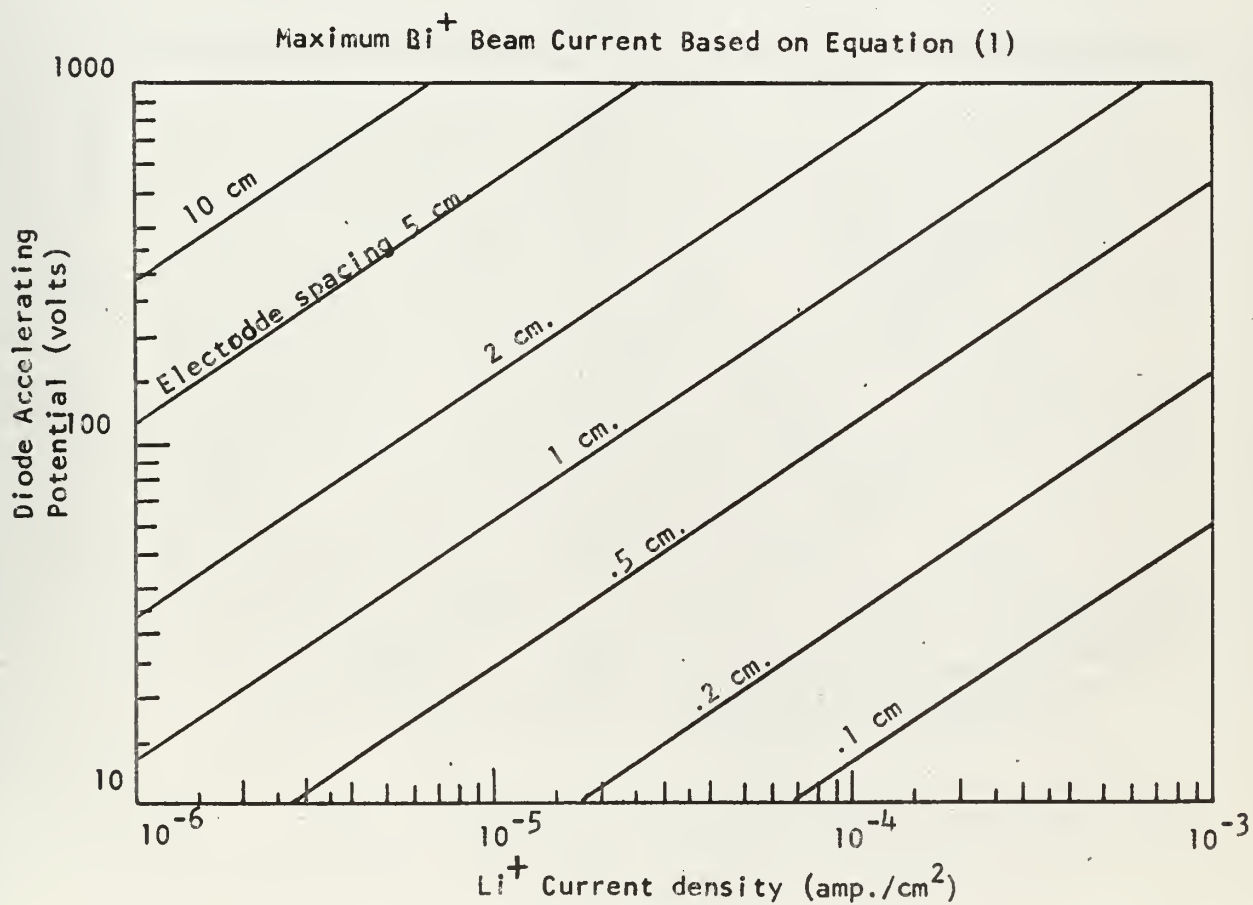
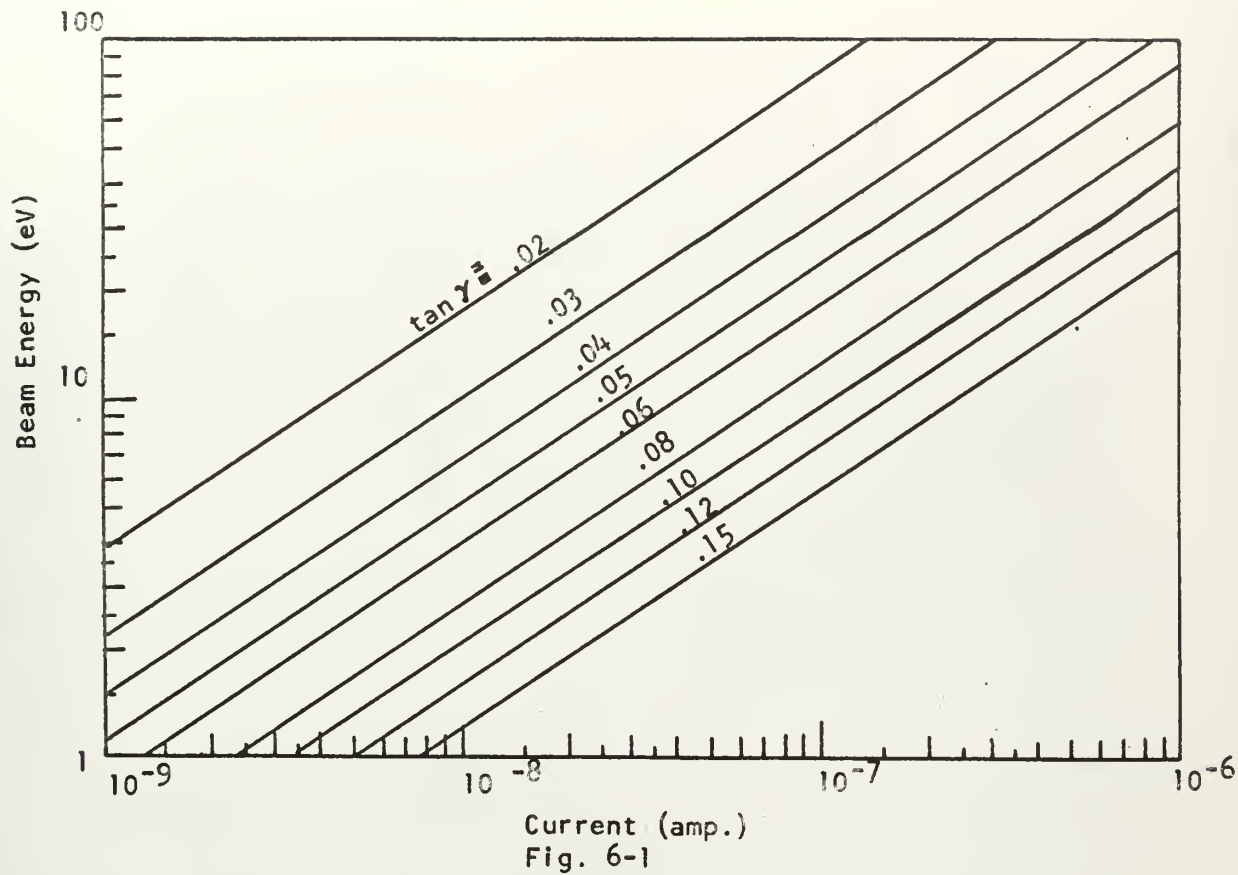
the predicted beam perveance at $\sim 3 \times 10^{-11}$ which, for the chosen beam parameters does not drastically alter the desired beam characteristics.

Next we calculate P_e from equation (3) (in the main text), for a 5:1 step-down ratio, giving $P_e \sim 3 \times 10^{-12}$. With this value we enter Fig. 6-5 and find the grid bias needed to give the required extraction perveance to be $\sim 1.25\%$, from which we find $M \sim .5$ and $Q/d_k \sim 5.7$. d_k is the emitter to grid distance, in this case 1.8mm, so we find the extraction stage image distance Q , to be ~ 1.0 cm. The 5.5 cm object distance for the deceleration stage then requires that the two stages be set 6.5 cm apart (using the upstream side of the grid plate as a reference plane for the extraction stage, and the low voltage plate for the deceleration stage). Simpson and Kuyatt (1963c) state that the effective emission area radius for the extraction stage used is approximately half the radius of the grid aperture, hence the "object size" for the extraction stage is 1 mm in radius for the dimensions used. Combining the magnifications of the two stages gives a value of $r_a \sim 1.5$ mm as required by Fig. 6- 9 (b).

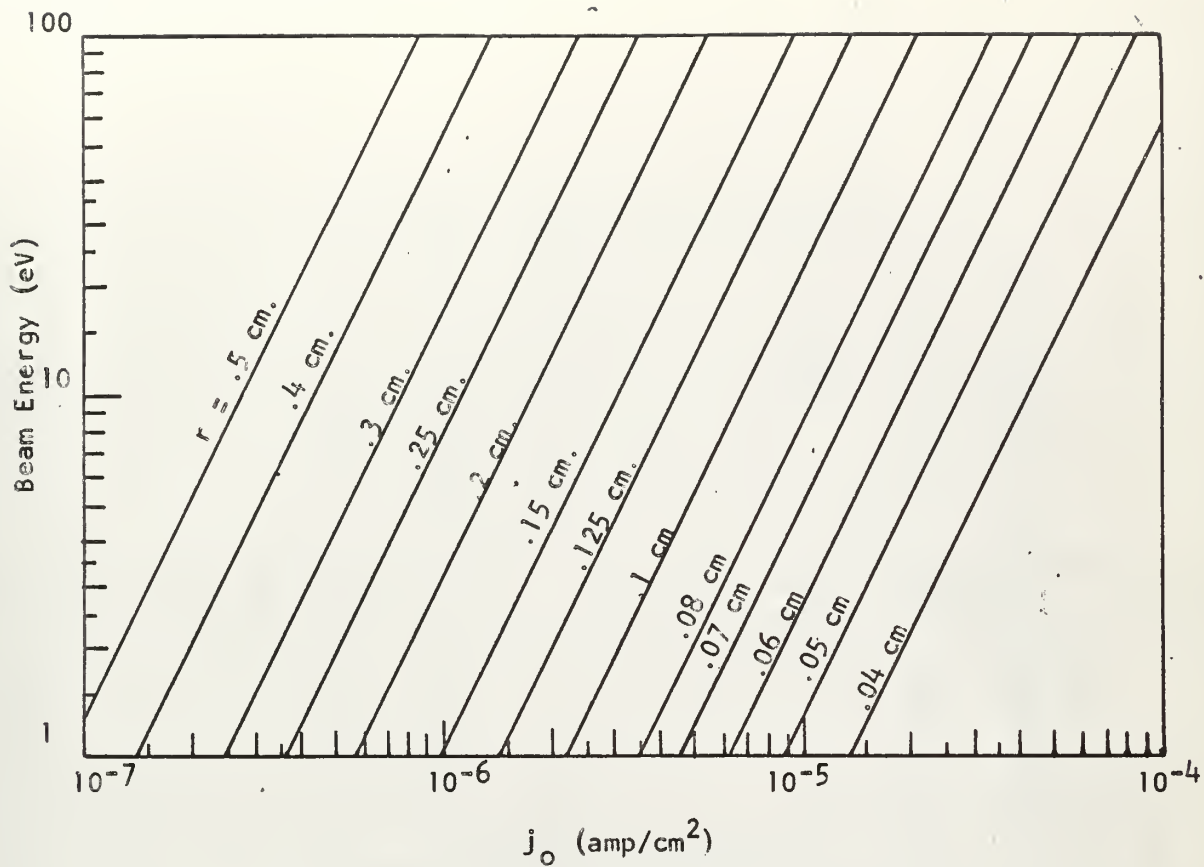
To summarize, we have found a solution to the problem which gives a beam of .3 cm minimum radius 8 cm from the lens, for a step-down ratio of 5:1, a grid bias of 1.25%, and an inter-stage spacing of 6.5 cm. For such a configuration we expect a current of 3×10^{-9} amp. We also note that at these voltages the inter-stage space charge spreading would tend to make L_F slightly larger than predicted.

Clearly there are so many independent parameters to this system that there is wide freedom of choice in setting the lens to obtain any desired beam configuration, and different sorts of requirements

placed on the final beam desired will require a different approach to the design problem. Furthermore, secondary adjustment of some of the lens parameters may be necessary to improve the beam characteristics after the initial settings. Facility in the use of these curves and understanding of their versatility will be gained through experience.



Langmuir-Child Law for Various Diode Spacings



j_o (amp/cm²)

Fig. 6-3

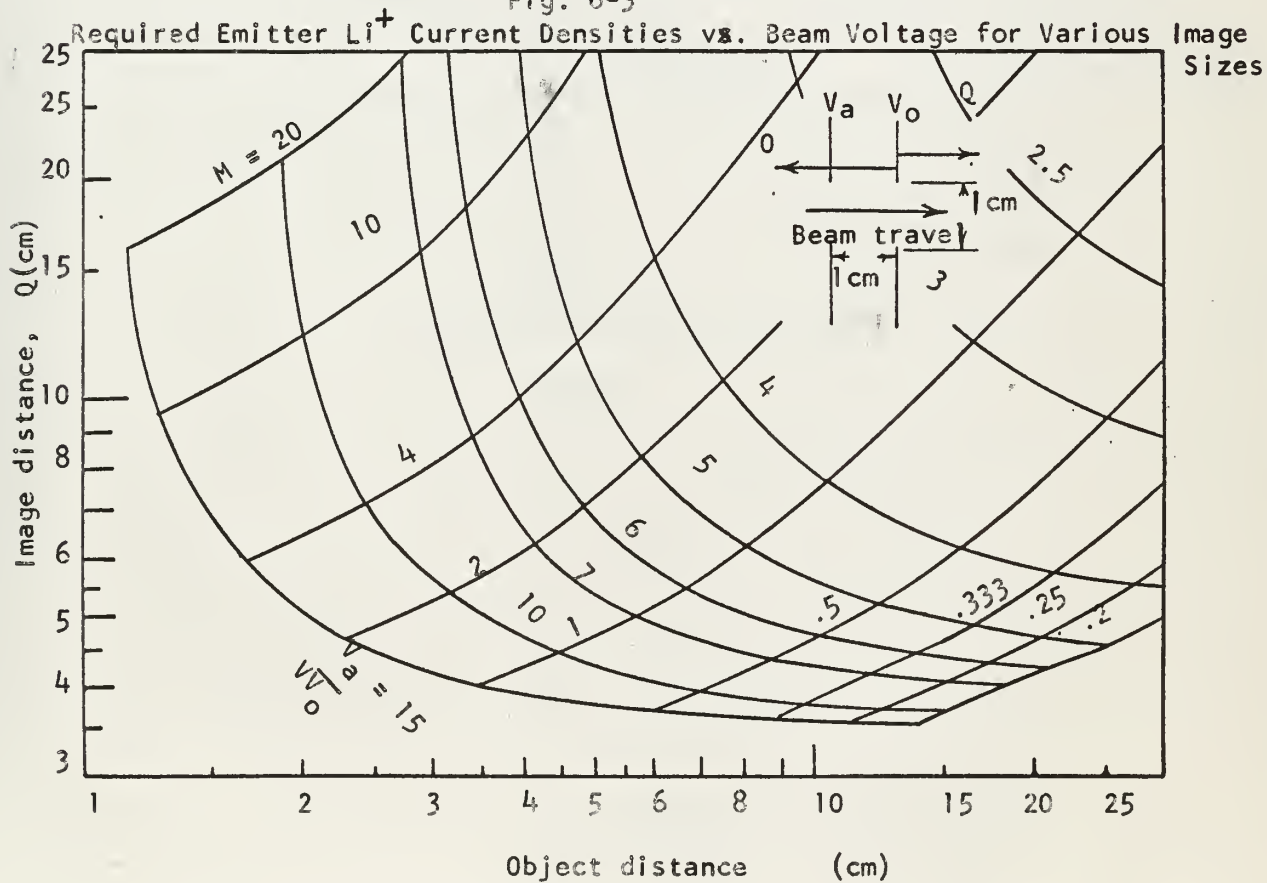


Fig. 6-4

Optical Characteristics of the Deceleration Stage

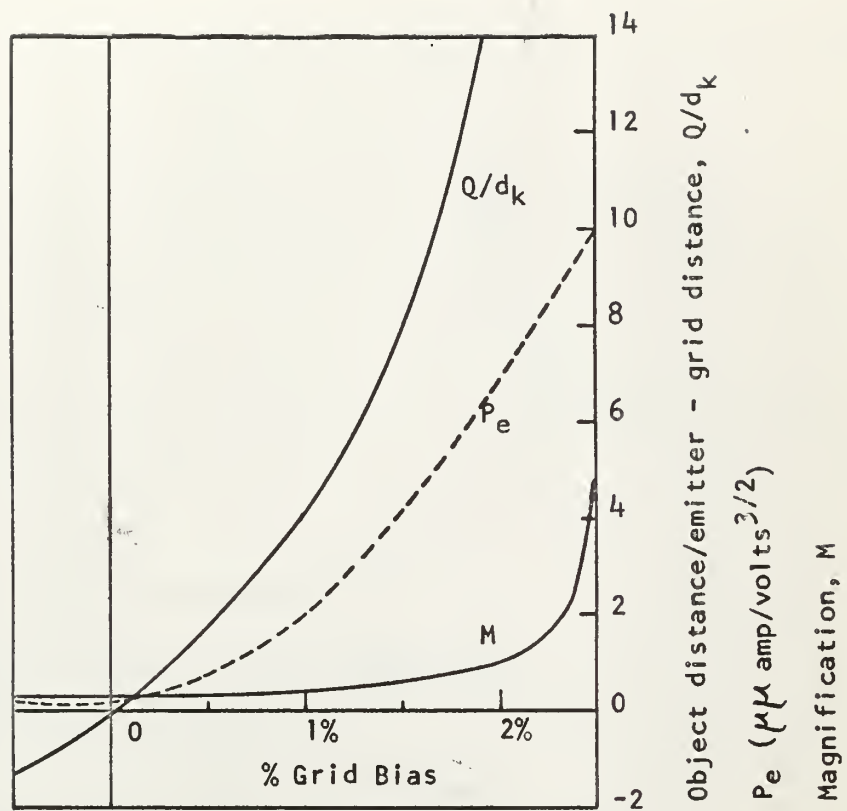
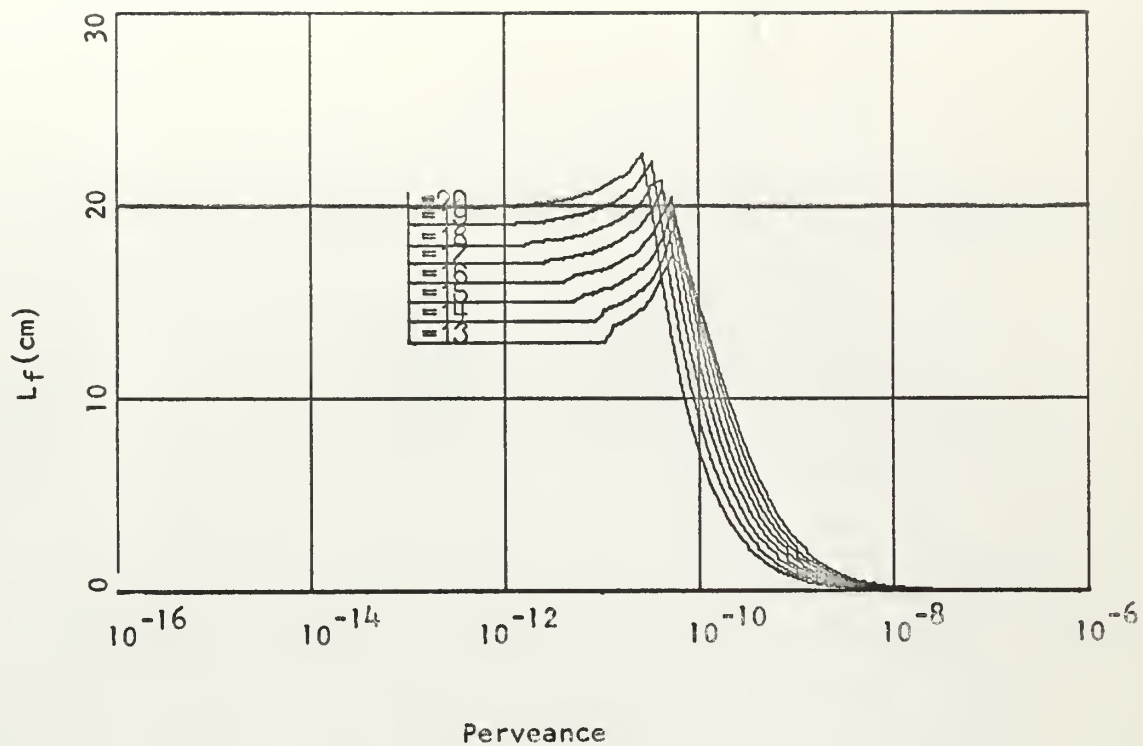


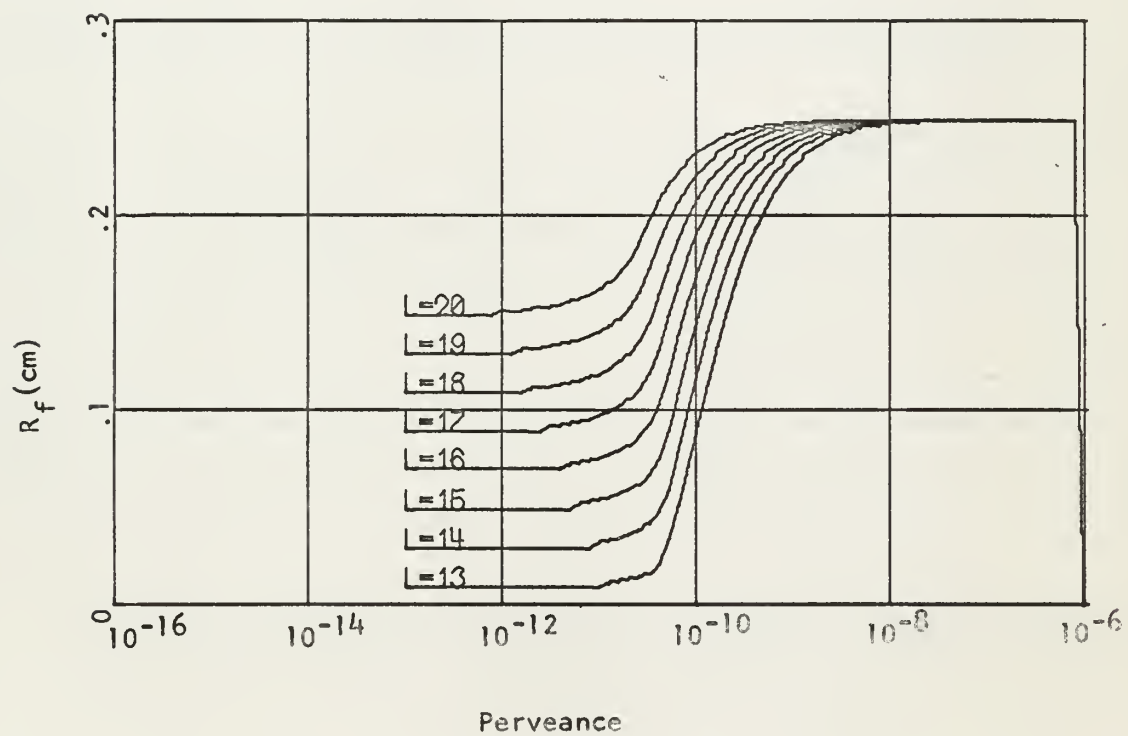
Fig. 6-5
Characteristics of Extraction
Stage

Fig. 6-6 through 6-18

- a) Plots of Radius of Space Charge Focal Point as a Function of Beam Perveance for Indicated Conditions**
- b) Plots of Space Charge Focal Distance as a Function of Beam Perveance for Indicated Conditions**



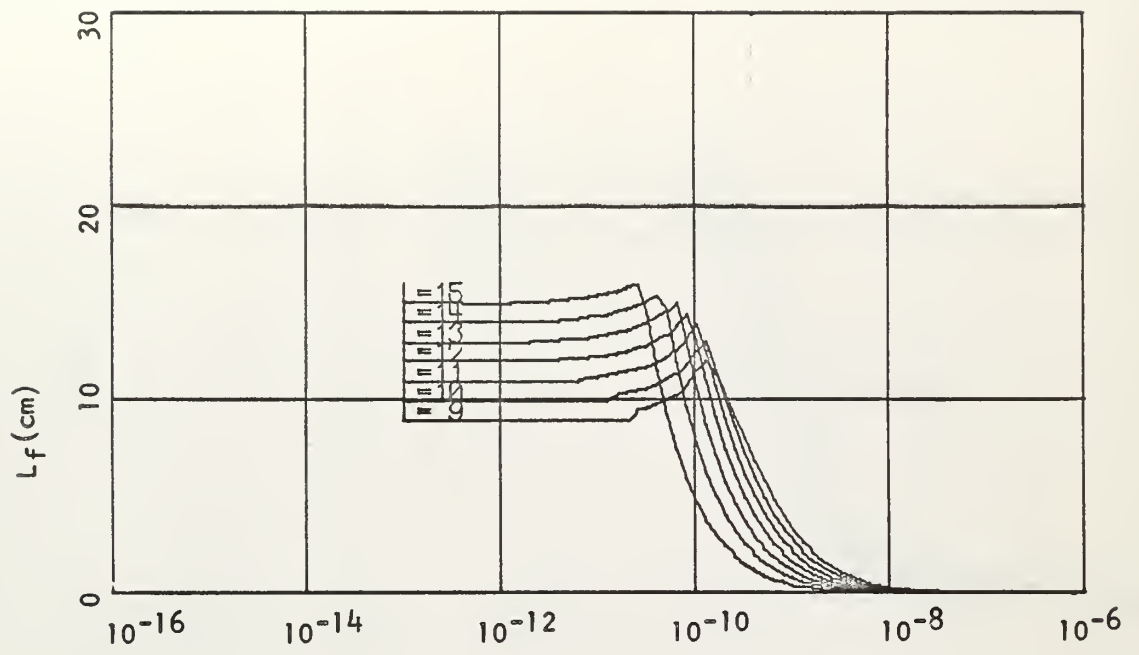
(a)



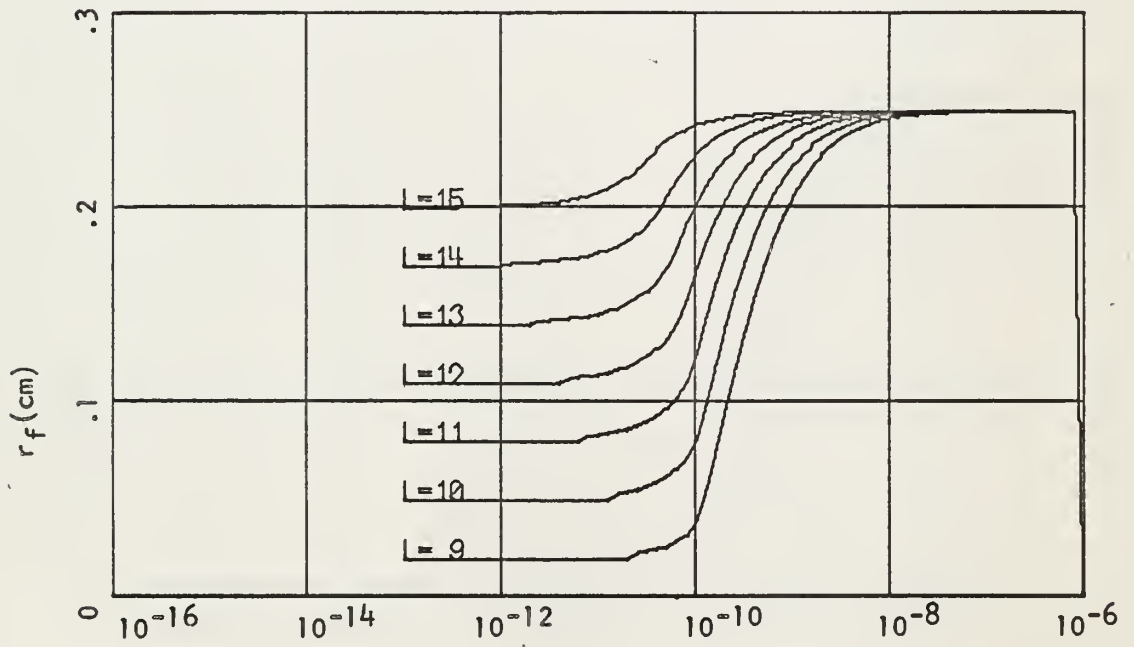
(b)

Fig. 6-6

$$\tan \gamma = .02 \quad R_B = .25 \text{ cm}$$



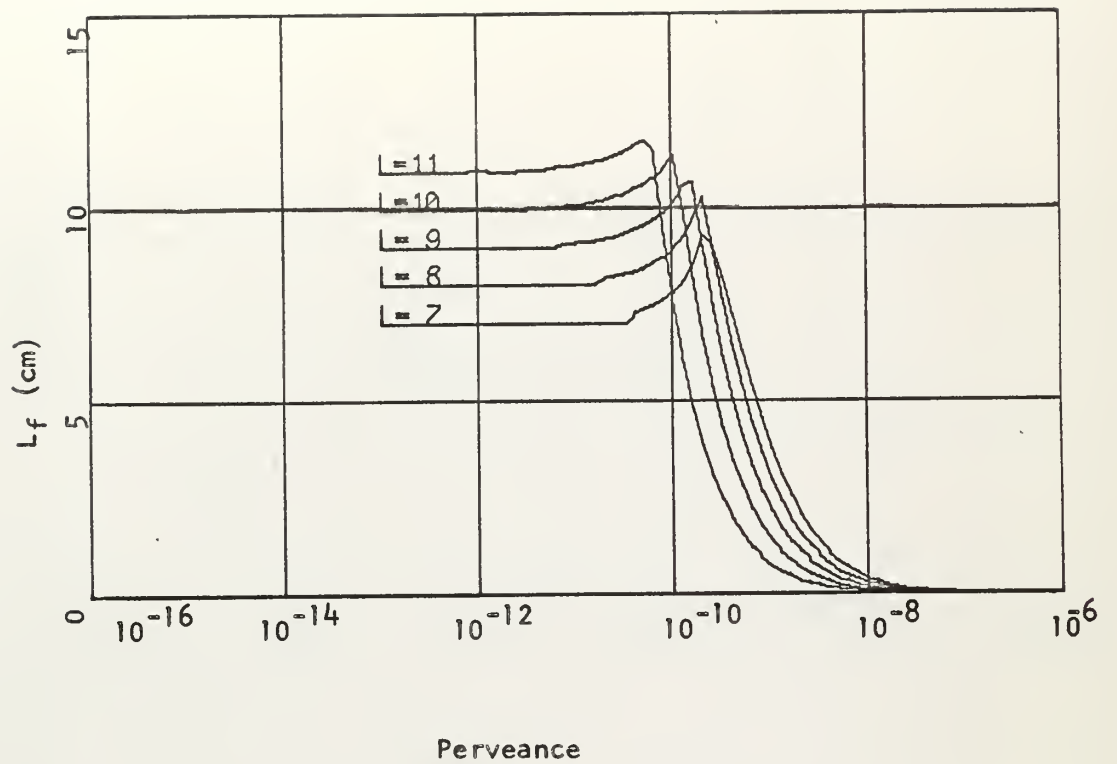
Perveance
(a)



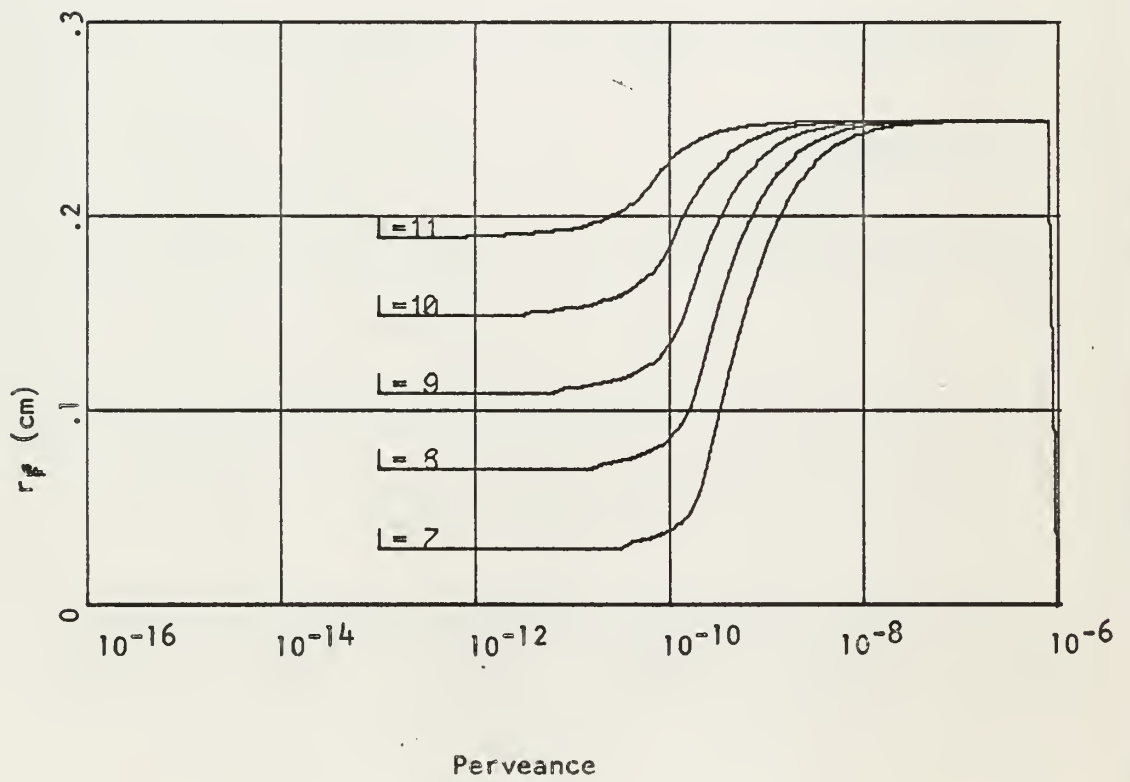
Perveance
(b)

Fig. 6-7

$$\tan \gamma = .03 \quad R_B = .25 \text{ cm}$$



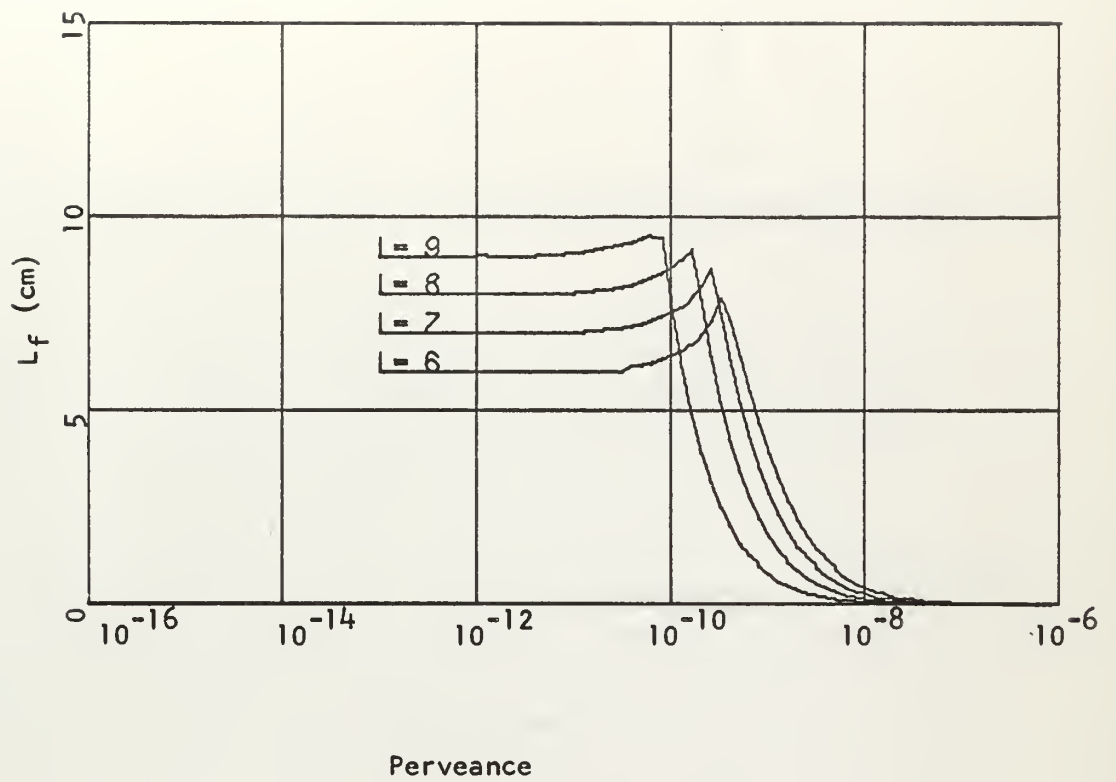
(a)



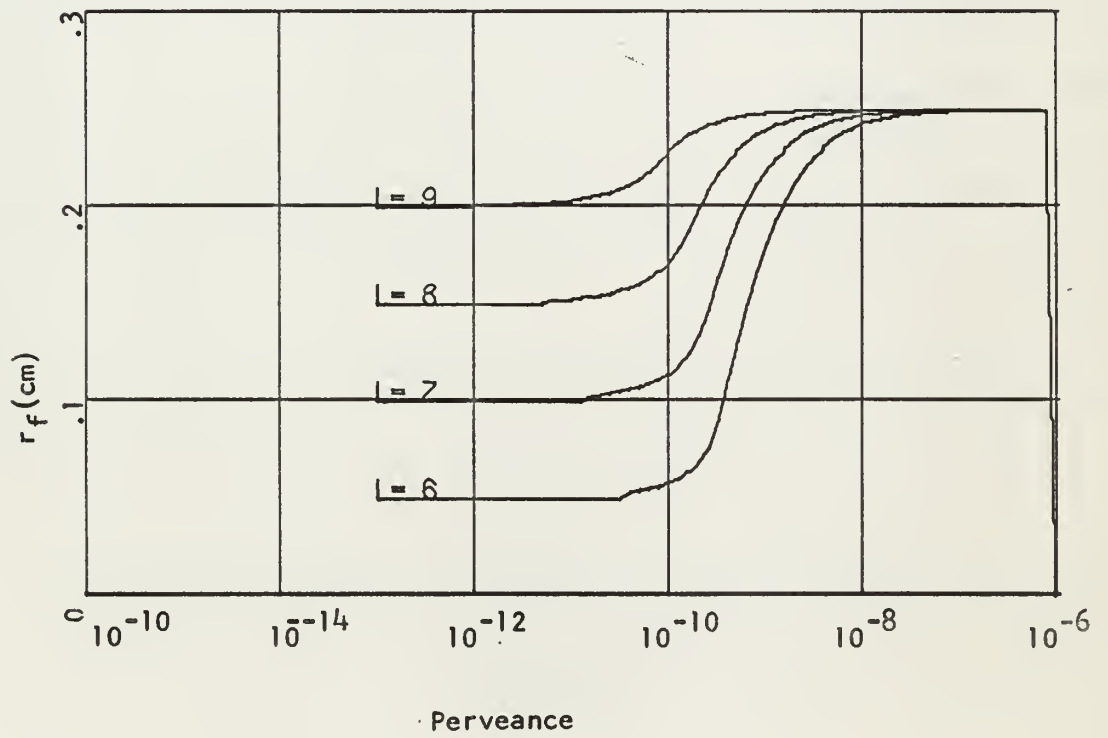
(b)

Fig. 6-8

$$\tan \gamma = .04 \quad R_B = .25 \text{ cm}$$



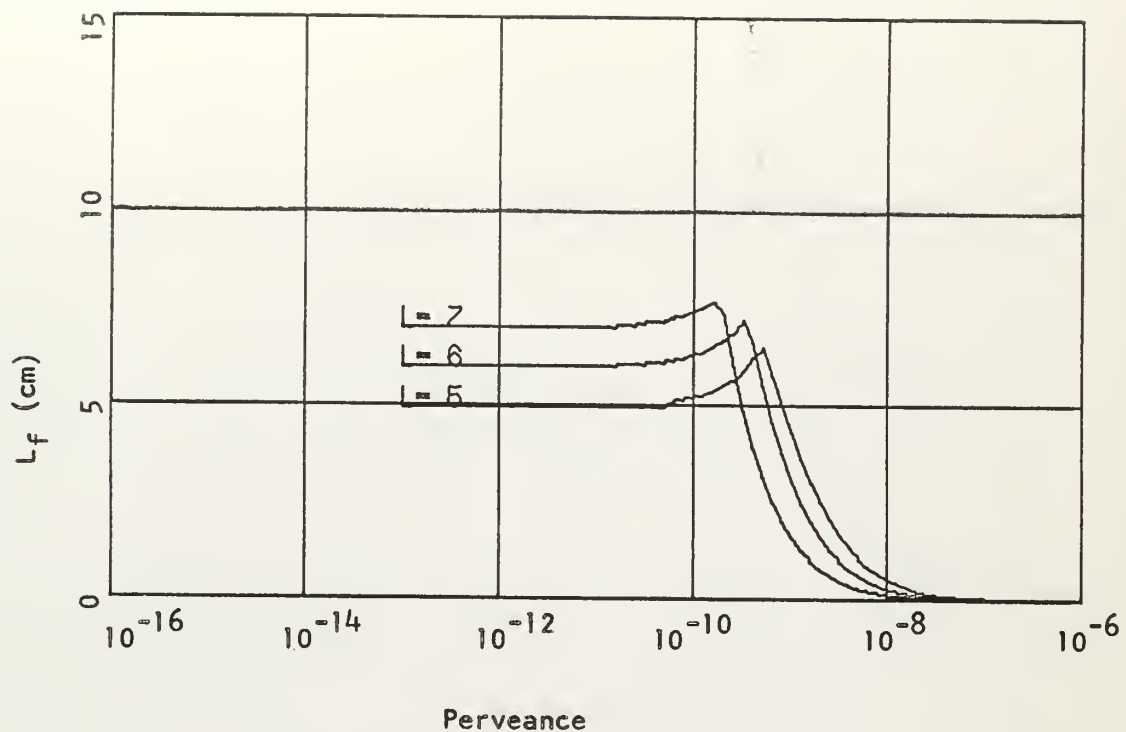
(a)



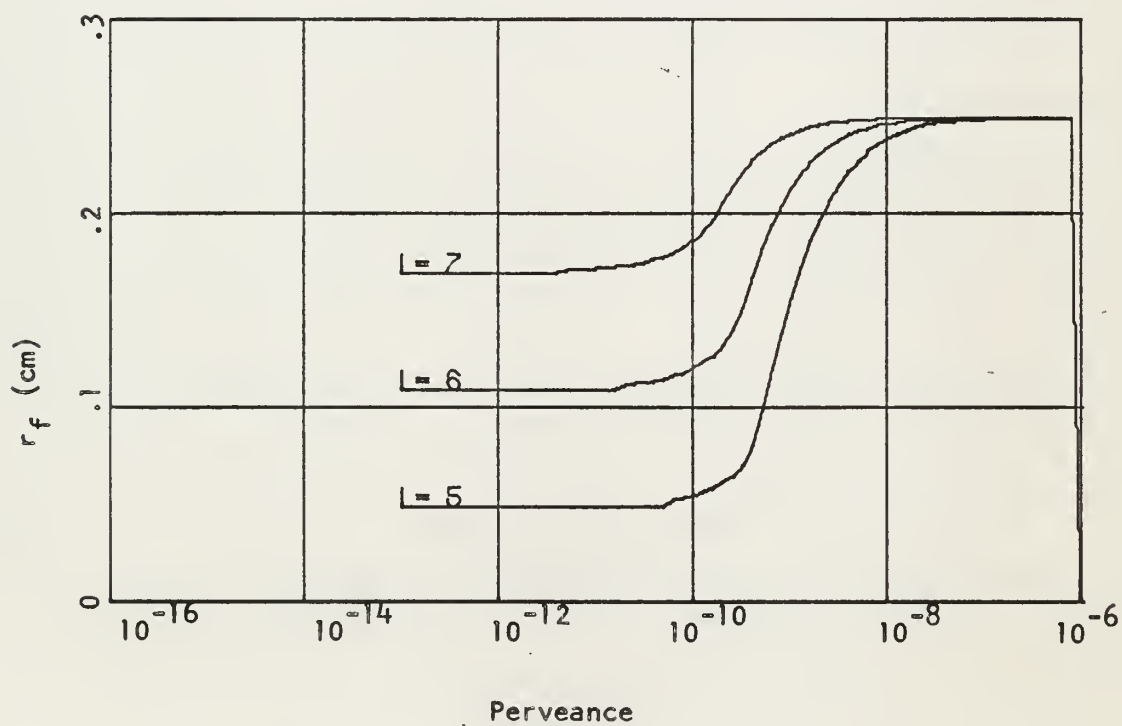
(b)

Fig. 6-9

$$\tan \gamma = .05 \quad R_B = .25$$



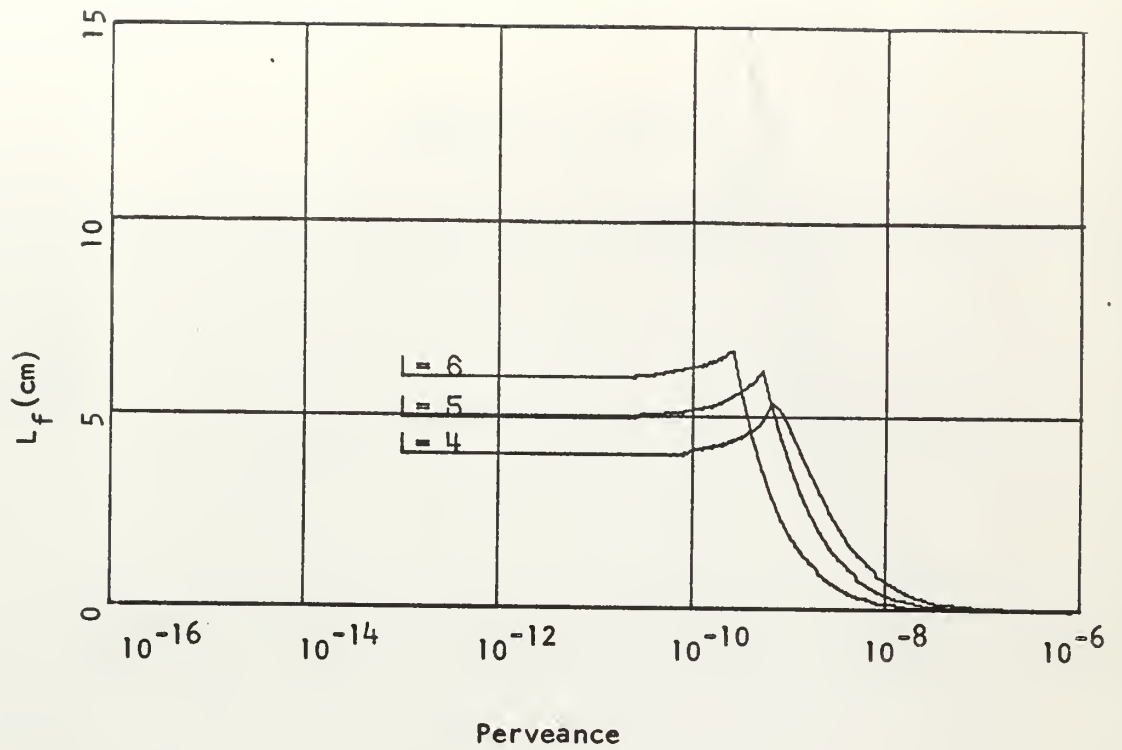
(a)



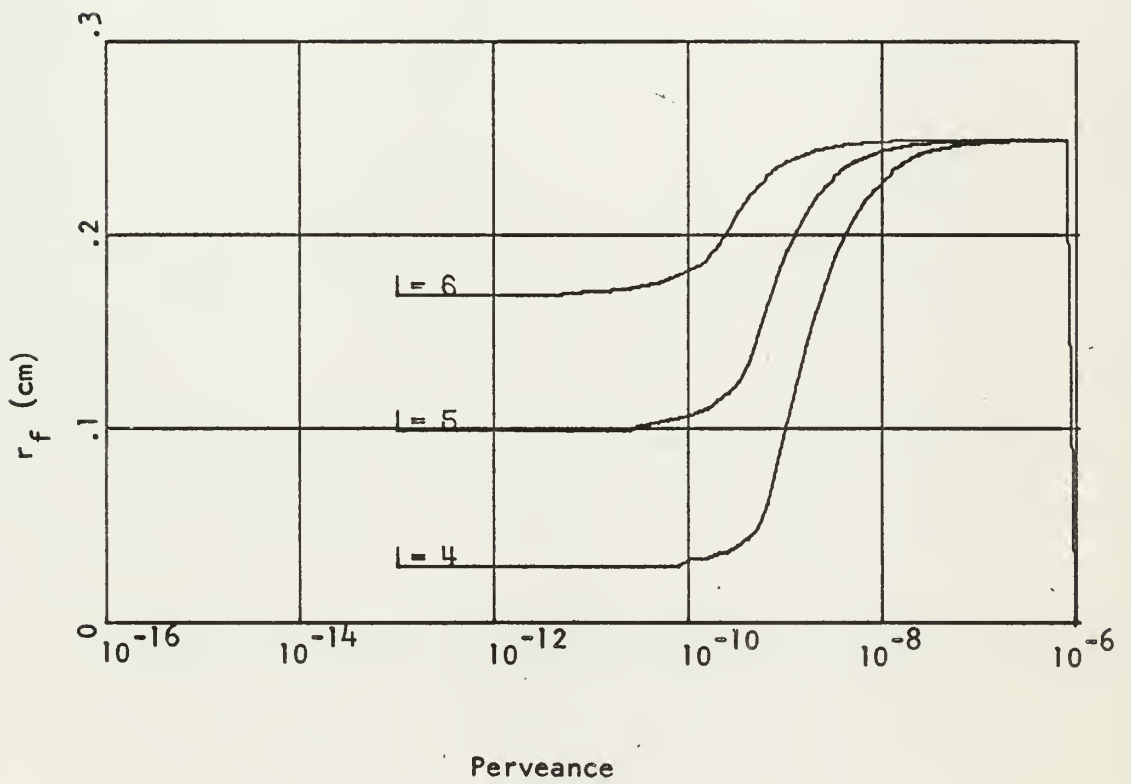
(b)

Fig. 6-10

$$\tan \gamma = .06 \quad R_B = .25 \text{ cm}$$



(a)

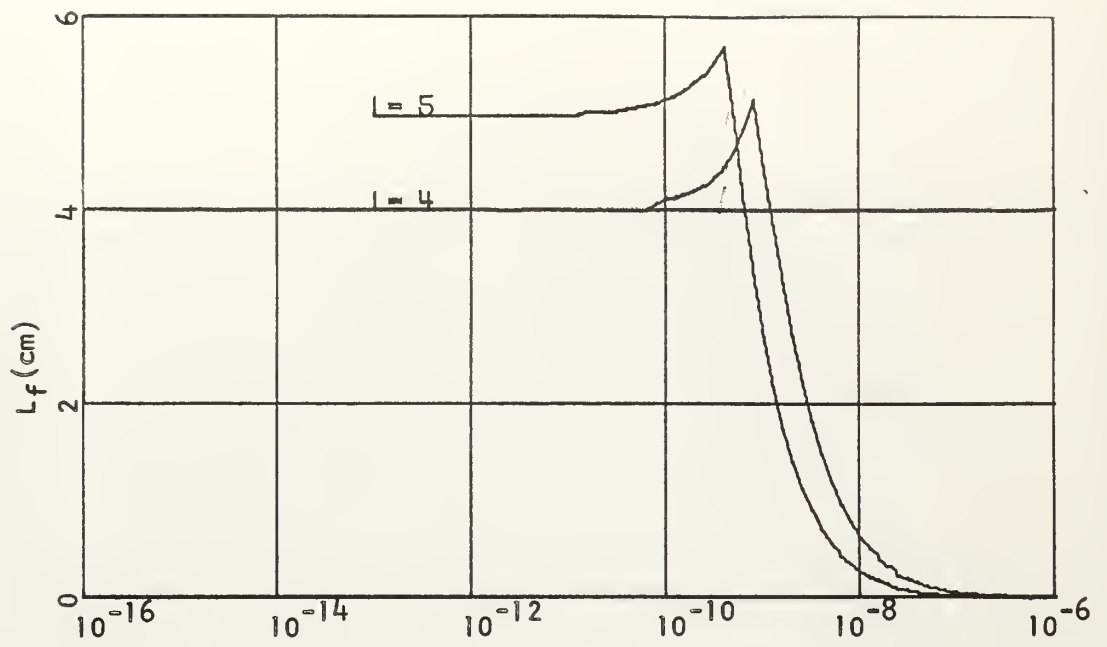


(b)

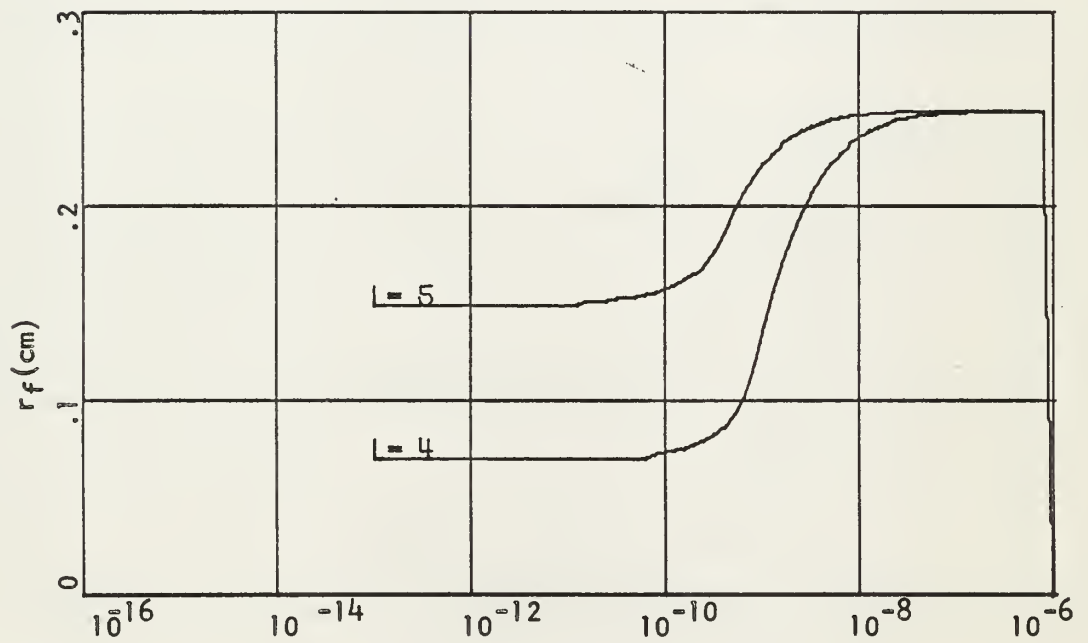
Fig. 6-11

$$\tan \gamma = .07$$

$$R_B = .25 \text{ cm}$$



Perveance
(a)

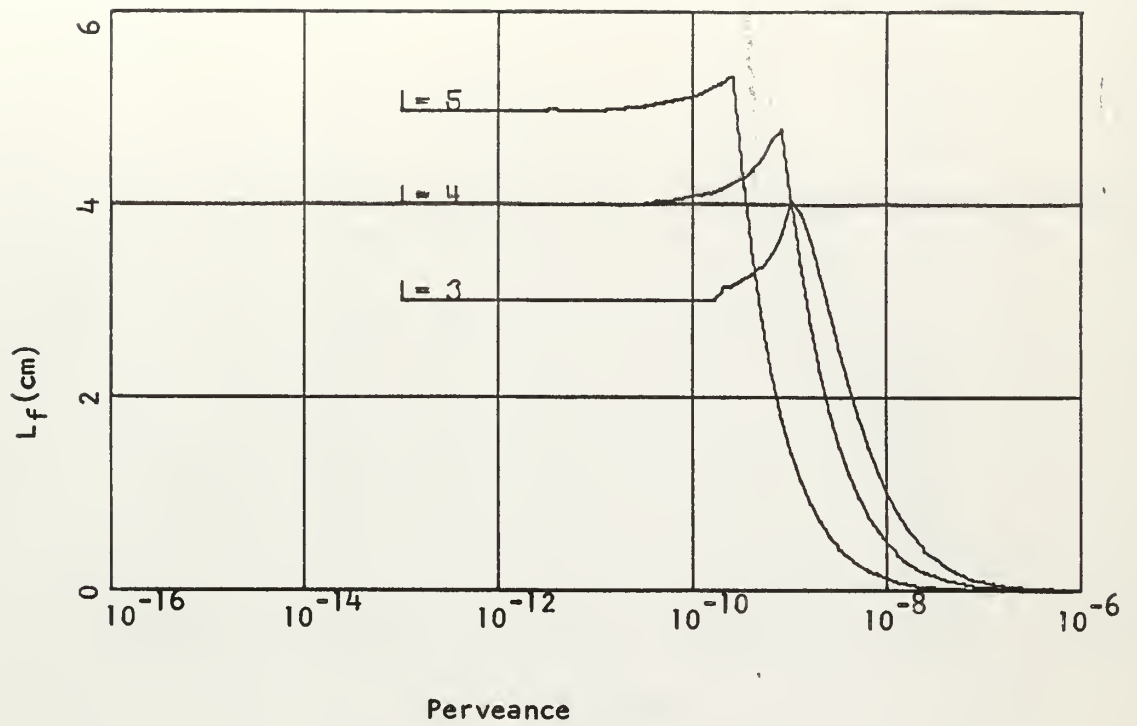


Perveance
(b)

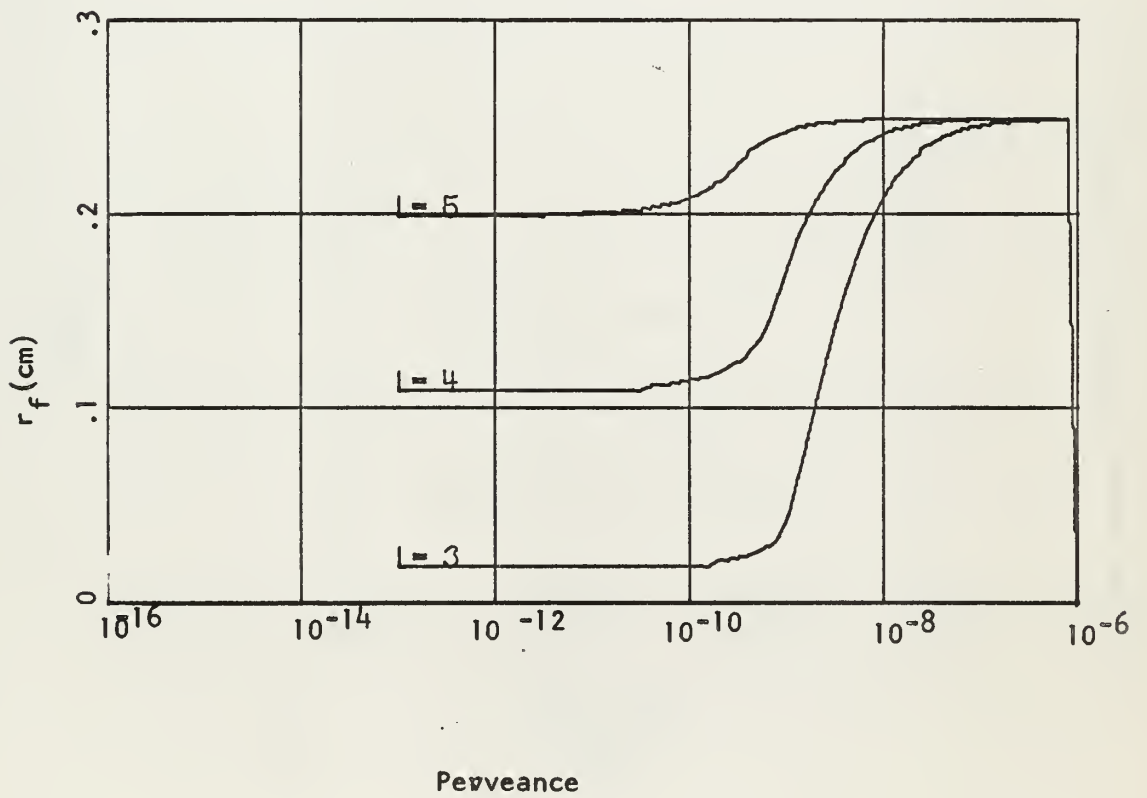
Fig. 6-12

$$\tan \chi = .08$$

$$R_B = .25 \text{ cm}$$



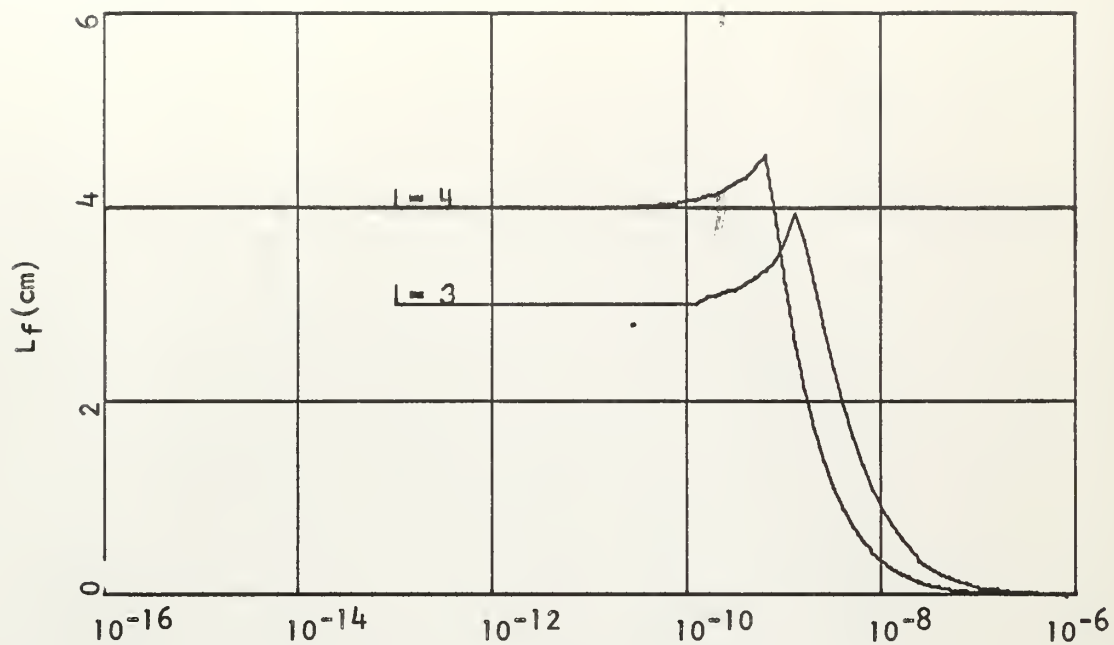
(a)



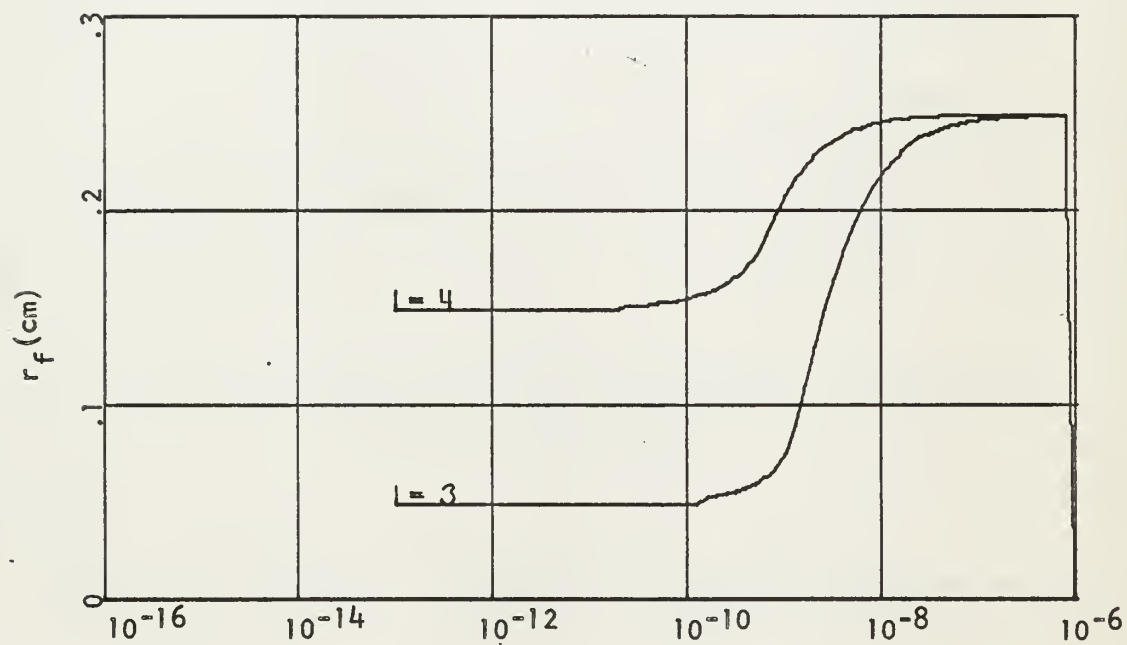
(b)

Fig. 6-13

$\tan \alpha = .09$ $R_B = .25$ cm.



Perveance
(a)



Perveance
(b)

Fig. 6-14

$$\tan \gamma = .10 \quad R_B = .25 \text{ cm}$$

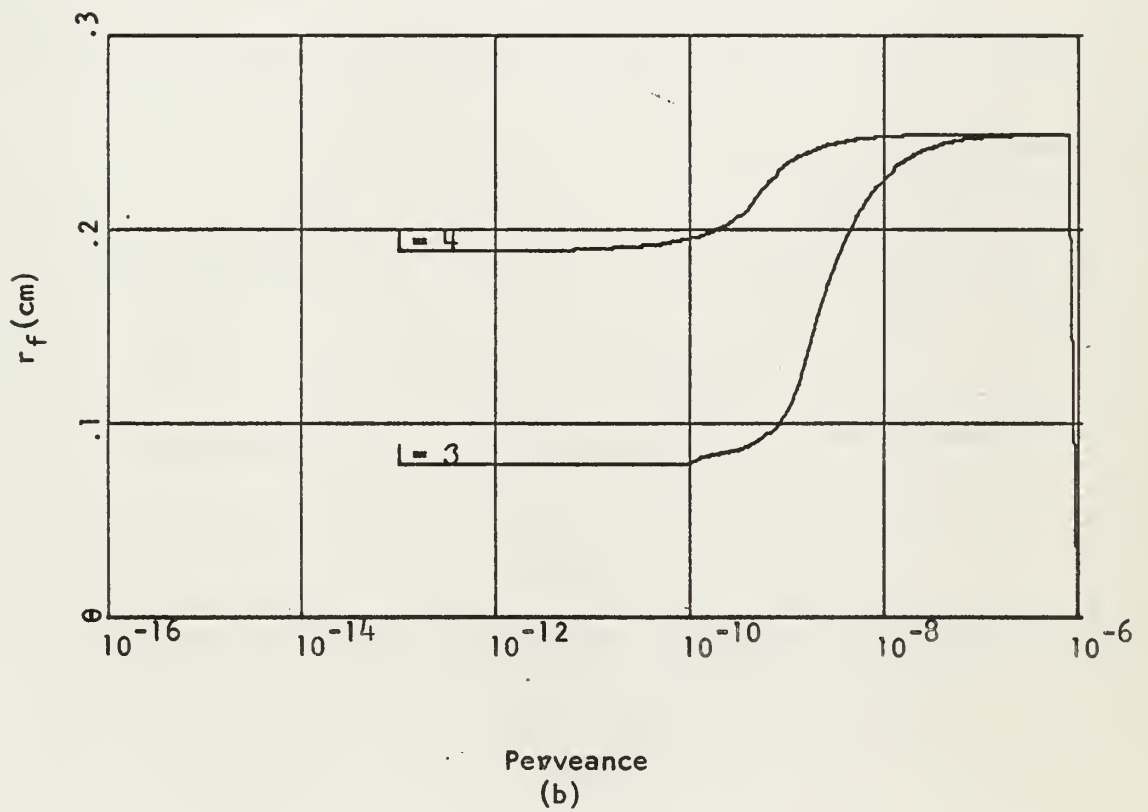
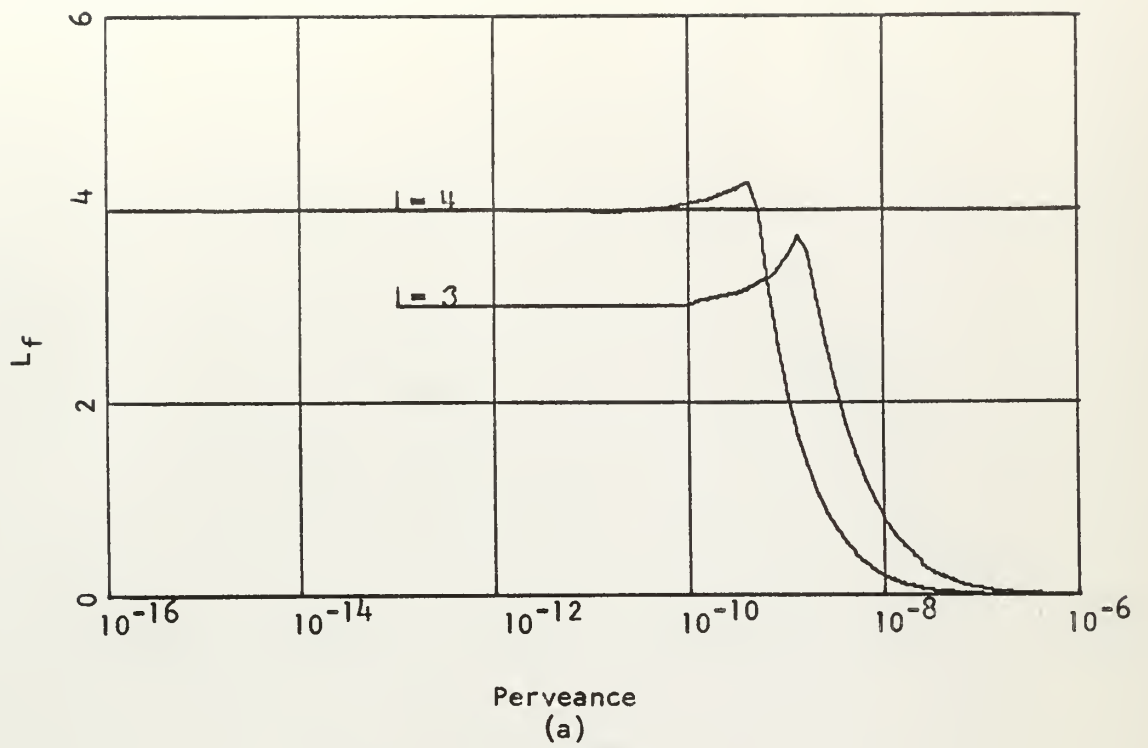


Fig. 6-15

$$\tan \gamma = .11 \quad R_B = .25 \text{ cm}$$

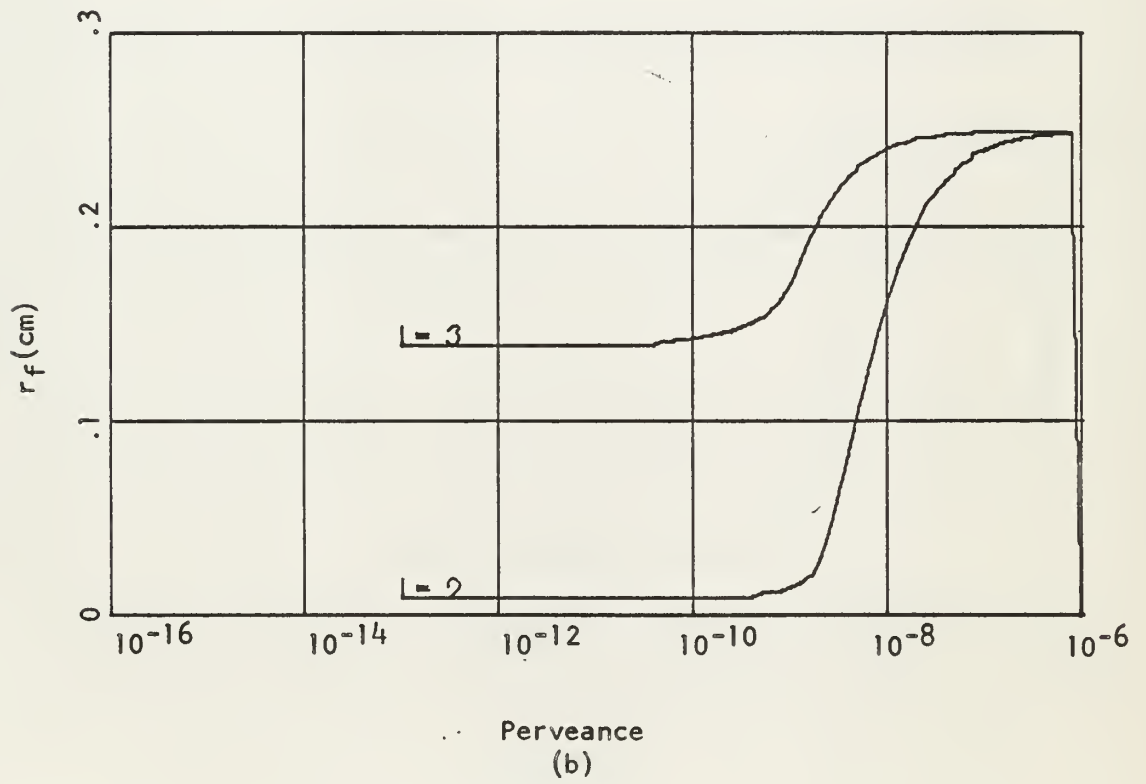
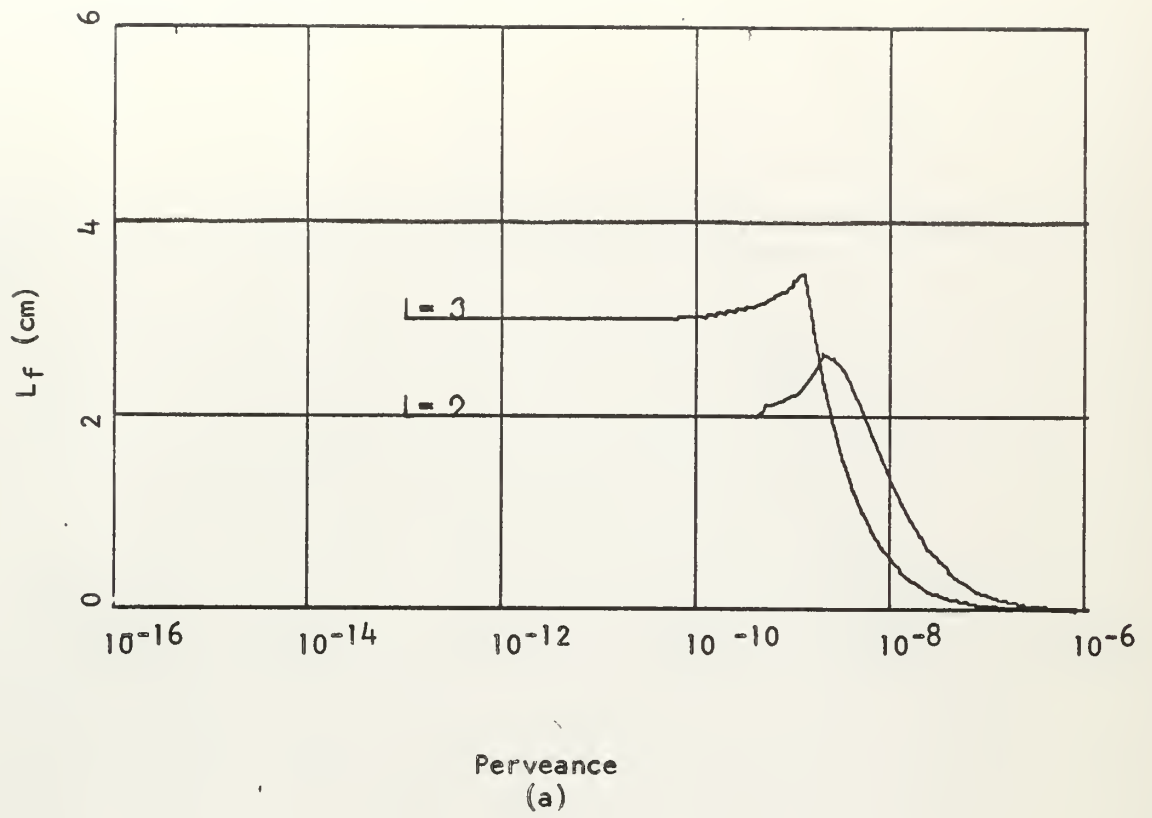
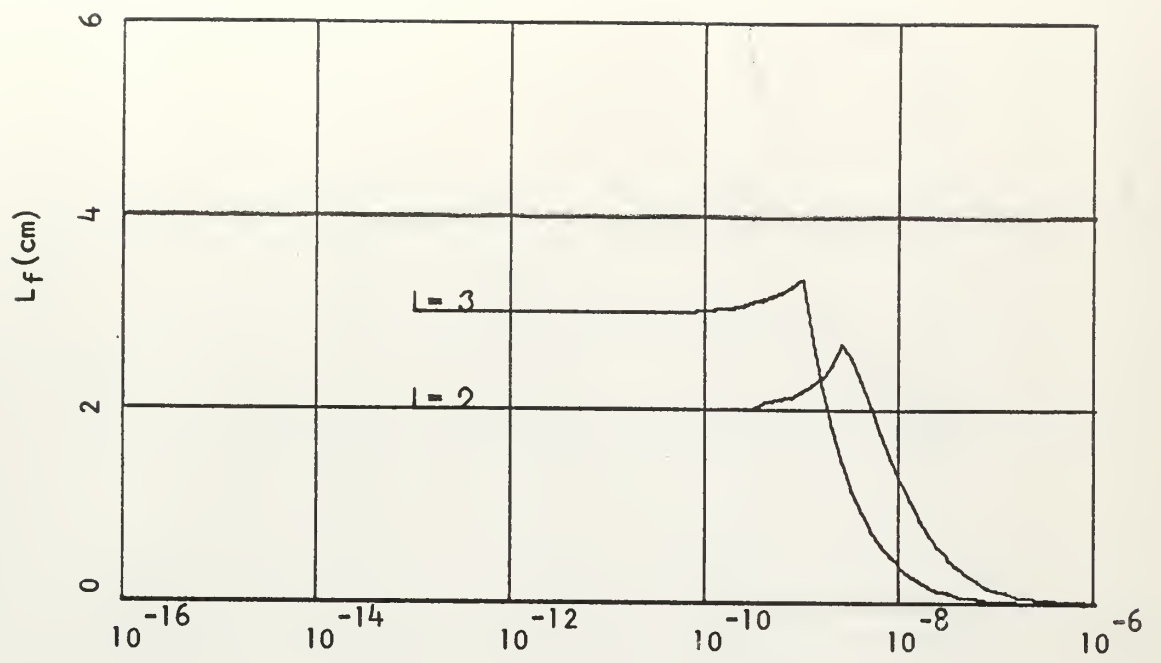
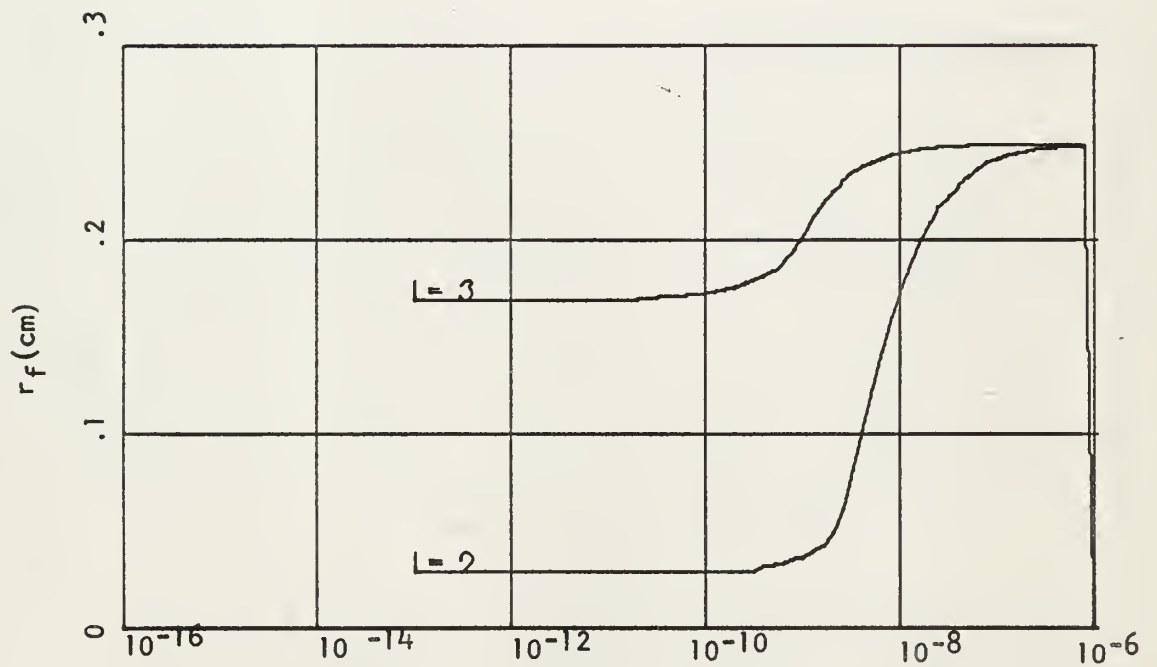


Fig. 6-16

$$\tan \alpha = .13 \quad R_B = .25 \text{ cm}$$



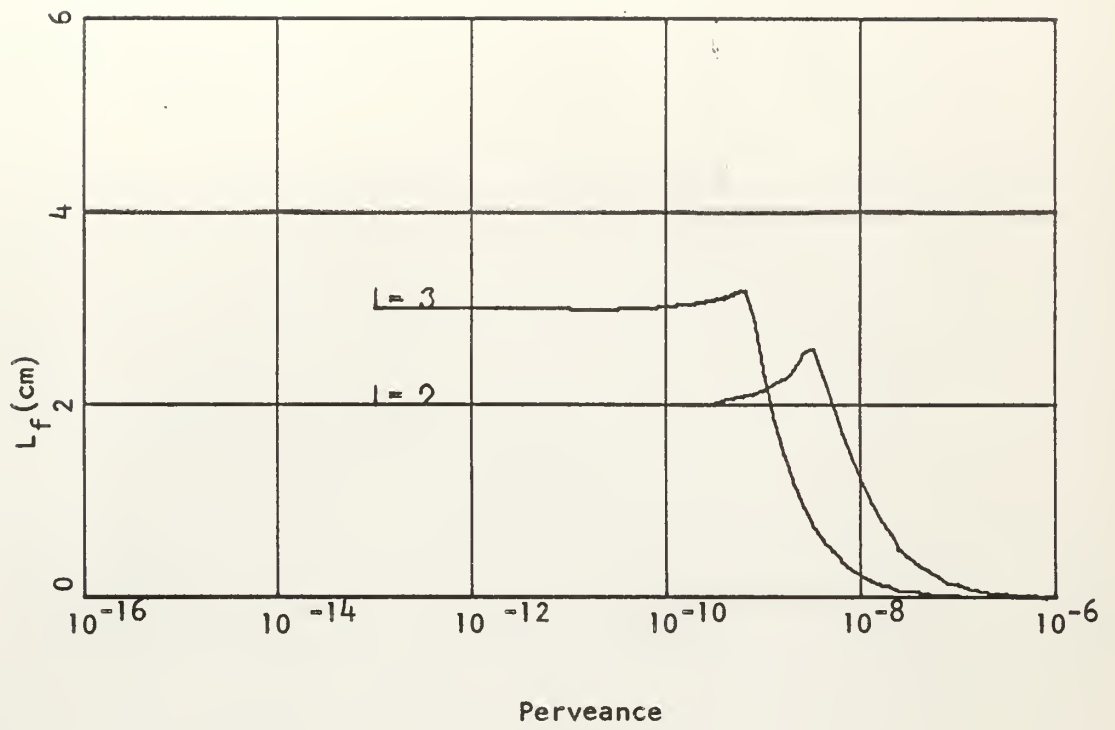
Perveance
(a)



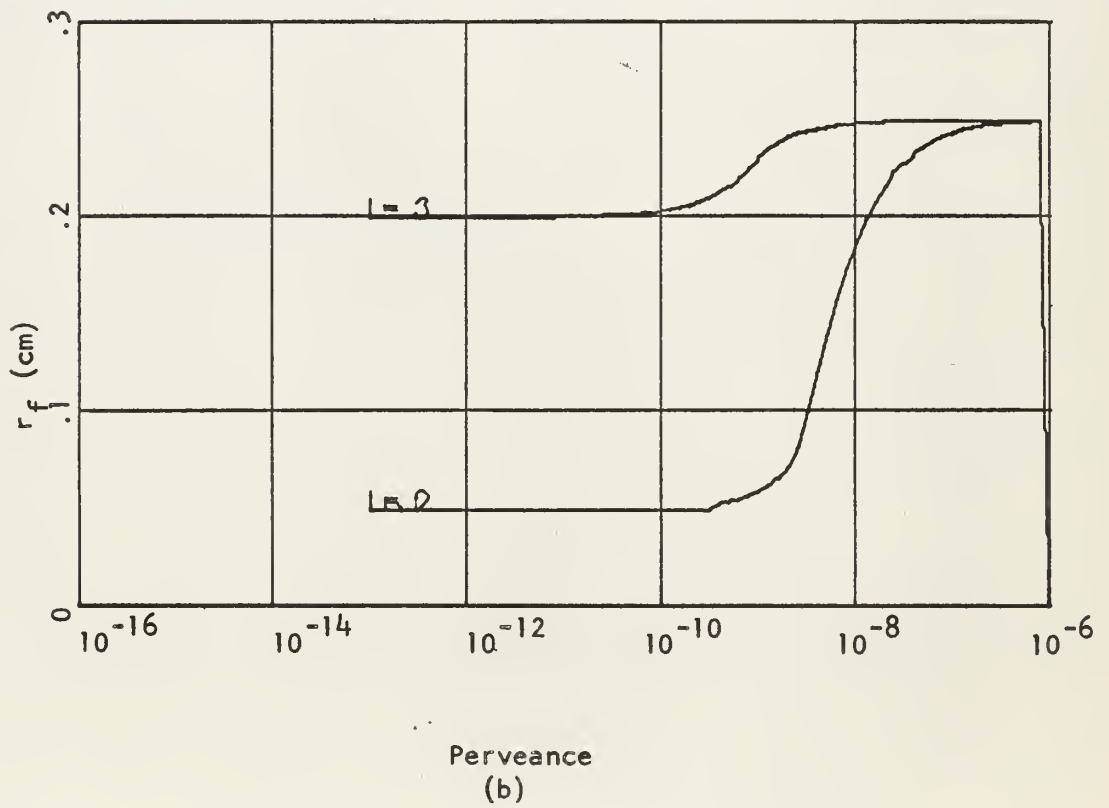
Perveance
(b)

Fig. 6-17

$$\tan \alpha = .14 \quad R_B = .25 \text{ cm}$$



(a)



(b)

Fig. 6-18

$$\tan \alpha = .15 \quad R_B = .25 \text{ cm}$$

thesH2983

Investigation of a low energy alkali ion



3 2768 002 07783 6

DUDLEY KNOX LIBRARY